

Dependence of He II Turbulence on Nonlocality and System Geometry

By

OWEN M. DIX

B.S. (Northern Arizona University, Flagstaff, AZ) 2005
M.S. (University of California, Davis) 2006

DISSERTATION

Submitted in partial satisfaction of the requirements for the degree of

DOCTOR OF PHILOSOPHY

in

Physics

in the

OFFICE OF GRADUATE STUDIES

of the

UNIVERSITY OF CALIFORNIA

DAVIS

Approved:

Professor Rena J. Zieve, Chair

Professor Richard Scalettar

Professor Andreas Albrecht

Committee in Charge

2012

Owen M. Dix
December 2012
Physics

Dependence of He II Turbulence on Nonlocality and System Geometry

Abstract

We have investigated two aspects of open-orbit vortices in He II turbulence simulations. These vortices form when using the local induction approximation in a system with full periodic boundaries. Using the fully nonlocal Biot-Savart law prevents this state from forming, but also increases computation time. We found that including the nonlocal calculation up to some truncated distance, on order of the average intervortex spacing, prevents this open-orbit state from forming. It is capable of significantly reducing computation time, while still accurately modeling homogeneous turbulence, as compared to the fully-nonlocal calculation.

We also sought a geometric approach to this phenomenon. Open-orbit vortices are in a state that is topologically distinct from ordinary turbulence. Vortex reconnections change the topology of the superfluid and are immediately responsible for vortices entering the open-orbit state. They are also required to free vortices from it. The periodic cube, equivalent to a flat 3-torus, is multiply-connected. This property allows the open-orbit vortex state to persist. We use the 3-sphere geometry, which is simply-connected, while keeping as many other properties of Euclidean turbulence as possible. However, the simplest driving velocity on the 3-sphere, the Hopf vector field, is not irrotational. It results in a state of highly-polarized turbulence, dissimilar to ordinary homogeneous turbulence found in experiment.

Contents

Abstract	ii
List of Figures	vii
List of Tables	xiii
Acknowledgments	xv
1 Background	1
1.1 Introduction	3
1.2 Vortex Dynamics	6
1.2.1 Equation of Motion	6
1.2.2 Reconnections	11
1.3 Emergence of the Open-Orbit Problem	12
1.4 References	18
2 Numerical Simulation	21
2.1 A Brief History of Numerical Methods	22
2.2 Approximating Spatial Derivatives	26
2.3 Spatial Resolution	31

2.3.1	Interpolation	32
2.4	Nonlocal Interactions	37
2.5	Reconnections	38
2.6	References	40
3	Periodic Boundaries	41
3.1	Motivation: Open-Orbit Vortices	43
3.2	Reproducing Homogeneous Turbulence	49
3.2.1	Our Data on the Open-Orbit Problem	49
3.2.2	Reproducing the Solution: Homogeneous Turbulence	52
3.3	Nonlocal Interaction Distance, d_{NL}	67
3.4	References	79
4	3-sphere	83
4.1	Motivation	83
4.2	Adaptations	85
4.3	S^3 with Nonlocal Interactions	90
4.3.1	Homogeneity	90
4.3.2	Anisotropy and Line Length Density	108
4.3.3	Dependence on Initial Conditions	117
4.3.4	Discussion	124
4.4	Varying the Nonlocal Interaction Distance, d_{NL}	125
4.4.1	Homogeneity	125
4.4.2	Anisotropy and Line Length Density	128

4.4.3	Dependence on Initial Conditions	131
4.4.4	The Effects of Nonlocal Interactions	137
4.5	References	144
5	Conclusion	147
5.1	Periodic Boundaries	147
5.2	3-sphere	149
5.3	References	155
A	Biot-Savart Law	157
A.1	Derivation of the Biot-Savart Law for \vec{v}_s	157
A.2	Green's Function Solution to Poisson's Equation	161
B	Kelvin's Theorem and Vortex Motion	163
B.1	Kelvin's Theorem	163
B.2	Vortices Move with Ideal Fluid Velocity	165
C	Parametric Curves	167
C.1	Tangent Vector	168
C.2	Curvature Vector	168
C.3	Binormal Vector	171
D	Scaling in Homogeneous Superfluid Turbulence	173
E	Vortex Visualization on S^3	177
E.1	Visualizing S^3	177

E.2	Stereographic Projection	181
E.3	Hyperspherical Coordinates	184
E.4	Hopf Fibration	185
F	Hopf Velocity Field	191
F.1	Hopf Velocity Properties	192
F.2	Divergence and Curl of Hopf Velocity	196
F.2.1	Divergence of Hopf Velocity	198
F.2.2	Curl of Hopf Velocity	202
G	Appendix References	205
G.1	References	205

List of Figures

1.1	Demonstration of the vorticity of a superfluid vortex filament.	5
1.2	Schematic of the relevant vectors involved in tracking vortex motion.	10
1.3	Vortex reconnection schematic	12
1.4	Schematic of the formation of open-orbit vortices	16
2.1	Schematic of interpolation on a vortex segment	34
2.2	Vortex configuration demonstrating geometry of new curvature vector	36
3.1	Comparison of vortex tangles using the LIA and the full Biot-Savart calculation, from Adachi et al. (2010)	45
3.2	Example plot of $L(t)$ from Aarts (1993)	46
3.3	Comparison of $L(t)$ and $I_{\parallel}(t)$ between the LIA and the full Biot-Savart calculation, from Adachi et al. (2010)	47
3.4	Our data comparing $L(t)$ and $I_{\parallel}(t)$ between the LIA and the full Biot-Savart calculation	50
3.5	Our data comparing vortex tangles using the LIA and the full Biot-Savart calculation	51
3.6	Evolution of vortex line length per octant volume	53
3.7	Average line length per octant volume	55

3.8	Average $\langle L \rangle^{1/2}$, from Aarts (1993)	56
3.9	Comparison of our line length density data to Aarts (1993)	57
3.10	Demonstration of scaling by β , from Schwarz (1988)	59
3.11	Comparison of our line length density data to Aarts (1993), scaled by β	60
3.12	Average mutual friction force density along the three primary axes . .	61
3.13	$\langle \bar{\Gamma} \rangle$, from mutual friction force density, versus v_{ns}	62
3.14	Average vortex velocity versus driving velocity	63
3.15	Anisotropy parameters for a range of driving velocities	64
3.16	Vortex reconnections and reconnection rate	68
3.17	Effects of nonlocal interaction distance on line length density	70
3.18	Root-Mean-Square fractional deviation versus nonlocal interaction dis-	
	tance	71
3.19	Root-Mean-Square fractional deviation versus nonlocal interaction dis-	
	tance using the entire equilibrated time domain	73
3.20	Line length density data for a range of system sizes	75
3.21	Root-Mean-Square fractional deviation versus nonlocal interaction dis-	
	tance for different system sizes	77
3.22	Fractional deviation of $\sigma(L)$ and $\sigma(I_{\parallel})$ versus driving velocity	78
3.23	Root-Mean-Square fractional deviation versus $(\langle \ell \rangle - d_{NL})/D$	80
4.1	Evolution of $L(t)$ for each \mathbb{R}^4 orthant	91
4.2	Average line length density for each \mathbb{R}^4 orthant	92
4.3	Example curves showing mirror symmetry in average line length den-	
	sity for each \mathbb{R}^4 orthant	93

4.4	Hopf projections of snapshots of the vortex tangle	98
4.5	Evolution of $L(t)$ for each Hopf-projected \mathbb{R}^3 octant	100
4.6	Average line length density within each Hopf-projected octant	101
4.7	Select curves showing mirror antisymmetry within each Hopf-projected octant	103
4.8	Extended $L(t)$ data for each Hopf-projected \mathbb{R}^3 octant	105
4.9	Separated octant data from Figure 4.8	106
4.10	Average extended line length density for each Hopf-projected octant .	107
4.11	Average anisotropy parameter I_{\parallel}	109
4.12	Vortex reconnections and reconnection rate	111
4.13	Evolution of $L(t)$	112
4.14	Fit of average line length density data	113
4.15	Average line length density per \mathbb{R}^4 orthant and Hopf-projected \mathbb{R}^3 octant using larger driving velocities	115
4.16	Fit of $\langle L \rangle$ using larger driving velocities	116
4.17	Stereographic projection of the initial condition: a perturbed ring just outside of xy -plane	118
4.18	Evolution of $L(t)$ comparing different initial perturbed vortices	119
4.19	Hopf projection of initial vortex tangle	120
4.20	Evolution of $L(t)$ comparing an initial vortex tangle and perturbed initial vortex rings	121
4.21	Stereographic projections of Hopf vector field along initial perturbed vortices	123

4.22 Average line length density per \mathbb{R}^4 orthant volume for different d_{NL} values	126
4.23 Average line length density for each Hopf-projected \mathbb{R}^3 octant volume for different d_{NL} values	127
4.24 Anisotropy and average line length density for different d_{NL} values	129
4.25 Root-Mean-Square fractional deviation versus d_{NL}	130
4.26 Average line length density for different d_{NL} values with different initial perturbed rings	132
4.27 Evolution of $L(t)$ for $d_{NL} = 0.25\pi r_0$ with different initial perturbed rings	133
4.28 Evolution of $L(t)$ with different d_{NL} values for an initial vortex tangle or an initial perturbed ring	134
4.29 Root-Mean-Square fractional deviation versus d_{NL} with different initial perturbed rings	135
4.30 Root-Mean-Square fractional deviation versus $(\langle \ell \rangle - d_{NL})/r_0$	136
4.31 Anisotropy parameter I_{\parallel} versus v_{ns} for small d_{NL}	138
4.32 Snapshots of vortex tangle under Hopf fibration and stereographic projection for $d_{NL} = 0$ and $d_{NL} = 0.5\pi r_0$	140
4.33 Stereographic projection of growth of an initial perturbed vortex	141
4.34 Components of the nonlocal velocity versus time and driving velocity	142
5.1 Comparison of vortex polarization between the 3-sphere geometry and rotational counterflow, from Tsubota et al. (2003)	153

B.1	Arbitrary contour of integration	165
B.2	Superfluid vortex filament	166
C.1	Schematic of the relevant vectors involved in tracking vortex motion.	171
E.1	Association between a 2-sphere and a 2-ball	178
E.2	Association of 3-ball with 3-sphere	179
E.3	The association between a periodic box and a 2-torus is shown.	180
E.4	Stereographic projection of circle	181
E.5	Stereographic projection of 2-sphere	183
E.6	Flow lines of Hopf velocity field under Hopf fibration and stereographic projection	190

List of Tables

3.1	Comparison of quantities characterizing homogeneous turbulence between other sources	66
4.1	Demonstration of \mathbb{R}^4 orthant (binary) number inversion symmetry . .	94
4.2	Demonstration of Hopf-projected \mathbb{R}^3 octant (binary) number inversion antisymmetry	102

Acknowledgments

Thank you to my family and friends for supporting me. I would like to thank Professor Greg Kuperberg for helpful conversations and correspondence. And I am especially grateful to Professor Rena Zieve. You have been a wonderful advisor.

Chapter 1

Background

As liquid ${}^4\text{He}$ is cooled below $T \approx 2.2$ K, it enters a phase of matter called He II, which is comprised of two inseparable fluids, the normal fluid and superfluid. Physically, the superfluid component is comprised of the ground state of a Bose-Einstein Condensate, while the normal fluid component is made up of quasiparticle excitations out of the ground state (London, 1938, Barenghi et al., 1983). Below some critical velocity, the superfluid exhibits remarkable properties, such as the ability to flow perpetually without dissipation. Above this velocity, the normal fluid interaction with filamentary superfluid vortices leads to significant dissipation and the system becomes turbulent. Reviews of this extensive area of research can be found in Vinen and Niemela (2002), Vinen (2006).

Ordinary turbulence involves the swirling of fluid particles on a continuum of different length scales. The kinetic energy of rotation at large length scales is transferred to eddies of smaller and smaller sizes until it is dissipated as heat at the smallest scales, through viscous interactions. The quantum nature of superfluids indicate that they are irrotational, implying that the superfluid component would not support tur-

bulence. However, Feynman (1955) suggested that superfluid turbulence could exist as a tangle of filamentary vortices around which the superfluid can rotate, and Vinen (1957a) gave experimental evidence supporting its existence. These filamentary vortices have a fixed vortex core radius but can curve and distort to form structures of different length scales. An applied driving velocity can cause a system of such vortices to grow, while interactions of vortices with the normal fluid and with each other can dissipate energy and thus reduce the line length of these vortices. Vinen (1957b) presented an analysis of this system explaining the homogeneous state, where the growth and decay rates are equal. The first successful microscopic model of this homogeneous turbulent system was presented by Schwarz (1982).

Simulating the turbulent system is simplified by eliminating the real-wall boundaries found in experiment. Instead, it is common to make these walls periodic, such that one wall is identified with the wall directly opposite. This tool, used commonly in condensed matter physics, is equivalent to a system with an infinite number of copies in each direction. It has the benefit of saving complexity from the boundaries, which saves computation time. Furthermore, real-wall boundaries affect fluid flow; which means turbulence will not be homogeneous throughout the entire volume since the region nearest the boundaries behaves differently from the center of the system. One must, therefore, use a significantly larger system than desired to get portion of that volume which is relatively homogeneous. This increases computation time even more. Schwarz (1988) revealed details of a problem with simulating superfluid turbulence in periodic boundaries, however. The problem occurs when vortices arrange in a particular way, forming open orbits through the periodic cube geometry.

This open-orbit problem is the primary focus of this work. For the remainder of this chapter, I shall introduce some background on superfluid turbulence, developing the fundamentals of vortex dynamics, as well as describing this open-orbit problem in more detail. Chapter 2 discusses some of the specific features of our simulation method. Then, in Chapter 3, I discuss our contribution to simulating ^4He turbulence in the periodic cube. Finally, Chapter 4 uses the 3-sphere geometry to approach simulating superfluid turbulence, without boundaries, and to investigate its effects on this open-orbit problem.

1.1 Introduction

In order to derive some important properties of superfluid He II, we can make note of the ability for a superfluid to flow without dissipation. Outside of superfluids and superconductors, perpetual motion exists on a microscopic scale, inside discrete quantum states. Thus, we are inclined to suspect the superfluid phenomenon is quantum mechanical in nature. The He II superfluid can be represented by a relatively generic complex macroscopic wavefunction:

$$\Psi(\vec{r}) = \Psi_o \exp(iS(\vec{r})), \quad |\Psi|^2 = \frac{\rho_s}{m_4}, \quad (1.1)$$

where $S(\vec{r})$ is the position-dependent phase, ρ_s is the superfluid density, and m_4 is the mass of the ^4He atom. Applying the quantum mechanical momentum operator,

$\hat{p} = -i\hbar\nabla$, we obtain a relation for the superfluid velocity:

$$\vec{v}_s = (\hbar/m_4)\nabla S(\vec{r}). \quad (1.2)$$

Since the curl of a continuous gradient field is zero, we find that a superfluid is irrotational: $\nabla \times \vec{v}_s = 0$. By inserting this into an equation for the circulation around a closed contour, Equation 1.3, and applying Stokes' theorem, we see the circulation of a superfluid is, indeed, zero.

$$\begin{aligned} \Gamma &:= \oint_{\mathcal{C}} \vec{v}_s \cdot d\vec{l} \\ &= \int_{\mathcal{A}} (\nabla \times \vec{v}_s) \cdot d\vec{a} = 0 \end{aligned} \quad (1.3)$$

Superfluid *can* rotate, but only around filamentary vortex cores, inside of which, the superfluid wavefunction becomes zero, and only the normal fluid remains. If our surface, \mathcal{A} , contains the vortex filament, a region where we can no longer state that \vec{v}_s is irrotational, Γ no longer needs to vanish. Inserting Equation 1.2 for the superfluid velocity into Equation 1.3 shows that $S(\vec{r})$ must be multi-valued. Since the wavefunction must be single-valued, $S(\vec{r}_0) - S(\vec{r}_0)$ must be $2\pi n$, where n is an integer.

$$\begin{aligned} \Gamma &= \frac{\hbar}{m_4} \oint_{\mathcal{C}} \nabla S \cdot d\vec{l} = nh/m_4, \\ \kappa &:= h/m_4 \end{aligned} \quad (1.4)$$

Note that the circulation contains only constants fundamental to the system, so we

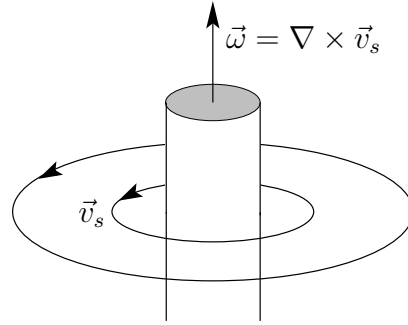


Figure 1.1: Demonstration of the vorticity of a superfluid vortex filament.

have defined the quantum of circulation, κ . For completion, we can now define a nonzero vorticity in the region of the vortex filament, $\vec{\omega} = \nabla \times \vec{v}_s = n\kappa\hat{\omega}/2\pi a_0$, where a_0 is the core radius, which in He II is about $1.3 \cdot 10^{-8}$ cm (see Figure 1.1). The fact that we can have a definite, quantized circulation surrounding a vortex filament, means this vortex must either close on itself, forming a ring, or else terminate on a solid-wall boundary.

Consider a single, infinite, straight vortex filament in Figure 1.1. With a contour at a distance $r > a_0$ from the filament, we can now solve for the velocity.

$$\Gamma = \oint_C \vec{v}_s \cdot d\vec{l} = nh/m_4,$$

$$v_s = nh/2\pi m_4 r. \quad (1.5)$$

Note that v_s would diverge if not for the existence of the vortex core, a_0 . Nevertheless, we have $v_s \propto n$, so the kinetic energy per unit vortex length becomes:

$$\varepsilon = \int_{a_0}^D \rho_s v_s^2 r dr \propto n^2,$$

(integrating from a_0 to our system size, D). The energy per unit length of a vortex is proportional to n^2 . It is more favorable under ordinary conditions to form two $n = 1$ vortices than one $n = 2$ vortex. This also tells us that the energy of our system is proportional to the total line length. This quantity will play a major role in our analysis of the turbulent system, when we present our work in Chapters 3 and 4.

The quantized nature of the superfluid vortices greatly simplifies vortex dynamics over ordinary fluids. Turbulence in a quantum fluid involves tracking the motion of these filamentary vortices as they grow, shrink, and distort. We will now look at the dynamics of these superfluid vortices.

1.2 Vortex Dynamics

1.2.1 Equation of Motion

He II is incompressible, $\nabla \cdot \vec{v}_s = 0$. This property allows us to find our vortex equation of motion. By comparing to electrodynamics:

$$\begin{aligned}\nabla \cdot \vec{v}_s &= 0 \leftrightarrow \nabla \cdot \vec{B} = 0 \\ \nabla \times \vec{v}_s &= \vec{\omega} \leftrightarrow \nabla \times \vec{B} = \mu_o \vec{J}\end{aligned}$$

we can see that, just like \vec{B} , the superfluid velocity will obey the Biot-Savart law, Equation 1.6.

$$\vec{v}_s(\vec{r}) = \frac{\kappa}{4\pi} \int \frac{(\vec{s} - \vec{r}) \times d\vec{l}}{|\vec{s} - \vec{r}|^3} \quad (1.6)$$

Here, \vec{s} is the position vector of the vortex being integrated over, \vec{r} is the position vector of a fluid particle and $d\vec{l}$ points along the vortex in the direction of the vorticity, $\vec{\omega}$ from Figure 1.1. For an explicit derivation, see Appendix A. Vorticity at \vec{s} induces a velocity at \vec{r} . This comes as no surprise, since a vortex is just a filament that fluid flows around.

Equation 1.6 tells us how the fluid moves, but not the vortices themselves. For that, we turn to Kelvin's theorem, which states that circulation in an ideal fluid is conserved (Appendix B).

$$\frac{d\Gamma}{dt} = \frac{d}{dt} \oint_C \vec{v}_s \cdot d\vec{l} = 0$$

This implies that vortices in an ideal fluid move with the fluid velocity (Appendix B).

We now have that, with a given arrangement of vortices, the Biot-Savart law can predict the future motion of those vortices. Each vortex segment acts as a source of superfluid velocity, which then drives another vortex segment to move with its local \vec{v}_s . It is convenient to parametrize the vortex filament by the arclength along it, ξ , which increases in the direction of the vorticity vector (Appendix C).

$$\dot{\vec{s}}_{\text{Biot}}(\xi, t) = \frac{\kappa}{4\pi} \int \frac{(\vec{s}_o - \vec{s}) \times d\vec{\xi}_o}{|\vec{s}_o - \vec{s}|^3}, \quad (1.7)$$

The vector, $d\vec{\xi}_o$ points tangent to the vortex segment being integrated over, and the parameter itself varies over all vortices in the system. We deal specifically with homogeneous turbulence which is driven by an applied \vec{v}_s . So, the total vortex velocity from the superfluid, $\dot{\vec{s}}_{\text{sf}}$, is just the sum of these two components, $\vec{v}_s + \dot{\vec{s}}_{\text{Biot}}$.

Until now, we have ignored the normal fluid component of He II. However the

normal fluid is known to interact with the superfluid vortex core, see for example (Barenghi et al., 1983). This interaction yields an additional vortex velocity dependent on the relative motion between the vortex core and the normal fluid:

$$\dot{\vec{s}}_{\text{nf}} = \alpha \hat{s}' \times (\vec{v}_n - \dot{\vec{s}}_{\text{sf}}) - \alpha' \hat{s}' \times [\hat{s}' \times (\vec{v}_n - \dot{\vec{s}}_{\text{sf}})],$$

where, \hat{s}' is a unit vector pointing tangent to the vortex line. α , and α' are dimensionless friction coefficients, dependent on temperature and characterizing the interaction. The system temperature in a simulation is entirely determined by the value of these two coefficients. Assembling these, we have the full form for the equation of motion of a vortex (Schwarz, 1985):

$$\dot{\vec{s}}(\xi, t) = [\vec{v}_s + \dot{\vec{s}}_{\text{Biot}}] + \alpha \hat{s}' \times (\vec{v}_n - [\vec{v}_s + \dot{\vec{s}}_{\text{Biot}}]) - \alpha' \hat{s}' \times [\hat{s}' \times (\vec{v}_n - [\vec{v}_s + \dot{\vec{s}}_{\text{Biot}}])].$$

Note that the Biot-Savart integral diverges as the source point, \vec{s}_o , approaches the field point, \vec{s} . So the integral can be split into a local part and nonlocal part (Arms and Hama, 1965, Schwarz, 1985). The local part omits distances from the field point within about the filament core radius, a_0 , equating this with the filament's internal structure. It extends as far as l_{\pm} in each direction along the vortex core. The remaining integral is included in the nonlocal part of the integral.

$$\dot{\vec{s}}_{\text{Biot}}(\xi, t) = \frac{\kappa}{4\pi} \hat{s}' \times \vec{s}'' \ln \left(\frac{2(l_+ l_-)^{1/2}}{e^{1/4} a_0} \right) + \frac{\kappa}{4\pi} \int' \frac{(\vec{s}_o - \vec{s}) \times d\vec{\xi}_o}{|\vec{s}_o - \vec{s}|^3} \quad (1.8)$$

The primed integral in the nonlocal part indicates the integration range excludes the

region l_{\pm} neighboring \vec{s} . Since the local term dominates, it is common, historically, to reject the nonlocal part. This is called the local induction approximation (LIA). When this is done, there is no objective best cutoff for l_{\pm} in the local term so the average radius of curvature, \bar{R} , is used, and the coefficient in front of the local term is referred to as β , sometimes inserting a constant of order unity, c .

$$\beta := \frac{\kappa}{4\pi} \ln \left(\frac{\bar{R}}{ca_0} \right)$$

We, however, do not use this approximation, a choice discussed in Chapter 3. We also make a number of modifications to the equation of motion in our simulations. First of all, it should be noted that several previous works ignore α' (Schwarz, 1982, Buttke, 1986, Aarts, 1993). For the temperature value we use in our simulations ($T=1.6$ K, corresponding to $\alpha = 0.1$), α' is small compared to α , so we have done the same. So our equation of motion becomes:

$$\begin{aligned} \dot{\vec{s}}(\xi, t) &= \vec{v}_s + \beta_* \hat{s}' \times \vec{s}'' + \dot{\vec{s}}_{\text{Biot}^*} + \alpha \hat{s}' \times (\vec{v}_{ns} - \beta_* \hat{s}' \times \vec{s}'' - \dot{\vec{s}}_{\text{Biot}^*}) \quad (1.9) \\ \beta_* &= \frac{\kappa}{4\pi} \ln \left(\frac{2(l_+ l_-)^{1/2}}{e^{1/4} a_0} \right) \\ \dot{\vec{s}}_{\text{Biot}^*} &= \frac{\kappa}{4\pi} \int' \frac{(\vec{s}_o - \vec{s}) \times d\vec{\xi}_o}{|\vec{s}_o - \vec{s}|^3} \end{aligned}$$

where we have used the notation, $\vec{v}_{ns} = \vec{v}_n - \vec{v}_s$. Figure 1.2 shows a diagram of the relevant vectors in computing the vortex equation of motion. The vectors \hat{s}' , \vec{s}'' , and $\hat{s}' \times \vec{s}''$ point in the tangent, normal and binormal directions, respectively.

Although superfluid turbulence is inherently quantum mechanical, Equation 1.9

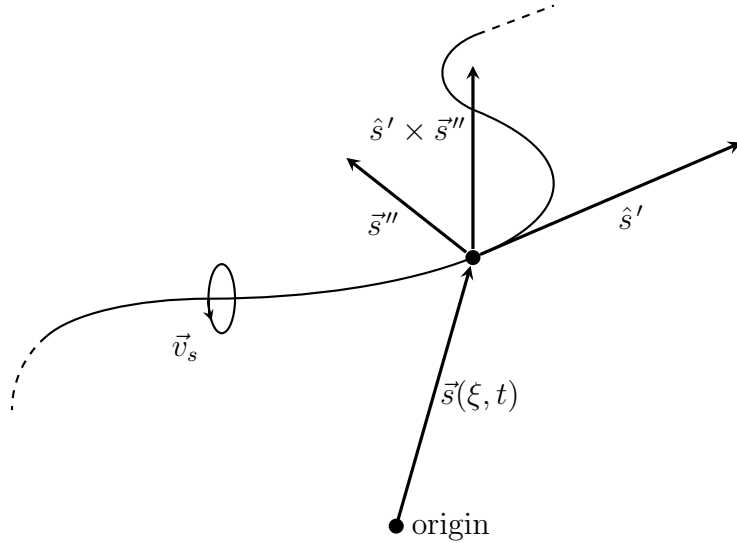


Figure 1.2: Schematic of the relevant vectors involved in tracking vortex motion.

is semi-classical in nature. The quantum nature of the superfluid led to quantization of the vortex circulation, which meant our vortices could be described as filaments. This allows us to track individual points on the curve, without regard for diffusion of the vorticity. Furthermore, the nonlocal term arises from interaction between these vortices and the normal fluid, which is comprised of excitations of the Bose-Einstein condensate ([Barenghi et al., 1983](#)). Nevertheless, we are left with an equation which simply tracks these vortex filaments as they move around in the system.

It is useful to investigate what effect each term in Equation 1.9 has on vortex dynamics. Clearly, \vec{v}_s indicates that the driving velocity influences vortex motion. This is often of uniform magnitude and direction, which just leads to uniform translation of the vortex system (we deal with a different applied field in Chapter 4). The local term, $\hat{s}' \times \vec{s}''$, causes motion in the binormal direction. When a simulation employs the LIA, this term causes no growth or decay of the vortex ([Buttke, 1986](#), p. 10-11).

If one does not use the LIA, the coefficient in front of the local term can vary across the vortex, strictly because of variation in point spacing, which can lead to vortex stretching or shrinking. However, this is generally insignificant since point spacing varies inside the logarithmic term in β_* . The local component also appears inside the friction term, $\alpha \hat{s}' \times (-\beta_* \hat{s}' \times \vec{s}'')$. Referring to Figure 1.2, this term always causes motion of the vortex in the normal direction. In other words, this always straightens the vortex, decreasing its line length. The remaining terms can lead to vortex growth or decay depending on the arrangement of vortices.

1.2.2 Reconnections

While the equation of motion controls much of vortex dynamics, there is one important ingredient that it does not describe: vortex reconnections. This process involves two vortex segments touching a point, and swapping the neighboring ends of the vortex such that the vortex orientation is preserved. A schematic of this reconnection phenomenon is shown in Figure 1.3.

When the nonlocal interaction between two vortex segments dominates other sources of vortex motion, these two vortices can attract. However, the vortex equation of motion (Equation 1.9), does not account for the actual reconnection process, which is quantum mechanical (Koplik and Levine, 1993). A detailed analysis of this process has shown that it is sufficient for the study of homogeneous turbulence to model vortex reconnections with a quick exchange of vortex segments (Schwarz, 1985). However, one must take some care so that the ansatz employed does not drastically alter the line length in the system. This combination of the vortex equation

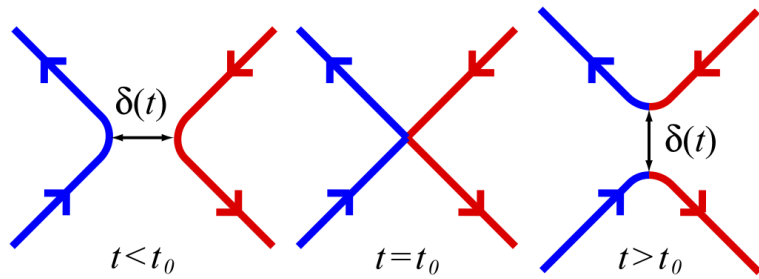


Figure 1.3: Vortex reconnection schematic, taken from Paoletti et al. (2008). Arrows indicate the direction of the tangent vector.

of motion and reconnection ansatz makes up the physical system in our simulations. The vortex equation of motion is responsible for growth of vortices, which occurs primarily in planes perpendicular to the driving velocity. Homogeneous turbulence is three dimensional. Vortex reconnections allow for nonlocal interactions between these planes of expanding vortices, randomizing the system. Vortices will often reconnect in a way that produces smaller vortices which will then grow, sustaining turbulence.

1.3 Emergence of the Open-Orbit Problem

During the late 1980's there was something of a controversy between physicist K. W. Schwarz, of the IBM Thomas J. Watson Research Center, and Thomas F. Buttke, an applied mathematician of Lawrence Berkeley Laboratory. Such debates are a necessity in science, so that the real issues at hand can be fleshed out. Since this one is so central to the project I am discussing, it is worth going over in detail.

After working for several years to develop a theory of superfluid turbulence, Schwarz (1982) finally presented the claim that the macroscopic behavior of homogeneous superfluid turbulence could be modeled by applying some simple dynamical rules to the vortices. The apparent goal of this paper was to find the simplest possible model that was consistent with homogeneous turbulence.

The model used by Schwarz (1982) consisted of two main features. Vortices were almost entirely governed by the local induction approximation (LIA), but could also be occasionally influenced by the nonlocal effects of other vortices when two segments approached close enough to reconnect (the reconnection ansatz). Both of these features were discussed in Section 1.2. The LIA provides a computational advantage. When the vortex is discretized, if there are N vortex segments in the system, the full Biot-Savart law would be $\mathcal{O}(N^2)$, computations, while the LIA is only $\mathcal{O}(N)$. A few years later, Schwarz (1985) detailed the reconnection ansatz. Allowing the vortex reconnection to occur in full detail was computationally expensive and observing a number of these reconnections with different orientations showed that this quick exchange was sufficient for modeling homogeneous turbulence.

Thomas F. Buttke, had a different approach than Schwarz. Buttke (1986) gave the first attempt at finding a stable numerical solution to simulating homogeneous superfluid turbulence using the LIA. In contrast to the perspective taken in Schwarz (1982), Buttke (1986) aimed to model the vortex dynamics as accurately as possible. Buttke (1987) summarized his findings in a comment on Schwarz (1982). The algorithm derived by Buttke (1986) was unable to reproduce one of the characteristic markers of homogeneous superfluid turbulence: $\langle L \rangle \propto v_{ns}^2$, where $\langle L \rangle$ is the line length

density of the vortex system. This relation was well established experimentally for homogeneous superfluid turbulence (Tough, 1982) as well as theoretically explained by a dimensional scaling relation put forward by Schwarz (1982), (see Appendix D). Buttke (1987) commented that the algorithm presented by Schwarz (1985) was adequate for ordinary vortex dynamics. His real concern was with Schwarz's mesh spacing during a reconnection.

Buttke (1987) argued that the mesh spacing for points along the vortex must decrease with increased applied fluid velocity. Using this spacing allowed for accurate modeling of the high-curvature regions that occur during a reconnection. However, it also yielded $\langle L \rangle$ that varied linearly with v_{ns} , not quadratically. Not using the refined spacing criterion meant the spacing was not suitable for modeling the reconnection process but it also recaptured the correct $\langle L \rangle \propto v_{ns}^2$ behavior for homogeneous turbulence. Precisely how the unrefined spacing was insufficient is important. Buttke found that, when the coarser spacing was applied, small spurious vortex loops were formed near reconnection sites. These spurious vortices were enough to sustain homogeneous turbulence. When the spacing was refined, the spurious vortices went away and self-sustaining homogeneous turbulence was also lost. Buttke postulated that this was also why Schwarz's code produced homogeneity: using a coarse mesh spacing inadvertently produced these spurious vortex loops at reconnection sites, which helped sustain turbulence. This was not such a bold assumption. Buttke had tested Schwarz's numerical algorithm and found similar spurious vortices he found in his own code (Buttke, 1987). He did not explicitly state, though, that he used Schwarz's recommended reconnection ansatz.

Schwarz (1987) responded that he investigated the reconnections in his program and found no such spurious vortices. Schwarz referred Buttke to his previous paper on the reconnection process (Schwarz, 1985), which stated that the reconnection should be initiated prior to the formation of these sharp cusps and performed as an instantaneous exchange of vortex heads and tails. Naturally, eliminating the cusps where spurious vortices form, should eliminate the spurious vortices, themselves. As opposed to varying spacing with the average fluid velocity, Schwarz (1985) varied point spacing along the vortex, adding a large number of points in the vicinity of a reconnection site. Schwarz (1987) also stated that he obtained homogeneous turbulence in a wide range of point spacings, the empirical method of finding the effect of point spacing on his results.

This raised the question of why Schwarz's code could sustain homogeneous turbulence and Buttke's could not. Schwarz (1987) highlighted a phenomenon inhibiting turbulence in Buttke's simulations, the open-orbit problem. Both scientists had been using periodic boundary conditions for their simulations. To quote Schwarz (1987): “One artificial feature of periodic boundary conditions is that closed vortex loops can reconnect to themselves to form infinite, open lines.” Since vortices grow in planes perpendicular to the driving velocity, when a loop reconnects with itself while straddling a periodic wall, the resultant open-orbit lines are parallel, see Figure 1.4. The local term causes these vortices to straighten, resulting in an array of parallel, straight vortices. To compensate, Schwarz added an “occasional randomizing step in which half the open lines are rotated by ninety degrees around the axis defined by the flow velocity passing through the center of the computational volume”. This

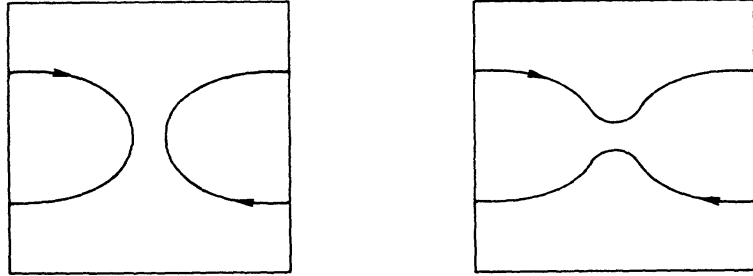


Figure 1.4: Schematic of the formation of open-orbit vortices. The vortex reconnects with itself while spanning a periodic boundary, resulting in two infinite vortices when viewed in an extended zone scheme. With the driving velocity directed into the page, the closed vortex would grow while the open-orbit vortices will not. This figure is taken from [Schwarz \(1988\)](#).

rotation allowed these parallel vortices to reconnect, breaking the system out of this pathological state. This, Schwarz claimed, was what Buttke was missing from his code. Shortly thereafter, [Schwarz \(1988\)](#) detailed this problem of forming open-orbit vortices with periodic boundaries and showed more thoroughly that the algorithm he presented matched experiment.

Admittedly, the occasional mixing step that [Schwarz \(1988\)](#) employed is far from physical. It also artificially adds randomness to the system, which [Buttke \(1987\)](#) claimed suffered from unsustainable turbulence. If this open-orbit problem was not the fundamental issue, but rather the model itself was not sufficient to sustain turbulence, it is possible for this mixing step to have only inadvertently fixed the problem. This would, of course, be cheating – if only accidentally. However, [Schwarz \(1988\)](#)

also included simulations with real-wall boundaries and no mixing step was necessary to sustain turbulence. The two simulation techniques matched with reasonable accuracy. Schwarz (1988) demonstrated that the primary features necessary for homogeneous turbulence were the vortex equation of motion, using the LIA calculation, and the vortex reconnection ansatz, where reconnections can be performed as an instantaneous exchange of the ends of each segment.

Because of the appeal that periodic boundaries hold for saving simulation time and complexity, others since Schwarz (1988) have attempted to model homogeneous He II turbulence with different techniques for dealing with the open-orbit problem (Aarts, 1993, Kondratenko et al., 2008, Adachi et al., 2010).

Aarts (1993) used the LIA calculation and a similar reconnection ansatz to Schwarz (1988). However, Aarts (1993) noticed that the open-orbit problem has a delayed onset. After the system has equilibrated, there is a length of time before the vortices decay into this open-orbit state. Aarts (1993) simply used this intermediate time domain for performing averages over different characteristics of homogeneous turbulence. Kondratenko et al. (2008) also used the LIA but attempted a modified reconnection procedure, where the velocity of vortex segments near a reconnection site are considered before reconnections are allowed to proceed. Although Kondratenko et al. (2008) claims success, I take issue with these reported results in Chapter 3. Adachi et al. (2010) presented the most physical and the most successful approach to the open-orbit problem. Unlike previous studies, Adachi et al. (2010) did not merely use the LIA calculation, but compared this to results using the full Biot-Savart integral. The nonlocal nature of the Biot-Savart calculation, not

only prevented degenerating into the open-orbit state, but also produced significant deviations from the LIA approach. Adachi et al. (2010) concluded that the LIA method was inadequate for simulating homogeneous turbulence. We, on the other hand, sought more nuance to this statement. LIA and the full Biot-Savart integral represent two ends of a spectrum. In Chapter 3, we investigate the degree to which nonlocality is necessary to accurately model homogeneous He II turbulence. Then, in Chapter 4, we take a geometric approach to the open-orbit problem by simulating superfluid turbulence on the 3-sphere.

1.4 References

- Aarts, R. *A numerical study of quantized vortices in He II*. PhD thesis, Eindhoven University of Technology (1993).
- Adachi, H., Fujiyama, S., and Tsubota, M. *Physical Review B*, **81**, 1 (2010).
- Arms, R. J. and Hama, F. R. *The Physics of Fluids*, **8**, 553 (1965).
- Barenghi, C. F., Donnelly, R. J., and Vinen, W. F. *Journal of Low Temperature Physics*, **52**, 189 (1983).
- Buttke, T. F. *A Numerical Study of Superfluid Turbulence in the Self-Induction Approximation*. PhD thesis, University of California, Berkeley (1986).
- Buttke, T. F. *Physical Review Letters*, **59**, 2117 (1987).

- Feynman, R. P. *Progress in Low Temperature Physics*, volume 1. North Holland (1955).
- Kondaurova, L. P., Andryuschenko, V. A., and Nemirovskii, S. K. *Journal of Low Temperature Physics*, **150**, 415 (2008).
- Koplik, J. and Levine, H. *Physical Review Letters*, **71**, 1375 (1993).
- London, F. *Nature*, **141**, 643 (1938).
- Paoletti, M. S., Fisher, M. E., Sreenivasan, K. R., and Lathrop, D. P. *Physical Review Letters*, **101**, 15401 (2008).
- Schwarz, K. W. *Physical Review Letters*, **49**, 283 (1982).
- Schwarz, K. W. *Physical Review B*, **31**, 5782 (1985).
- Schwarz, K. W. *Physical Review Letters*, **59**, 2118 (1987).
- Schwarz, K. W. *Physical Review B*, **38**, 2398 (1988).
- Tough, J. *Progress In Low Temperature Physics*, volume VIII. North-Holland Publishing Company (1982).
- Vinen, W. F. *Proceedings of the Royal Society A*, **240**, 128 (1957a).
- Vinen, W. F. *Proceedings of the Royal Society A*, **242**, 493 (1957b).
- Vinen, W. F. *Journal of Low Temperature Physics*, **145**, 7 (2006).
- Vinen, W. F. and Niemela, J. J. *Journal of Low Temperature Physics*, **128**, 167 (2002).

Chapter 2

Numerical Simulation

In this chapter, I present details of our numerical methods. The quantized nature of superfluid vortices makes simulating turbulence in a superfluid conceptually easier than a normal fluid. Discrete points along effectively-one-dimensional filaments need to be tracked in space and iterated forward in time.

We need to use some data structure to track our points along the vortex. Either these points must be ordered, or we have to store additional data, to indicate each point's neighbors along the vortex. Vortices are able to grow, shrink and reconnect, which means that points need to continually be inserted, deleted and swapped. Storing ordered data in an array would be horribly inefficient since operations such as these would require shifting the other data within our structure. An array does, however, afford a convenient index for points along the vortex tangle. Memory is generally cheap, while processing time is more precious. So storing disordered points along with pointers to neighbors along the vortex, is the preferred choice. Efficiency is often assisted with the use of concurrent programming. Unfortunately, vortex turbulence does not easily lend itself to being parallelized. Operations performed on

some point on the vortex often depend on other neighboring points. The disordered points do not generally lie in contiguous blocks of memory, thus, making concurrent programming not terribly helpful.

2.1 A Brief History of Numerical Methods

There is another aspect of simulating homogeneous superfluid turbulence that could use some context. The numerical methods used to solve the vortex equation of motion have varied over time. As I have mentioned, [Schwarz \(1982\)](#) pioneered the model of superfluid turbulence as a dynamical system of vortices. His calculation used the local induction approximation (LIA); however, the numerical integration technique was not published until later ([Schwarz, 1985](#)). This detailed the use of a forward-Euler algorithm with a modified hopscotch technique to correct a known, periodic instability along the vortex. The algorithm is first order in the time step dt , meaning the error for each iteration of a point on the vortex is of order dt^2 . [Schwarz \(1985\)](#) used known solutions for vortex rings to analyze the stability of his algorithm. In addition, [Schwarz \(1988\)](#) was able to match experiment for homogeneous He II turbulence.

[Buttke \(1986, 1988\)](#) found two stable numerical schemes for solving the LIA calculation without the normal-fluid interaction term. When both the interaction term and reconnection ansatz were included, Buttke presented a second-order Crank-Nicolson solution, but was unable to rigorously prove stability ([Buttke, 1986](#), p. 93). He did, however, argue stability by comparing to exact solutions of the equation

of motion. As I discussed in Chapter 1.3, Buttke could not reproduce sustainable homogeneous turbulence, though this was likely due to the formation of open-orbit vortices. Two things are worth noting regarding Buttke’s techniques. Unlike others studying this system, Buttke chose not to track the position vectors for points along the vortex. Instead he tracked the tangent vector field, which he argued was likely to be simpler to integrate (Buttke, 1986, p. 10). Also, his method of adding a point along the curve was equivalent to adding a point along the straight line separating the two neighboring points (Buttke, 1986, p. 93). This is in contrast to using some smooth interpolation method, as detailed (for example) by Schwarz (1985).

Aarts (1993) used a method of integration similar to Buttke (1986), a second-order Crank-Nicolson method, and also showed stability by comparing to exact solutions. However, unlike Buttke, Aarts used a smooth interpolation routine for adding points along the vortex. Aarts also provided a nice review of various numerical integration algorithms and their stability conditions (Aarts, 1993, Section 3.2.2). Aarts was able to produce sustainable turbulence with periodic boundary conditions. (Aarts, 1993, p. 68–74) recognized the existence of the open-orbit vortex problem, explicitly disagreeing with Buttke (1987) by stating that the model (consisting of the LIA and reconnection ansatz) was indeed adequate for modeling homogeneous turbulence.

Kondratenko et al. (2008) and Adachi et al. (2010) both use a fourth-order Runge-Kutta technique for integrating the equation of motion. Both report the point spacing and time step used for these methods. Neither explicitly demonstrates stability. Unlike previous homogeneous turbulence simulations, Adachi et al. (2010) compared use of the LIA with the full Biot-Savart integral. Nevertheless, the indicator of accu-

racy that these researchers each use was empirical. By this point, the general model of Schwarz (1982) of superfluid turbulence as a dynamical system of vortices is well established. Details of this model are still being investigated, of course.

Our interest has been the open-orbit problem with superfluid turbulence in periodic boundaries. Our vortex equation of motion is given by Equation 1.9.

$$\begin{aligned}\dot{\vec{s}}(\xi, t) &= \vec{v}_s + \beta_* \hat{s}' \times \vec{s}'' + \dot{\vec{s}}_{\text{Biot}^*} + \alpha \hat{s}' \times (\vec{v}_{ns} - \beta_* \hat{s}' \times \vec{s}'' - \dot{\vec{s}}_{\text{Biot}^*}) \\ \beta_* &= \frac{\kappa}{4\pi} \ln \left(\frac{2(l_+ l_-)^{1/2}}{e^{1/4} a_0} \right) \\ \dot{\vec{s}}_{\text{Biot}^*} &= \frac{\kappa}{4\pi} \int' \frac{(\vec{s}_o - \vec{s}) \times d\vec{\xi}_o}{|\vec{s}_o - \vec{s}|^3}\end{aligned}$$

Here, l_{\pm} are distances neighboring a point in the forward (+) and reverse (-) directions, and the nonlocal integral ranges over all vortices in the system, outside of this l_{\pm} range. We model this using a common, fifth-order Runge-Kutta-Fehlberg (RKF54) algorithm with an adaptive time step.

Runge-Kutta methods use intermediate steps to give more accurate estimate for the updated location of each point on a vortex. Since the equation of motion depends on spatial derivatives, each point depends on its neighbors. Thus, all points on one vortex must be iterated by one intermediate step before the next intermediate step can be computed. Different coefficients for the fifth-order calculation can be combined to give a fourth-order-accurate value for points on a vortex. The difference of these two calculations give us an estimate of the error in our system Δ , and the time step dt is adapted to keep this estimate under a certain bound, $\epsilon \approx 1 \cdot 10^{-4} D$, where D gives the linear size of our system. Based off of the maximum Δ for all

points in the system, the previous time step is adapted to ensure Δ will stay below ϵ during the next time step, using the following equation

$$dt_{i+1} = dt_i (\epsilon/\Delta)^{1/5}. \quad (2.1)$$

Ideally, we would like our error to be equal to ϵ . If Δ is too large, our system is inaccurate, too small and our simulation runs too slowly. Hence, if Δ is less than ϵ , the previous guess for dt was too small and is increased for next time. This discussion reveals the benefit of a higher order numerical integration technique: a larger time step can be used, allowing for shorter CPU times. However, if Δ is greater than ϵ , the previous guess for dt was too large and the updated point locations are rejected, recalculating dt to reduce the subsequent Δ . If the step size is rejected often (which empirically ours is not), the simulation can be slowed significantly. To prevent this, we multiply Equation 2.1 by a safety factor (initially 0.9 but this is decreased if a step size is rejected).

We keep our minimum point spacing a factor of about 100 times larger than this error Δ , in the numerical integration routine. The intervortex spacing is greater than this minimum point spacing, as well. The system usually contains between 1 and 10 vortices, totaling between a few hundred and several thousand points depending on the driving velocity. Time steps usually vary within the range $1 \cdot 10^{-5}$ s to $5 \cdot 10^{-4}$ s. Most importantly, we compare our results extensively to experiment and theory in Chapter 3 as the ultimate test of the accuracy of our simulation.

In addition to the numerical integration routine, we must also approximate spatial derivatives in our equation of motion. We make efforts to control truncation error in

these numerical approximations. The following section discusses our discretization of these quantities. Then in Section 2.3, I shall discuss our particular algorithms for interpolating points on the vortex. In Sections 2.4 and 2.5, I shall discuss our implementation of the nonlocal calculation and the reconnection ansatz.

2.2 Approximating Spatial Derivatives

There are certain quantities necessary for tracking vortex motion. These quantities determine the shape of the vortex, which can obviously change from point to point. This discussion deals with snapshots of the vortex at constant time, $\vec{s}(\xi, t) = \vec{s}(\xi, t_*) = \vec{s}(\xi)$, where ξ is the arclength along the vortex. The goal is to find numerical approximations for each derivative in the equation of motion, \hat{s}' , and \vec{s}'' . However, such approximations have already been found (Schwarz, 1985). Aarts (1993) finds the error in these approximations, which we include below.

$$\begin{aligned}\hat{s}' &= \frac{l_-^2 \vec{l}_+ + l_+^2 \vec{l}_-}{|l_-^2 \vec{l}_+ + l_+^2 \vec{l}_-|} + \vec{\epsilon}_0, \\ \vec{\epsilon}_0 &= -\frac{1}{6} \xi_+ \xi_- (|\vec{s}'''|^2 \hat{s}' + \vec{s}''') + \dots\end{aligned}\tag{2.2}$$

For the curvature vector, (Schwarz, 1985) reports:

$$\begin{aligned}\vec{s}'' &= a_+ \vec{l}_+ - a_- \vec{l}_- + \vec{\epsilon}_1 & (2.3) \\ a_{\pm} &= \frac{b_{\pm}}{|b_+ \vec{l}_+ - b_- \vec{l}_-|^2} \\ b_{\pm} &= \frac{1}{2} \frac{l_+^2 l_-^2 + l_{\mp}^2 (\vec{l}_+ \cdot \vec{l}_-)}{l_+^2 l_-^2 - (\vec{l}_+ \cdot \vec{l}_-)^2} \\ \vec{\epsilon}_1 &= -\frac{1}{3} (\xi_+ - \xi_-) (|\vec{s}''|^2 \hat{s}' + \vec{s}''') + \dots\end{aligned}$$

In these two numerical approximations, $\vec{l}_+ := \vec{s}_{i+1} - \vec{s}_i$ and $\vec{l}_- := \vec{s}_i - \vec{s}_{i-1}$ are the difference vectors between neighboring points in the forward (+) and reverse directions (-). Also, ξ_{\pm} is the curved point spacing between neighboring points. If we imagine a curved vortex passing through our discrete set of points, it can be shown that this spacing relates to the straight-line spacing by:

$$l_{\pm} = \xi_{\pm} - \frac{1}{24} \xi_{\pm}^3 |\vec{s}''|^2 + \dots$$

The above relations are not the only possible approximations for the vector derivatives. Aarts (1993) reports an alternative form for the curvature vector:

$$\begin{aligned}\vec{s}'' &= c_+ \vec{l}_+ - c_- \vec{l}_- + \vec{\epsilon}_2 & (2.4) \\ c_{\pm} &= \frac{2l_{\mp}}{l_+ l_- |\vec{l}_+ + \vec{l}_-|} \\ \vec{\epsilon}_2 &= -\frac{1}{12} (\xi_+ - \xi_-) (|\vec{s}''|^2 \hat{s}' + 4\vec{s}''') + \dots\end{aligned}$$

The two approximations for the curvature vector arrive from different assumptions.

tions about the shape of the curved vortex as it passes through our discrete set of points. Deciding between these different approximations requires analyzing the error in each. Notice that the error, $\vec{\epsilon}_{1,2}$, in Equations 2.3, and 2.4 are similar. The \vec{s}''' terms in each equation are identical. But the \hat{s}' term in $\vec{\epsilon}_2$ of Equation 2.4 is one-fourth that of $\vec{\epsilon}_1$. It would seem that Equation 2.4 gives the lesser error, however, this turns out not to be the case.

Let us look at the $\vec{\epsilon}_1$ component along \hat{s}' :

$$\vec{\epsilon}_1 \cdot \hat{s}' = -\frac{1}{3}(\xi_+ - \xi_-) \left(|\vec{s}''|^2 \hat{s}' \cdot \hat{s}' + \vec{s}''' \cdot \hat{s}' \right) + \dots$$

Since we parametrize using the arclength, the tangent vector is of unit length (see Appendix C): $\hat{s}' \cdot \hat{s}' = 1$. We can differentiate this twice, to obtain the relation: $\hat{s}' \cdot \vec{s}''' = -|\vec{s}''|^2$. This exactly cancels the $\hat{s}' \cdot \hat{s}'$ term. So, the \hat{s}' component of $\vec{\epsilon}_1$ cancels to first order in ξ_{\pm} . This does not happen in $\vec{\epsilon}_2$ because of the factor of 4 in the \vec{s}''' term. The first order error in $\vec{\epsilon}_2 \cdot \hat{s}'$ simplifies to $+\frac{1}{4}(\xi_+ - \xi_-)|\vec{s}''|^2$.

We can look at $\vec{\epsilon}_1$ along the normal and binormal directions, \vec{s}'' and $(\hat{s}' \times \vec{s}'')$.

$$\begin{aligned} \vec{\epsilon}_1 \cdot \vec{s}'' &= -\frac{1}{3}(\xi_+ - \xi_-) \left(|\vec{s}''|^2 \hat{s}' \cdot \vec{s}'' + \vec{s}''' \cdot \vec{s}'' \right) + \dots \\ \vec{\epsilon}_1 \cdot (\hat{s}' \times \vec{s}'') &= -\frac{1}{3}(\xi_+ - \xi_-) \left(|\vec{s}''|^2 \hat{s}' \cdot (\hat{s}' \times \vec{s}'') + \vec{s}''' \cdot (\hat{s}' \times \vec{s}'') \right) + \dots \end{aligned}$$

In general, these components do not cancel; however the first \hat{s}' term is zero along both components. So, the error in the numerical approximation 2.3, does not depend on the curvature to first order in ξ_{\pm} . Note that the \hat{s}' term will also cancel in $\vec{\epsilon}_2$, along the \vec{s}'' and $(\hat{s}' \times \vec{s}'')$ directions, but the $\vec{\epsilon}_2 \cdot \hat{s}'$ component does not cancel. The

\hat{s}' term was the only term of the leading order error that differed from $\vec{\epsilon}_1$. I shall summarize the first-order error for each of Equations 2.3 and 2.3, in the orthonormal basis $(\hat{s}', \hat{s}'', \hat{s}' \times \hat{s}'')$.

$$\begin{aligned}\vec{\epsilon}_1 &= -\frac{1}{3}(\xi_+ - \xi_-)(0, \vec{s}''', \vec{s}''') \\ \vec{\epsilon}_2 &= -\frac{1}{3}(\xi_+ - \xi_-) \left(-\frac{3}{4}|\vec{s}''|^2, \vec{s}''', \vec{s}''' \right)\end{aligned}$$

So despite first appearances, Equation 2.4 actually has greater truncation error than Equation 2.3. This also means that the first order error in Equation 2.4 depends on the local curvature at each point, but Equation 2.3 does not. We should expect that the biggest difference between these approximation equations is when they are used on the curviest parts of the vortex. Note that similar arguments apply to our tangent vector equation, so that the error in Equation 2.2 when written in the orthonormal basis $(\hat{s}', \hat{s}'', \hat{s}' \times \hat{s}'')$, reduces to:

$$\vec{\epsilon}_0 = -\frac{1}{6}\xi_+\xi_-(0, \vec{s}''', \vec{s}'''),$$

which is second order in the curved point spacing, ξ_{\pm} , and independent of the curvature vector.

Until now, I have dealt specifically with truncation error in these approximations. However, rounding error can also be crippling to an algorithm. To demonstrate this, let us look at the subtraction of two numbers in finite precision, where each number contains some error. In general, this error could come simply from their finite-precision representation, or from previous calculations. I will represent the

stored floating-point version of our numbers with tildes, \tilde{x} , and the exact versions without. So, a generic floating-point number can be written as, $\tilde{a} = a(1 + \Delta a)$. If we wish to calculate $x = a - b$, the relative error in x is given below (Higham, 2002).

$$\left| \frac{x - \tilde{x}}{x} \right| = \left| \frac{-a\Delta a - b\Delta b}{a - b} \right| \leq \max(|\Delta a|, |\Delta b|) \frac{|a| + |b|}{|a - b|}.$$

The relative error in something even as seemingly innocuous as the subtraction of two numbers becomes very large when $|a - b| \ll |a| + |b|$. The phenomenon is referred to as catastrophic cancellation. Note, however, that this error can still be small if the errors, Δa and Δb , are very small. Thus, finite precision operations bring previous errors into prominence. Since a relative error accumulates with each floating-point operation, it is not hard to understand that slightly different forms of an equation can have different errors. Simply performing operations in a different order, even if they are mathematically equivalent with infinite precision, changes the error with finite precision calculations.

We can empirically test the error in the curvature approximations Equations 2.3 and 2.4, and various ways of representing them. The curvature dependence in $\vec{\epsilon}_2$ gives a way to analyze the behavior of these methods. The angle between two adjacent difference vectors gives a simple parameter to characterize the curvature magnitude. A bigger angle means a bigger curvature at that point. This can be done rather simply by comparing the curvatures for a range of angle values and looking for divergences in the magnitudes. We find empirically that Equation 2.4 is a worse approximation than Equation 2.3 at higher curvatures. This matches the truncation error dependence we previously deduced. However, for very straight vortex segments, those with smaller

angles and thus smaller curvatures, Equation 2.4 is actually more numerically stable! Since the leading order truncation error should still be better for Equation 2.3, regardless of the curvature vector, this fact is either due to rounding error or higher-order truncation error. Rounding error does seem likely. Equation 2.3 is significantly more complicated, and each mathematical operation accumulates more error. So the subtractions involved in Equation 2.3 are more prone to catastrophic cancellation when the vortex is very straight. Thus, we use Equation 2.3 for the majority of vortex configurations. But we use the simpler Equation 2.4 for configurations where neighboring vortex segments are very nearly parallel.

2.3 Spatial Resolution

We now have approximations for our spatial derivatives, but to actually discretize our vortex, we have to establish the point spacing. There is a trade-off between speed and accuracy. If we use too few points, our approximations for the spatial derivatives are worse. But with a fine spacing, we have to store and compute the motions of too many points for our simulations to finish in a reasonable time. If we use an adaptive point spacing, however, we can have more detail in the regions of highest curvature, where more refinement is needed, and less detail for straighter sections, where it is not needed. Thus, we make our point spacing in the region surrounding some point, \vec{s}_i , dependent on the radius of curvature at that point.

We want several points to exist along some region of a certain radius of curvature. Aarts (1993) suggests the point spacing be $R/10 < l_{\pm} < R/5$. Recall that l_{\pm} is the

straight-line point spacing in front of and behind some point on the vortex. In practice, we have to satisfy this for all points and since the radius of curvature varies from point to point, conflicts arise. So to smooth out the spacing, we use the average radius of curvature to define the cutoff point spacings. So, if a point spacing is greater than our maximum we add a point. If it is less than the minimum, we delete a point. Here again, conflicts can arise where a point could be added, then removed repeatedly. So, we extend our lower point spacing limit to $R/12$, to avoid this. We favor a more detailed model of our vortex. If we imagine a semicircular region of a vortex with radius, R , there should be between $\pi R/(R/5) \approx 16$ and $\pi R/(R/12) \approx 37$ points on the semicircle, which should be more than adequate to capture future variations that occur across that vortex segment. We have also implemented maximum and minimum limits to the spacing. Both of these are based off of the error in our calculations. The minimum spacing was designed to be much larger than the error in our numerical integration method. We do not want error to leak in at small scales and dominate vortex behavior. Also, we have limited the maximum point spacing so that, even for a perfectly straight vortex, we still have several points within the size of our system.

2.3.1 Interpolation

Since we can only track a finite number of points along the vortex, we have to infer what the vortex is doing in between those points. Vortices shrink, stretch and contort, so we need to add points from time to time: this is an interpolation problem. We follow the work of [Schwarz \(1985\)](#), who interpolates based on the local radii of

curvature of the vortex points in that region. An imaginary circle is passed through points neighboring the vortex segment that is larger than the maximum spacing. This is clearly not the only choice for interpolating between points on a curve. I have already mentioned in Section 2.1 that [Buttke \(1986\)](#) chose to simply add points on the straight line connecting its neighbors. This artificially increases the curvature of the vortex, however. And it is not difficult avoid this.

We want our interpolation method to have two primary features. If our new point is added between the points i and $(i + 1)$, \vec{s}_{new} gives the location to the new point:

1. The curvature vector of \vec{s}_{new} is the average of the curvature vectors of its neighboring points.

$$\vec{s}_{new}'' = \frac{1}{2}(\vec{s}_i'' + \vec{s}_{i+1}'') \quad (2.5)$$

2. \vec{s}_{new} is added halfway along the circle passing through i and $i + 1$, which has the above curvature vector, and thus has a local radius: $R_{new} = 1/|\vec{s}_{new}''|$.

[Schwarz \(1985\)](#) explicitly states these criteria. [Aarts \(1993, p. 39\)](#) goes one step further to derive the equation for the new point:

$$\vec{s}_{new} = \frac{(\vec{s}_i + \vec{s}_{i+1})}{2} + \left(\sqrt{R_{new}^2 - \frac{1}{4}|\vec{s}_{i+1} - \vec{s}_i|^2} - R_{new} \right) \hat{s}_{new}'' \quad (2.6)$$

But this equation is not quite correct: given the first criterion we want, it does not satisfy the second criterion.

With our approximations from Section 2.2 for the curvature vector, \vec{s}'' , Equations 2.3 and 2.4, we can easily find \vec{s}_{new}'' , by taking the average of those of the neighboring points. This satisfies the first criterion. For the second criterion, a circle

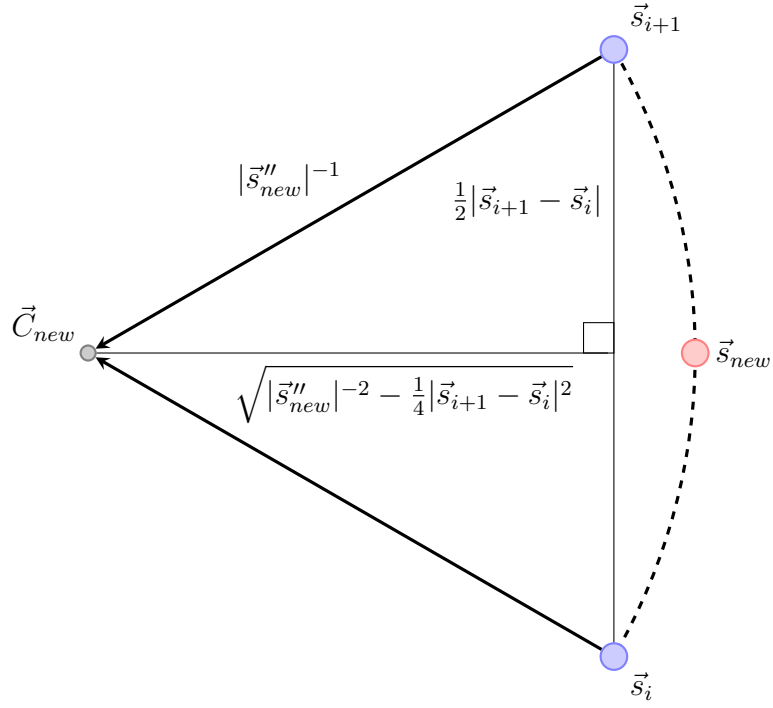


Figure 2.1: Schematic of a vortex segment for adding a point, \vec{s}_{new} . \vec{C}_{new} is the center of the circle of radius $|\vec{s}''_{new}|^{-1}$

of radius $|\vec{s}''_{new}|^{-1}$ is passed through the points \vec{s}_i and \vec{s}_{i+1} . This circle lies in the plane spanned by the vectors $(\vec{s}_{i+1} - \vec{s}_i)$, and \vec{s}'' . The geometry of the problem is shown in Figure 2.1.

Given that the midpoint of the chord of this circle is $\vec{M} = (\vec{s}_i + \vec{s}_{i+1})/2$, we can determine a vector pointing from \vec{M} to our new point, which we want to lie halfway

along the arc of the circle of radius $|\vec{s}_{new}''|^{-1}$:

$$\begin{aligned}\vec{s}_{new} - \vec{M} &= \left[|\vec{s}_{new}''|^{-1} - \sqrt{|\vec{s}_{new}''|^{-2} - \frac{1}{4}|\vec{s}_{i+1} - \vec{s}_i|^2} \right] (-|\vec{s}_{new}''|^{-1}\vec{s}_{new}'') \\ \vec{s}_{new} &= (\vec{s}_i + \vec{s}_{i+1})/2 + \left[\sqrt{|\vec{s}_{new}''|^{-2} - \frac{1}{4}|\vec{s}_{i+1} - \vec{s}_i|^2} - |\vec{s}_{new}''|^{-1} \right] |\vec{s}_{new}''|^{-1}\vec{s}_{new}''\end{aligned}\quad (2.7)$$

This is the same as Equation 2.6, which is incorrect because it assumes that the new curvature vector is perpendicular to the chord $\vec{l} = (\vec{s}_{i+1} - \vec{s}_i)$. This is not generally true. To show that it does not have to be so, let us look at a simple scenario. Figure 2.2 shows a particular vortex configuration where \vec{s}_i has zero curvature and that of \vec{s}_{i+1} is nonzero. The vortex segment, \vec{l} , is positioned along the \hat{y} axis, with its midpoint at the origin.

The two criteria are that the new point's curvature vector must be the average of \vec{s}_i'' and \vec{s}_{i+1}'' , and that the new point must be added halfway along the circular arc connecting these two neighboring points. The first criterion requires that \vec{s}_{new}'' has some negative \hat{y} component. However, the second criterion requires the new point to be added somewhere on the $+\hat{x}$ axis. Thus, the new curvature vector cannot be perpendicular to $\vec{l} = (\vec{s}_{i+1} - \vec{s}_i)$. This is easy enough to fix. Before forming the unit curvature vector from the incorrect Equation 2.6, we should remove the component parallel with \vec{l} , then normalize. The modified unit vector is labeled $\hat{s}_{new,\perp}''$. The correct equation for interpolating points becomes:

$$\vec{s}_{new} = \frac{(\vec{s}_i + \vec{s}_{i+1})}{2} + \left(\sqrt{R_{new}^2 - \frac{1}{4}|\vec{s}_{i+1} - \vec{s}_i|^2} - R_{new} \right) \hat{s}_{new,\perp}''.\quad (2.8)$$

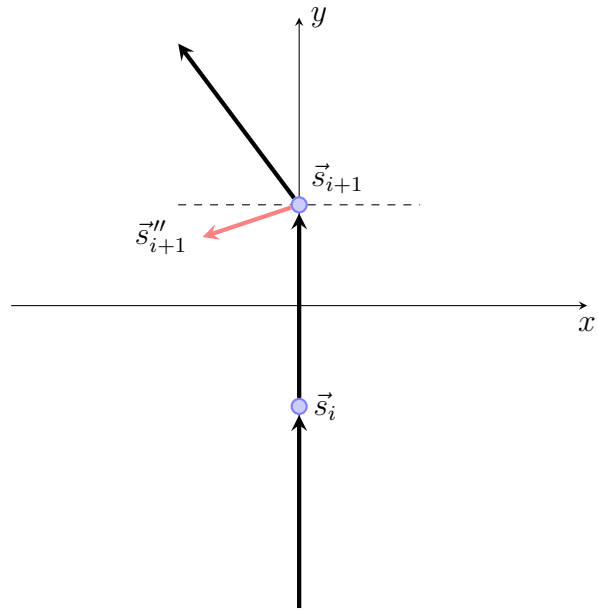


Figure 2.2: An example configuration of a vortex region, demonstrating that the curvature of a new point is not generally perpendicular to the vortex segment, $\vec{l} = (\vec{s}_{i+1} - \vec{s}_i)$. The dashed line is inserted as a guide to the eye.

It should be noted that, while Aarts (1993) used the incorrect equation for adding points, we have tested both and it makes little difference to the resultant data.

2.4 Nonlocal Interactions

The vortex equation of motion, Equation 1.9, also contains the nonlocal part of the Biot-Savart law.

$$\dot{\vec{s}}_{\text{Biot}^*} = \frac{\kappa}{4\pi} \int' \frac{(\vec{s}_o - \vec{s}) \times d\vec{\xi}_o}{|\vec{s}_o - \vec{s}|^3}$$

In general, this is fairly straight-forward to calculate. A point on the vortex, the “field” point at $\vec{s}_i = \vec{s}$, is subject to the nonlocal field from all “source” vortex segments, $d\vec{\xi}_o$, at position \vec{s}_o . These are all outside of the field point’s immediate neighbors, since the neighboring segments are included in the local term. We approximate each source vortex segment as a straight line and integrate over this straight segment. Then we sum the velocity contributions at \vec{s}_i , from all segments, to get the total. In an attempt to minimize the accumulated rounding error in this sum over the vortex, we employ compensated summation (Higham, 2002).

For N points along the vortex tangle, this process is $\mathcal{O}(N^2)$ in the number of computations. This was why Schwarz (1982) and many others discarded the nonlocal term and employed the LIA calculation, only. As we first noted in Chapter 1.3, Adachi et al. (2010) demonstrated the importance of the nonlocal field. We measure its degree of importance by truncating the range of the nonlocal integral, $|\vec{s}_o - \vec{s}|$. By only including a nonlocal field where $|\vec{s}_o - \vec{s}|$ is less than some nonlocal interaction distance, d_{NL} , we can greatly reduce the number of computations.

2.5 Reconnections

The final crucial aspect of the code that I shall discuss is the vortex reconnection ansatz. This is also a nonlocal phenomenon, the only nonlocal effect included when making the LIA calculation. Schwarz (1985) investigated the simulation of these reconnections. During a reconnection the approaching vortex segments form sharp cusps which touch at the reconnection site. This can be computationally expensive to simulate since additional points will be added in the high-curvature region.

Vortices in experiment touch and exchange segments preserving the orientation of each vortex. This phenomenon is not governed by the equation of motion. So, eventually, a simulation must contain some procedure for manually swapping these vortex heads and tails. This whole process happens very rapidly, so Schwarz (1985) concluded that given the initial and final states of the reconnection, it is sufficient to bypass much the formation of this cusp and simply exchange vortex ends when vortex segments approach within some critical distance. If we associate each point with the vortex segment in front of it, and consider that vortex points i and j are being considered for reconnection. The critical distance, below which a reconnection occurs is given by:

$$\Delta_{ij} = 2R_{min}/\ln(R_{min}/a_0),$$

where R_{min} is the minimum local radius of curvature between the two points, i and j . Physically, this distance can be derived analytically as the separation between two semi-circular vortex segments when the local field equals the nonlocal field. However, in practice, Δ_{ij} is on order of the point spacing. We do maintain a maximum Δ ,

similar to how we have an absolute minimum and maximum point spacing. For very straight vortex segments, with large local radii, we need to ensure reconnections do not occur beyond a certain range. We also take care to ensure that vortex reconnections conserve line length. Since the reconnection ansatz is an artificial smoothing of the resultant vortex segments, it is, otherwise, possible to alter the line length of the system.

Selecting which vortex segments will reconnect is a matter of finding the vortex points closest to each other amongst all points within the tangle. More precisely, we need to find all the points within Δ_{ij} of each other. And for those that are this close to multiple points, we need the closest pair of this set (which are not adjacent on the same vortex, of course). Managing points can be difficult. Here, we opt for simplicity without sacrificing too much efficiency. We do not want to check every pair of points, which would require N^2 comparisons. Instead, when checking vortex reconnections for some point i , another point j may be d farther than the maximum reconnection distance, Δ . Even if the vortex aligns along the line connecting i and j , which is unlikely, the point i could not connect with any other point in this region of the vortex near j , until we have traversed d along the vortex. Skipping this length of vortex allows us to avoid calculating Δ_{ij} for significant sections of the vortex tangle.

The particular numerical implementations described throughout this chapter apply generally to both our calculations with periodic boundaries, in Chapter 3, and on the 3-sphere, in Chapter 4. However, for the latter geometry, as one might expect, several adaptations need to be made, which I shall, then, discuss further.

2.6 References

Aarts, R. *A numerical study of quantized vortices in He II*. PhD thesis, Eindhoven University of Technology (1993).

Adachi, H., Fujiyama, S., and Tsubota, M. *Physical Review B*, **81**, 1 (2010).

Buttke, T. F. *A Numerical Study of Superfluid Turbulence in the Self-Induction Approximation*. PhD thesis, University of California, Berkeley (1986).

Buttke, T. F. *Physical Review Letters*, **59**, 2117 (1987).

Buttke, T. F. *Journal of Computational Physics*, **76**, 301 (1988).

Higham, N. J. *Accuracy and Stability of Numerical Algorithms*. Society for Industrial and Applied Mathematics, 2nd edition (2002).

Kondaurova, L. P., Andryuschenko, V. A., and Nemirovskii, S. K. *Journal of Low Temperature Physics*, **150**, 415 (2008).

Schwarz, K. W. *Physical Review Letters*, **49**, 283 (1982).

Schwarz, K. W. *Physical Review B*, **31**, 5782 (1985).

Schwarz, K. W. *Physical Review B*, **38**, 2398 (1988).

Chapter 3

Periodic Boundaries

For this chapter, we have investigated the problem of simulating homogeneous superfluid turbulence with periodic boundary conditions first described in detail by [Schwarz \(1988\)](#).

For a brief review of the history, He II can be described by a two-fluid model, comprised of a normal fluid part, with velocity v_n , and a superfluid part, with velocity v_s . At small velocities, the superfluid exhibits remarkable properties such as the ability to flow without dissipation. But above some critical velocity, turbulence sets in and new interactions must be accounted for. [Schwarz \(1982\)](#) provided a major breakthrough in understanding superfluid turbulence as a tangle of vortex filaments, an idea first suggested by [Feynman \(1955\)](#) and investigated by [Vinen \(1957\)](#). Each vortex filament is an effectively one-dimensional curve that the superfluid flows around. Because the superfluid is incompressible, $\nabla \cdot \vec{v}_s = 0$, the flow field due to these vortices is given by the Biot-Savart law. Kelvin's theorem tells us that vortices move at approximately the local superfluid velocity, meaning that the motion of each segment of the vortex is given by the positions of all vortices in the tangle.

An additional interaction term between the superfluid vortex and the normal fluid gives us the vortex equation of motion, so that the full equation of motion is given by:

$$\begin{aligned}\dot{\vec{s}}(\xi, t) &= \vec{v}_s + \dot{\vec{s}}_{\text{Biot}} + \alpha \hat{s}' \times \left(\vec{v}_{ns} - \dot{\vec{s}}_{\text{Biot}} \right) - \alpha' \hat{s}' \times \left[\hat{s}' \times \left(\vec{v}_{ns} - \dot{\vec{s}}_{\text{Biot}} \right) \right]. \quad (3.1) \\ \dot{\vec{s}}_{\text{Biot}}(\xi, t) &= \frac{\kappa}{4\pi} \int \frac{(\vec{s}_o - \vec{s}) \times d\vec{\xi}_o}{|\vec{s}_o - \vec{s}|^3}\end{aligned}$$

Here, $\vec{s}(\xi, t)$ is the position of each point along the vortex, parametrized by the arclength, ξ . κ in the Biot-Savart law is a fundamental constant for the superfluid vortex and the integral runs over all vortices within the tangle. The vector, \hat{s}' , is the unit vector tangent to the vortex filament, which $d\vec{\xi}_o$ also points along. α and α' are temperature dependent parameters characterizing the interaction between the normal fluid and the vortex core.

The Biot-Savart integral diverges as the source point, \vec{s}_o , approaches the field point, \vec{s} . So the integral is split into a local part and nonlocal part ([Arms and Hama, 1965](#), [Schwarz, 1985](#)). The local part rejects distances from the field point within about the filament core radius, a_0 , equating this with the filament's internal structure. It extends as far as l_\pm in the each direction along the vortex core. The remaining integral is included in the nonlocal part of the integral.

$$\dot{\vec{s}}_{\text{Biot}}(\xi, t) = \frac{\kappa}{4\pi} \hat{s}' \times \vec{s}'' \ln \left(\frac{2(l_+ l_-)^{1/2}}{e^{1/4} a_0} \right) + \frac{\kappa}{4\pi} \int' \frac{(\vec{s}_o - \vec{s}) \times d\vec{\xi}_o}{|\vec{s}_o - \vec{s}|^3}$$

Since the local term dominates, historically, the nonlocal part is rejected. This is called the local induction approximation (LIA). When this is done, there is no

objective best cutoff for l_{\pm} in the local term so the average radius of curvature, \bar{R} , is used, and the coefficient in front of the local term is referred to as, β , sometimes inserting a constant of order unity, c .

$$\beta := \frac{\kappa}{4\pi} \ln \left(\frac{\bar{R}}{ca_0} \right)$$

3.1 Motivation: Open-Orbit Vortices

The apparent goal that Schwarz (1982) had in mind was to establish the minimum characteristics necessary to simulate homogeneous superfluid turbulence. His code included two main features: the full Biot-Savart law was approximated by the LIA, and the only nonlocal effects came from the vortex reconnection ansatz, a rapid exchange of vortex heads and tails. Following a careful analysis of the numerical stability of simulating the equation of motion under the LIA, Buttke (1987) failed to reproduce the various signatures of homogeneous superfluid turbulence and concluded that these approximations were not adequate. Schwarz (1987) then revealed the problem we are investigating in this work, simulations of superfluid turbulence done with all boundaries periodic allow vortices to reconnect with themselves while straddling periodic walls leading to “open-orbit” vortices. This state is topologically distinct from usual superfluid turbulence since the periodic cube is equivalent to a 3-torus, and the open-orbit vortex is wrapped around one of the three holes of the 3-torus. This open-orbit vortex state prevents the usual homogeneous turbulence from developing. Schwarz (1988) expounded further both on this problem, and on his solution to this problem with periodic boundaries, and others have since recognized

it, as well (Aarts, 1993, Kondratenko et al., 2008, Adachi et al., 2010). Figure 3.1 demonstrates the vortex tangle both (a)(c) in the open-orbit state and (b)(d) with typical homogeneous turbulent behavior.

As I mentioned in Section 1.3, previous simulations have found different methods to overcome the open-orbits problem that come from periodic boundaries. Schwarz (1988), using the LIA, showed that using real-wall boundaries eliminates this problem. But periodic boundaries are much less computationally expensive and, thus, he inserted an occasional mixing step to sustain turbulence. It worked but was an ad hoc fix and certainly not physical. And it is a bit unsettling to insert randomness into the system and claim that the turbulence is self-sustaining. Aarts (1993) also used the LIA, but focused on the time domain after the superfluid system has equilibrated, but before it has degenerated into the open orbit state, as shown in Figure 3.2. Finally, the most physical solution was given by Adachi et al. (2010). They used the full Biot-Savart law, and, by comparing to LIA, argue that LIA is inadequate for simulating homogeneous superfluid turbulence. Figure 3.1 shows the difference in vortex structures for (a),(c) the LIA, and (b),(d) the full Biot-Savart calculation. As Aarts (1993) recognized, the structure in (a) and (c) does not occur right away but degenerates from one resembling (b),(d) to (a),(c) after some time.

Adachi et al. (2010) compared these two simulation techniques in multiple ways: visually (as in Figure 3.1), using the line length density given by:

$$L = \frac{1}{V} \int d\xi, \quad (3.2)$$

where V is the system volume, and with the anisotropy parameters, given by (Schwarz,

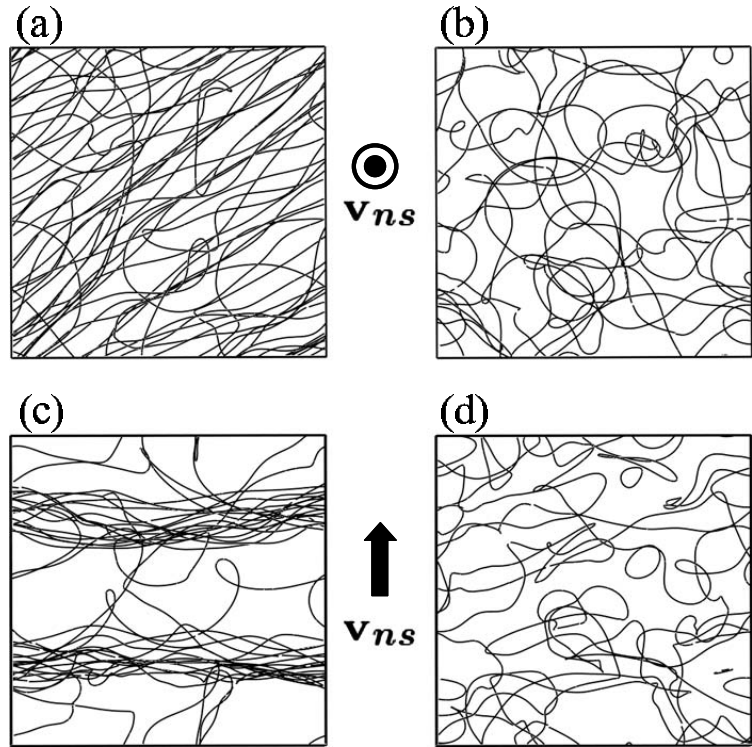


Figure 3.1: From Adachi et al. (2010): (a) Side and (c) top views of the LIA calculation. (b) Side and (d) top views of the full Biot-Savart calculation. All figures use a periodic cube with side length $D = 0.2$ cm displayed at time $t = 18.6$ s.

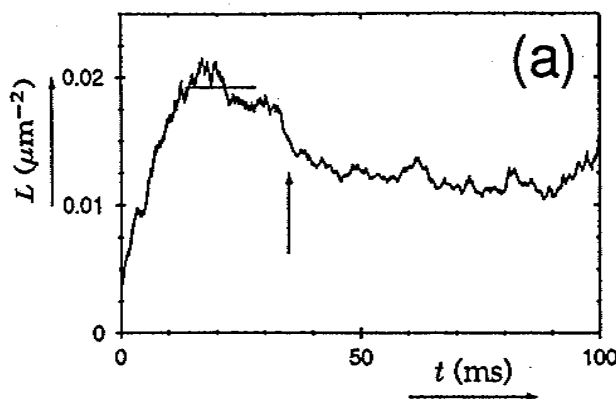


Figure 3.2: Example plot of $L(t)$, taken from [Aarts \(1993, p. 71\)](#). The upward arrow within the graph indicates when the vortex tangle degenerates into a collection of open-orbit vortices. The horizontal line indicates Aarts's time domain used for averaging $L(t)$. The periodic cube has side length $D = 0.005$ cm.

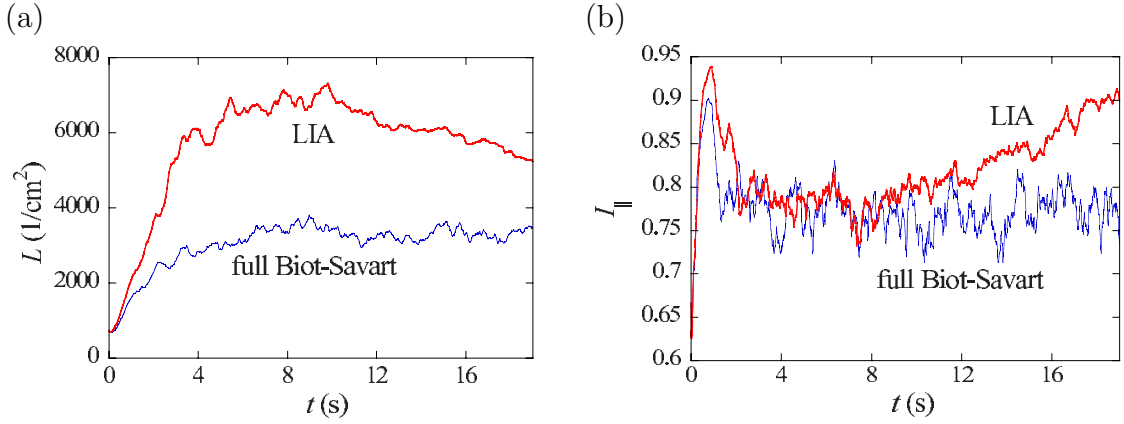


Figure 3.3: Comparison of the time evolution of the (a) L , and (b) the anisotropy parameter, $I_{\parallel}(t)$, from [Adachi et al. \(2010\)](#).

[1988](#), p. 2403):

$$I_{\parallel} = \frac{1}{VL} \int \left[1 - (\hat{s}' \cdot \hat{r}_{\parallel})^2 \right] d\xi \quad (3.3)$$

$$I_{\perp} = \frac{1}{VL} \int \left[1 - (\hat{s}' \cdot \hat{r}_{\perp})^2 \right] d\xi \quad (3.4)$$

$$I_{\ell} \hat{r}_{\parallel} = \frac{1}{VL^{3/2}} \int \hat{s}' \times \vec{s}'' d\xi. \quad (3.5)$$

Here \hat{r}_{\parallel} and \hat{r}_{\perp} are unit vectors parallel and perpendicular to the \vec{v}_{ns} direction. Note that, if a vortex tangle is completely isotropic, $I_{\parallel} = I_{\perp} = 2/3$ and $I_{\ell} = 0$. If vortices lie entirely within planes normal to \vec{v}_{ns} , $I_{\parallel} = 1$, $I_{\perp} = 1/2$, and I_{ℓ} will depend on the structure of the vortices. Also: $I_{\parallel}/2 + I_{\perp} = 1$.

Figure 3.3 shows their comparisons between calculations with the LIA and full Biot-Savart law, for $L(t)$ and $I_{\parallel}(t)$. It is clear that the LIA data deviate significantly

from those of the fully nonlocal calculation. The presence of nonlocal interactions reduces the vortex line length density. As Adachi et al. (2010) explains, the nonlocal interaction is strongest before and after a reconnection, when vortices are closest. The nonlocal term tends to repel two parallel vortex segments and attract antiparallel segments. Consequently, fewer parallel reconnections occur with the presence of the nonlocal interaction. Furthermore, reconnections between antiparallel segments produce sharp cusps that retreat away from the reconnection site quickly, due to the local velocity component. Parallel segments reconnect producing vortex segments with large radii that do not retreat quickly. The effect of nonlocal interactions is to increase intervortex separation thereby decreasing line length density. It should be noted, however, that the qualitative behavior of the LIA calculations by Adachi et al. (2010) is similar to what Aarts (1993) observed in Figure 3.2. In other words, Adachi et al. (2010) confirms that there is a region of time before the system settles into the open-orbit state.

This structural change is even more pronounced when viewing $I_{\parallel}(t)$ in Figure 3.3 (b). After some period of time, the vortex begins to align more in planes perpendicular to the driving velocity. Since, Figure 3.1 is a snapshot of the vortex tangle of Adachi et al. (2010), at $t = 18.6$ s we can see just what this looks like from (a) and (c). And, judging by the structure of this vortex tangle, this correlates with the open-orbit state first described in detail by Schwarz (1988). This is the nature of the problem which we address in this chapter.

While several researchers were able to address this problem and still match simulation and experiment (Schwarz, 1988, Aarts, 1993, Adachi et al., 2010), Adachi

et al. (2010) used the most physical solution. So, in Section 3.2 we present data using the full Biot-Savart calculation to show that our code is also in good agreement with previous simulations and experiment. Then, in Section 3.3 we present results using a range of nonlocal interaction distances, from the full Biot-Savart law to LIA, addressing, later, the argument made by Adachi et al. (2010), that LIA is an inadequate approximation. While we agree that the LIA calculation gives data which deviates significantly from the full nonlocal calculation, we find that only a small region of nonlocal interaction is enough to accurately model the system.

3.2 Reproducing Homogeneous Turbulence

Throughout this chapter, we run simulations focusing on the temperature, $T \approx 1.6$ K, which corresponds to $\alpha = 0.1$ and we ignore α' since it is an order of magnitude smaller. We primarily use a periodic cube with side length, $D = 0.005$ cm. We integrate the equation of motion using an adaptive-timestep Runge-Kutta-Fehlberg⁵⁴ routine.

3.2.1 Our Data on the Open-Orbit Problem

Our results in Figure 3.4, bear good qualitative agreement with Figure 3.3. We did however, use a different system size, leading to differences in the $\langle L \rangle$ and time scales. It should be noted that Figure 3.3 shows a factor of 2 difference between the equilibrated L of the LIA and full Biot-Savart calculations, while that difference in our results in Figure 3.4 is not nearly as pronounced. This difference is likely

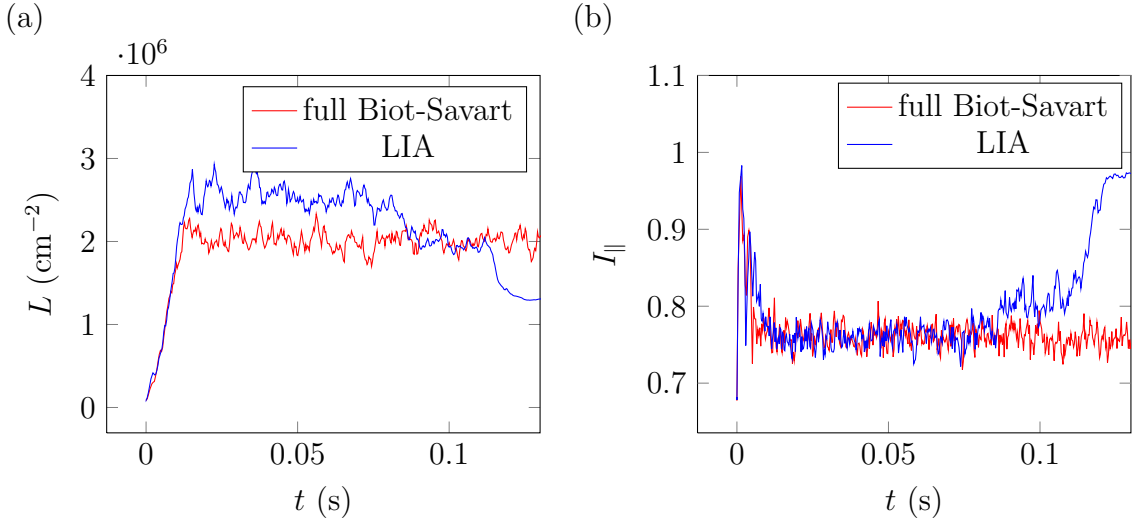


Figure 3.4: Our data comparing the use of LIA and full Biot-Savart calculations for (a) $L(t)$ and (b) I_{\parallel} , with $v_{ns} = 12 \text{ cm/s}$. There is good qualitative agreement between our results and those of [Adachi et al. \(2010\)](#), in Figure 3.3. Quantitative differences in $\langle L \rangle$ and time scales are partly due to different system sizes: 0.2 cm versus our 0.005 cm.

due to differences in driving velocity and other simulation parameters. Furthermore, our snapshots of the vortex tangle, itself, are in good agreement with Figure 3.1 by [Adachi et al. \(2010\)](#). This same comparison of the LIA and the Biot-Savart calculation in Figure 3.5.

Thus, our calculation shows this same open-orbit vortex problem as is found in the literature. But it is not enough to just show we can reproduce the problem. We also need to reproduce the solution to the problem.

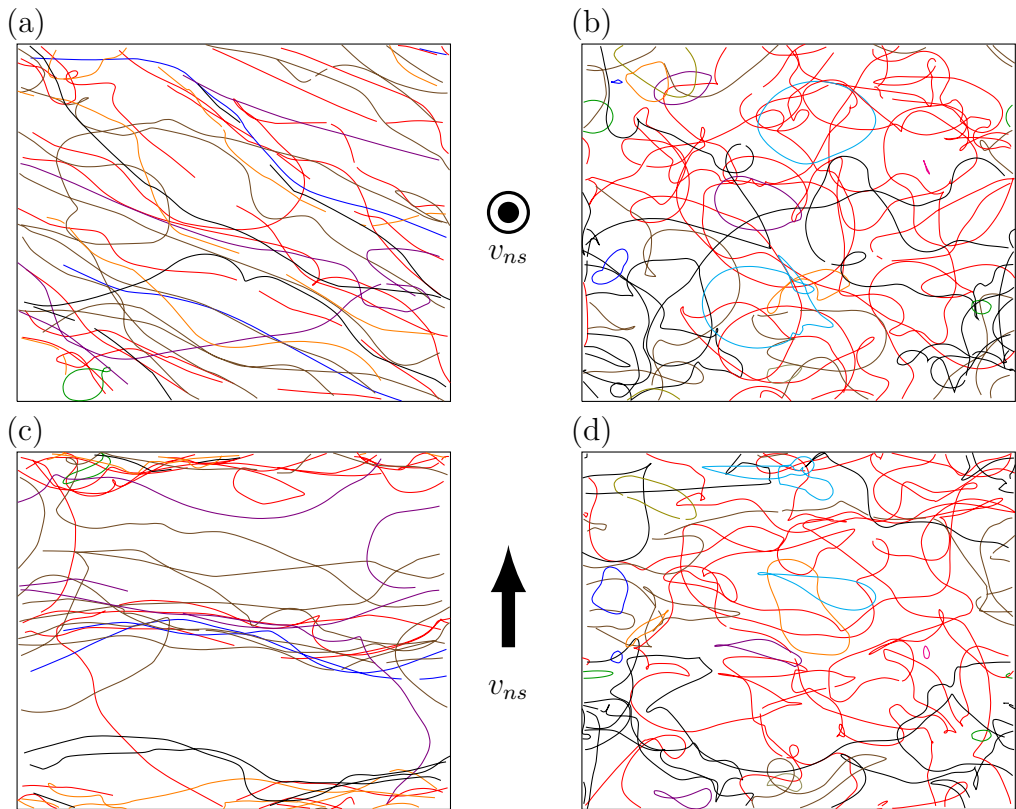


Figure 3.5: Compare to Figure 3.1. (a) Side and (b) top views of our LIA calculation, and (b) Side and (d) top views of our full Biot-Savart calculation, from Figure 3.4. All figures use a periodic cube with side length $D = 0.005$ cm displayed at time $t = 0.115$ s.

3.2.2 Reproducing the Solution: Homogeneous Turbulence

I will show comparisons to simulation and experimental results for multiple measures of homogeneous superfluid turbulence. My first task is to show homogeneity, and the simplest and most common quantity measured is the line length density, $L(t)$. Figure 3.6 shows a graph of $L(t)$ as the system evolves. The volumes used to calculate each curve are the eight, \mathbb{R}^3 octants: $\{x < 0, x \geq 0, y < 0, y \geq 0, z < 0, z \geq 0\}$. Here, our system is a periodic cube with side length $D = 0.005$ cm, and our driving velocity is (a) $v_{ns} = v_n = 6$ cm/s, and (b) $v_{ns} = v_n = 12$ cm/s. We chose $v_s = 0$, because, according to the vortex equation of motion, 3.1, the only difference that v_s has from v_n is uniform translation (as long as our velocity is chosen to be uniform, of course). Using v_n just simplifies things, so this is what we use throughout our simulations.

Figure 3.6 shows some key physical concepts. The initial growth period comes predominantly from the driving velocity transferring energy into vortex line length. Growth from interaction with the normal fluid eventually balances with energy loss due to vortex reconnections resulting in a steady-state line length density.

Our goal is to show homogeneity. Even after steady-state turbulence has set in, we expect some variation between the $L(t)$ octants, but the average, equilibrated values should be roughly the same. So Figure 3.7 shows these average equilibrated L values for each octant, for a range of driving velocities. Averages were done over the equilibrated time domain, by approximating the continuous time integral,

$$\langle X \rangle = \frac{1}{T} \int_0^T X(t) dt. \quad (3.6)$$

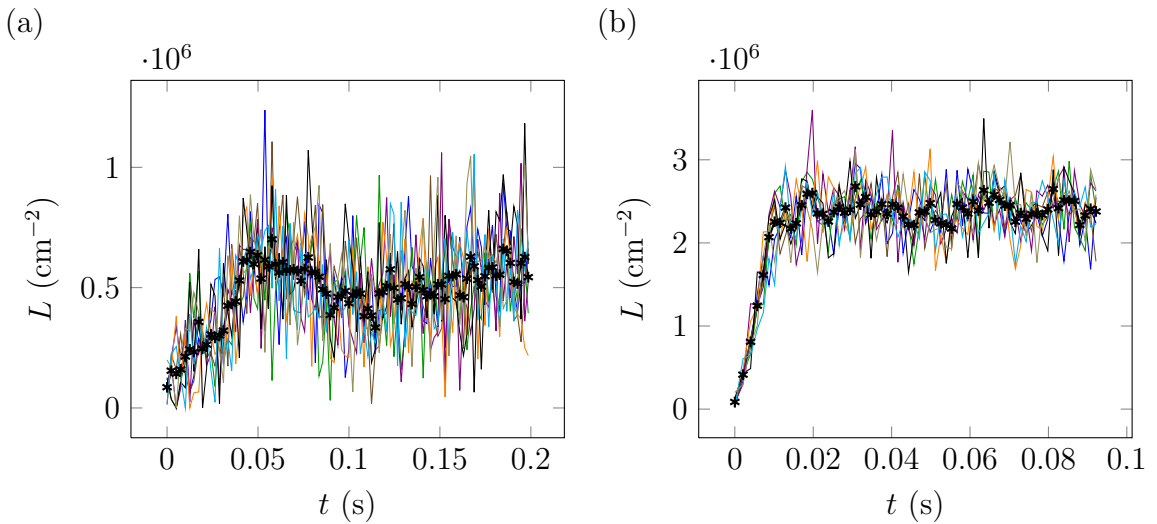


Figure 3.6: Evolution of the vortex line length density, $L(t)$, within each octant of the periodic cube, with total side length $D = 0.005$ cm. The curves in each figure marked by ---*--- , give the line length per total system volume, D^3 . Each other curve in (a) and (b) gives $L(t)$ for one of the eight, \mathbb{R}^3 octants: $\{x < 0, x \geq 0, y < 0, y \geq 0, z < 0, z \geq 0\}$. The applied velocity is (a) $v_{ns} = v_n = 6$ cm/s, and (b) $v_{ns} = v_n = 12$ cm/s.

Notice the bracket notation which I will use to indicate a time average. Contrast this with averages performed on quantities that vary over the length of the vortex, such as the local radius of curvature, R . For these, I will use the notation:

$$\bar{R} = \frac{1}{VL} \int R(\xi) d\xi, \quad (3.7)$$

where ξ is the arclength along the vortex, and L is, again, the line length density, which is why we include V the system volume. This integral is performed over all vortices. Judging from Figure 3.7, it is clear that our system is homogeneous at every velocity.

Other Indicators of Homogeneity

Showing homogeneity is just a prerequisite. It is conceivable that our simulation produces homogeneous turbulence that behaves, somehow, differently than experiments and simulations that have come before us. Approximate scaling arguments such as can be achieved through simple dimensional analysis (see Appendix D for more details) tell us that homogeneous turbulence should depend on the driving velocity as:

$$\langle L \rangle = c_L^2 (v_{ns}/\beta)^2, \quad (3.8)$$

where c_L is a commonly-cited, temperature-dependent quantity. Aarts (1993, p. 72), uses a linear fit of $\langle L \rangle^{1/2}$ versus v_{ns} , which I will reproduce in Figure 3.8, but in our units.

It appears that Aarts also constrains the y -intercept of his fit to be zero. Al-

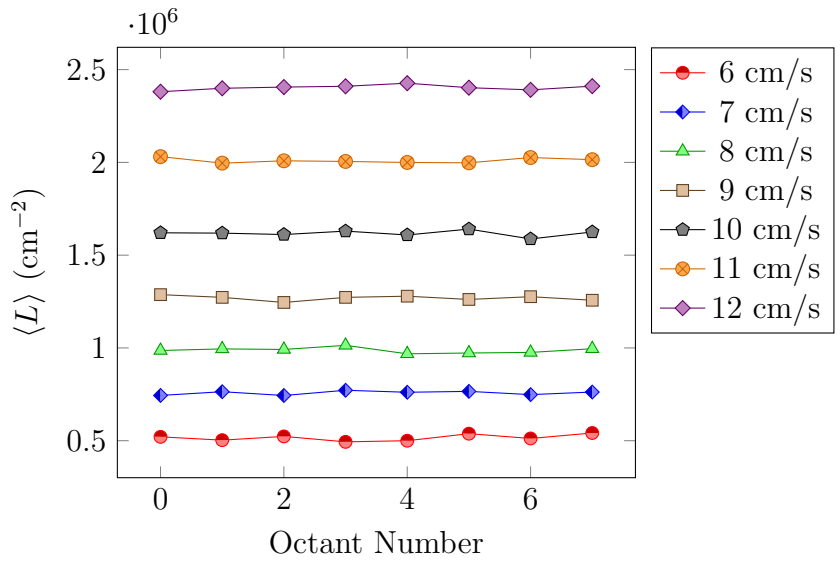


Figure 3.7: Average equilibrated line length density, $\langle L \rangle$, within each octant of the periodic cube, with total side length $D = 0.005$ cm, at multiple velocities. This graph shows we have homogeneity at all velocities.

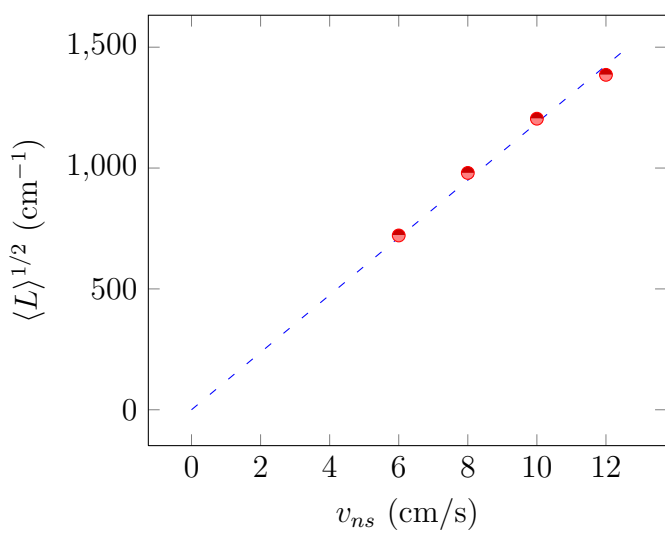


Figure 3.8: Average $\langle L \rangle^{1/2}$ from [Aarts \(1993, p. 72\)](#), displayed in our units. Simulation was performed in a periodic cube with side length, $D = 0.005$ cm.

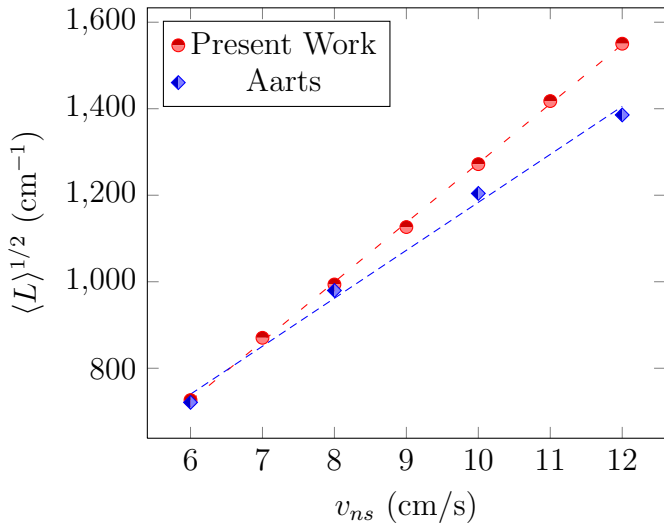


Figure 3.9: Comparison of line length density calculations to [Aarts \(1993\)](#). Our periodic cube, like Aarts's, has side length $D = 0.005$ cm.

though it appears a good fit, doing so is unnecessary. A nonzero intercept is frequently seen in experiment ([Tough, 1982](#)). Thus a better fit could be obtained by leaving this intercept unconstrained. We fit both our data and that of Aarts with an intercept, in Figure 3.9.

Experimental results support a negative intercept, which is in line with our data. Aarts's results show a positive y -intercept, though it may be that the data set presented in his dissertation was not sufficient to get an accurate measure of this value. There is another reason why one should not constrain the y -intercept to be zero. [Swanson and Donnelly \(1985\)](#) presented demonstrated that the relation between $\langle L \rangle$ and v_{ns} involves the logarithmic term in β and so it does not scale linearly. [Schwarz \(1988, p. 2414\)](#) also addressed this. $\langle L \rangle^{1/2}$ in Equation 3.8 is

not proportional to v_{ns} with constant slope and no y -intercept, because β is not constant. β depends logarithmically on the average local radius of curvature, which decreases with increasing velocity. This is why Schwarz (1988) fits either $\langle L \rangle^{1/2}$ versus a reduced $v_{ns,0} = v_{ns}/\beta$, or $\beta\langle L \rangle^{1/2}$ versus v_{ns} . When Schwarz (1988) applies this correction factor to the experimental data presented in Martin and Tough (1983), the intercept disappears. I have included Schwarz's demonstration, as Figure 3.10.

For an equivalent comparison to Aarts (1993), who does not track β in every trial, we use the relation $\beta = (\kappa/4\pi) \log(1/c\langle L \rangle^{1/2}a_0)\langle L \rangle^{1/2}$ suggested by Schwarz (1988), where c is a constant of order unity, and apply it to both our data and that presented by Aarts (1993). This modification to the data is shown in Figure 3.11. Our modified data match Schwarz's interpretation of the intercept, while Aarts's still retain a nonzero intercept value. However, this may be no more than an artifact of the few, somewhat noisy, data points that Aarts presented for these trials. Since this leads to less than a 10% error in Aarts's fit parameters, we will continue to compare to Aarts's reported values.

The linear fit of our data in Figure 3.11 gives us the slope, $c_L = 0.106$. This dimensionless parameter is a commonly viewed characteristic of homogeneous superfluid turbulence.

The mutual friction force by the normal fluid on the superfluid is another quantity which is often compared, most often reported as per unit volume instead of per unit line length. This force results in the interaction term of the vortex equation of motion

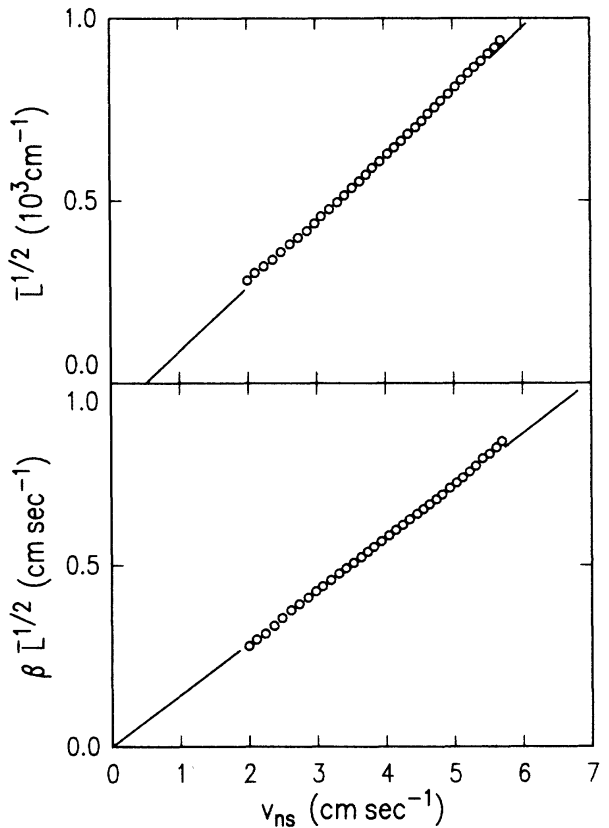


Figure 3.10: Figure 26 from Schwarz (1988, p. 2414). Above shows the data of Martin and Tough (1983), before Schwarz's logarithmic scaling. Below shows the same data after this scaling is applied.

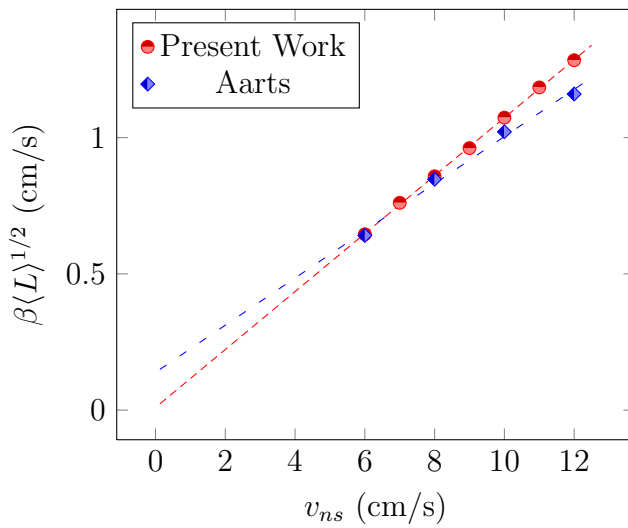


Figure 3.11: A modified version of Figure 3.9, a logarithmic scale factor has been applied to test for removal of the intercept, as per the interpretation in [Schwarz \(1988\)](#). The linear fit of our data yields a slope of $c_L = 0.106$.

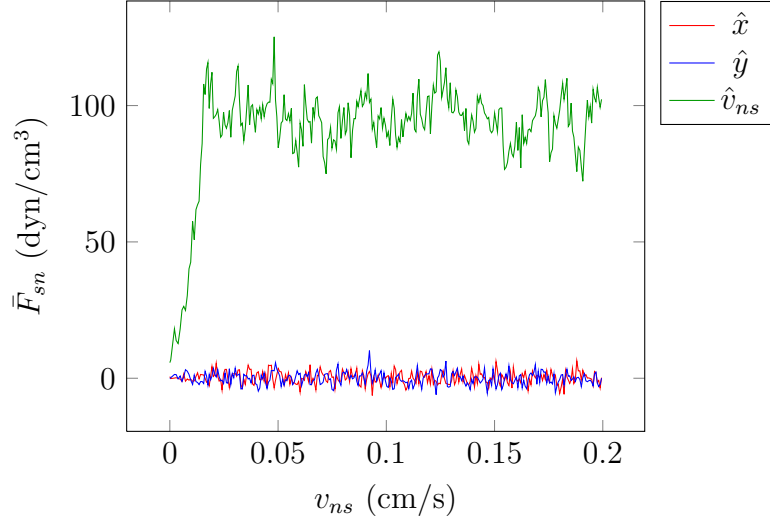


Figure 3.12: The average mutual friction force density along the three primary axes, for an example trial, with $v_{ns} = 9$ cm/s, and periodic cube with side length $D = 0.005$ cm.

and is perpendicular to the velocity that results.

$$\vec{F}_{sn} = -\frac{\rho_s \kappa}{V} \hat{s}' \times \vec{v}_{fric}, \quad (3.9)$$

where V is the system volume. When averaged along the entire vortex, the driving velocity, \vec{v}_{ns} , is the only thing that picks out a preferred direction. So it is expected that only \bar{F}_{sn} along this direction will be non-negligible. The averages along all three directions are included for an example trial in Figure 3.12. Schwarz (1988) also developed a scaling relation for \bar{F}_{sn} , finding that $\bar{F}_{sn} \propto v_{ns}^3 / \beta^2$. Similar to Aarts

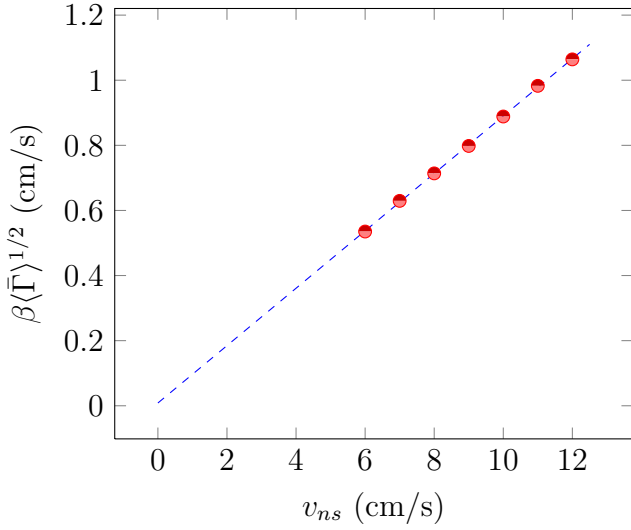


Figure 3.13: The quantity $\langle \bar{\Gamma} \rangle$ taken from the mutual friction force density, \bar{F}_{sn} along \hat{v}_{ns} . The periodic cube has side length, $D = 0.005$ cm. The linear fit of this data yields a slope of $c_F = 0.088$.

(1993), I will construct a new quantity:

$$\bar{\Gamma} := \frac{\bar{F}_{sn}}{\rho_s \kappa \alpha v_{ns}}. \quad (3.10)$$

This way, similar to before, we can fit $\beta \langle \bar{\Gamma} \rangle^{1/2}$ versus v_{ns} and expect it to be linear with no y -intercept, as shown in Figure 3.13. Our data obeys Schwarz's scaling relation for \bar{F}_{sn} , yielding a slope of $c_F = 0.088$.

Yet another quantity reported describing homogeneous superfluid turbulence is

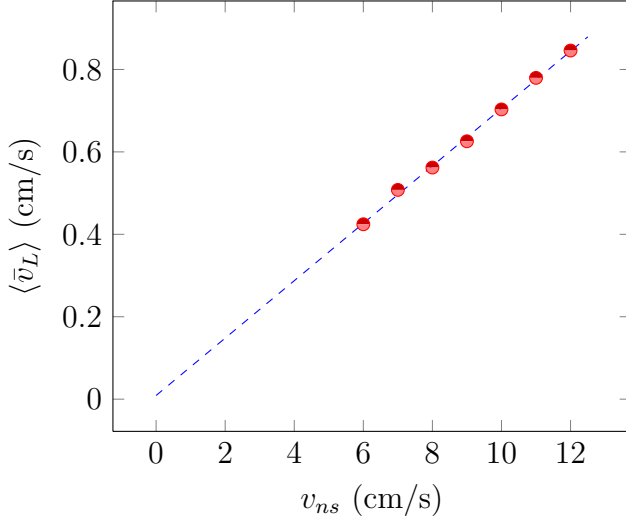


Figure 3.14: The average vortex velocity, \bar{v}_L . The periodic cube has side length, $D = 0.005$ cm. The linear fit of this data yields a slope of $c_v = 0.070$.

the average vortex velocity (relative to the applied superfluid velocity \vec{v}_s):

$$\bar{v}_L = \left[\frac{1}{VL} \int \dot{s} d\xi \right] - \vec{v}_s. \quad (3.11)$$

Similar to \bar{F}_{sn} , the only preferred direction is that of the applied superfluid, so we expect \bar{v}_L to only be non-negligible along \hat{v}_{ns} . This time the quantity in question requires no scaling with β : $\bar{v}_L/v_{ns} = b(T)$, where $b(T)$ is a temperature-dependent parameter (Tough, 1982, p. 153), (Schwarz, 1988, p. 2404). We show our recorded data for this value in Figure 3.14.

We can easily measure these quantities from the output data. The values I report for these are averaged over the equilibrated time-domain, and they already

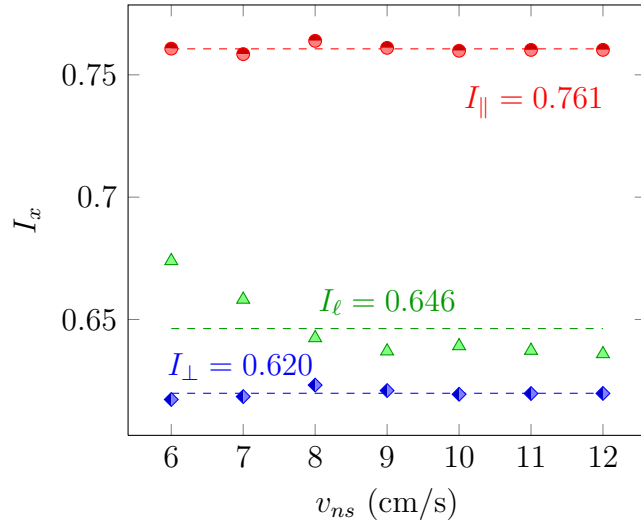


Figure 3.15: Anisotropy parameters for a range of v_{ns} . Average values over this range are shown. The periodic cube has side length $D = 0.005$ cm.

represent averages over the vortex line. But I am suppressing both the $\langle \dots \rangle$, and \bar{X} for simplicity. Figure 3.15 gives the behavior of these values over a range of driving velocities.

The anisotropy parameters stay relatively constant with v_{ns} . Only I_{ℓ} varies some initially but tends towards a uniform value. We want the average value over this range of data, which is shown in the figure. The ratio of the perpendicular and parallel anisotropy parameters, I_{\perp}/I_{\parallel} is one commonly reported quantity for homogeneous turbulence systems. But beyond this, these anisotropy measures appear in various combinations as meaningful quantities to compare to other works. Schwarz (1988) points out that the average mutual friction force density, \hat{F}_{sn} along \hat{v}_{ns} , can be written

as:

$$\bar{F}_{sn} = \rho_s \kappa \alpha (c_L^2 I_{\parallel} - c_L^3 I_{\ell}) v_{ns}^3 / \beta^2. \quad (3.12)$$

This is the relation we referred to earlier when motivating our method of fitting $\beta \langle \bar{\Gamma} \rangle^{1/2}$ in Figure 3.13 and it is precisely why we defined $\bar{\Gamma}$ the way we did in Equation 3.10. As we have defined it, then:

$$\bar{\Gamma} = (c_L^2 I_{\parallel} - c_L^3 I_{\ell}) \left(\frac{v_{ns}}{\beta} \right)^2.$$

We can see that the quantity, c_F , measured earlier from the mutual friction force density data is equal to $(c_L^2 I_{\parallel} - c_L^3 I_{\ell})^{1/2}$.

Equation 3.12 assumes, however, that we are using the LIA, which Schwarz (1988) and Aarts (1993) used but we did not. We should expect that any comparison to quantities involving I_{ℓ} should be somewhat off for this reason. Additionally, Schwarz (1988) states that, when neglecting α' , the slope parameter we call $c_v = c_L I_{\ell}$. Finally, with these relations, we can compare characteristics of homogeneous turbulence to multiple other works in Table 3.1.

In addition, Adachi et al. (2010) and Kondaurova et al. (2008) did not report values that allowed us to compare to c_L directly. They did, however, report $\gamma = c_L / \langle \beta \rangle$. Even though β decreases as v_{ns} increases, we can find the average $\langle \beta \rangle$ throughout our range of driving velocities: $\langle \beta \rangle \approx 0.0009 \text{ cm}^2/\text{s}$, in order to compare to these papers. We get a value of $\gamma = 117.8 \text{ s/cm}^2$, where Adachi et al. (2010) reports a value of $\gamma = 109.6 \text{ s/cm}^2$, in addition to comparing to an experimental value of $\gamma = 93 \text{ s/cm}^2$ from (Childers and Tough, 1976) and (Tough, 1982). We can

Source (T=1.6 K)	c_L	I_\perp/I_{\parallel}	c_F	$(c_L^2 I_{\parallel} - c_L^3 I_\ell)^{1/2}$	c_v	$c_L I_\ell$
Present Work	0.106	0.815	0.088	0.088	0.070	0.069
Aarts (1993)	0.11	-	0.095 [†]	-	0.045 [†]	-
Schwarz (1988)	0.137	0.775 [‡]	-	0.116 [†]	-	0.063 [†]

Table 3.1: Comparison of quantities characterizing homogeneous turbulence between other sources, all at T=1.6 K. Schwarz (1988) shows that our parameter, c_F is roughly equivalent to $(c_L^2 I_{\parallel} - c_L^3 I_\ell)^{1/2}$ and c_v to $c_L I_\ell$ (rough because it assumes use of the LIA). For comparison, we report all of these comparable values, using $c_{F,v}$ to indicate the direct measurement of relevant slopes of our data. The quantities with I_{\parallel} and I_ℓ were calculated directly with these parameters, for comparison. Schwarz (1988) shows that his theoretical calculations of I_\perp/I_{\parallel} , $(c_L^2 I_{\parallel} - c_L^3 I_\ell)^{1/2}$, and $c_L I_\ell$ match experiment. [†] : values were calculated from other reported values. [‡] : value was estimated from reported figure.

also extract the value for $I_\perp/I_{\parallel} \approx 0.8$ from Adachi et al. (2010), which also matches our quantity from Table 3.1 of 0.815.

Kondratenko et al. (2008) report a $\gamma = 280$ s/cm², which is extremely high, as Adachi et al. (2010) mention. Kondratenko et al. (2008) took the approach of applying the LIA, like Schwarz (1988), but modifying the reconnection ansatz such that the velocity of vortex segments near reconnection sites were considered. Reconnections could only occur if these vortex segments were expected to intersect based off of their velocities. While this is reasonable, reconnections resulting in open-orbits could still conceivably occur as a vortex grows through a boundary, back towards itself. While

they claim to have solved this open-orbit problem, their large γ begs explanation and it is conceivable they simply did not run simulations long enough. The use of the full Biot-Savart law, instituted by Adachi et al. (2010) has more plausibility and gives better results.

Kondratenko et al. (2008) also report values for the rate of vortex reconnections, an important process in carrying energy down to smaller length scales. Other simulations and analysis show the rate of vortex reconnections relates to the line length density, as $\dot{n} = C\kappa\langle L \rangle^{5/2}$, where \dot{n} is the reconnection rate per unit volume, C is a dimensionless constant on order 0.1-0.5 (Tsubota et al., 2000, Barenghi and Samuels, 2004, Nemirovskii, 2006). Kondratenko et al. (2008) reports an exponent of 5/2 and a value of $C = 2.47$. Figure 3.16 gives our data on the vortex reconnection rate for a series of trials. Analysis of this data yields an exponent of 2.47, and $C = 0.42$, well within the acceptable range.

Our full Biot-Savart calculation matches previous calculations of homogeneous superfluid turbulence through multiple comparisons. In the next section, we investigate further the claim by Adachi et al. (2010) that the LIA approximation is inadequate for reproducing homogeneous turbulence, and thus the full Biot-Savart calculation is necessary to accurately represent this behavior.

3.3 Nonlocal Interaction Distance, d_{NL}

The differences between the LIA and the full Biot-Savart calculations that we reviewed in Section 3.1, led Adachi et al. (2010) to conclude that the LIA approxi-

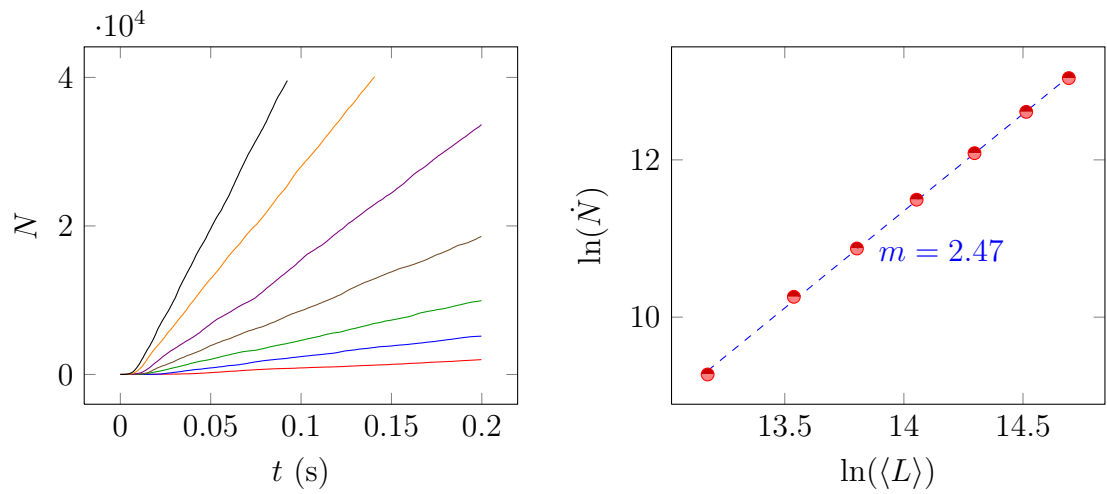


Figure 3.16: Part (a) shows the number of reconnections, N , with time for a series of trials with different velocity. Part (b) shows a plot of $\ln(\dot{N})$ versus $\ln(\langle L \rangle)$, finding the exponent of $\dot{N} = dN/dt \propto \langle L \rangle^m$, $m = 2.47$.

mation was inadequate for simulating homogeneous superfluid turbulence. We have already discussed this to some degree in Section 1.3. For one, the Adachi et al. (2010) simulations were all performed with periodic boundaries, which are known to cause issues such as open-orbit vortices. This is the origin of the deviations from the Biot-Savart results for I_{\parallel} shown in both Figures 3.3 (b) and 3.4 (b). While we can grant the authors this literary license, it would be a hasty generalization to conclude the LIA calculation is insufficient for all system geometries, from this discrepancy alone. Beyond this, we have reviewed some successful attempts at overcoming this periodic boundary problem, which let us retain LIA and all of its computation-savings, such as those by Schwarz (1988) and Aarts (1993). However, as I have mentioned and as Adachi et al. (2010) have pointed out, this was not the only issue with LIA calculations. Even in the region before the open-orbit state kicked in, when the LIA system was equivalently isotropic as the full Biot-Savart system, there is a significant deviation within L . It turns out that this deviation in L still retains an approximate $\langle L \rangle \propto v^2$ behavior (Schwarz, 1988, Aarts, 1993), but the deviation in values of L remains. It is a value judgment whether or not to discard the LIA for this reason, depending on the goal of the study. If the point is to discern what are the necessary attributes of a system to produce certain behavior, as Schwarz (1982, 1988) seemed to be aiming for, this may well be an acceptable approximation. Adachi et al. (2010) saw it justified to discard the LIA for these discrepancies.

We sought a more nuanced viewpoint, so have investigated whether some degree of the computation-saving power of the LIA could be retained. To say that there is only the LIA or the full Biot-Savart law is a false dichotomy. In reality, there

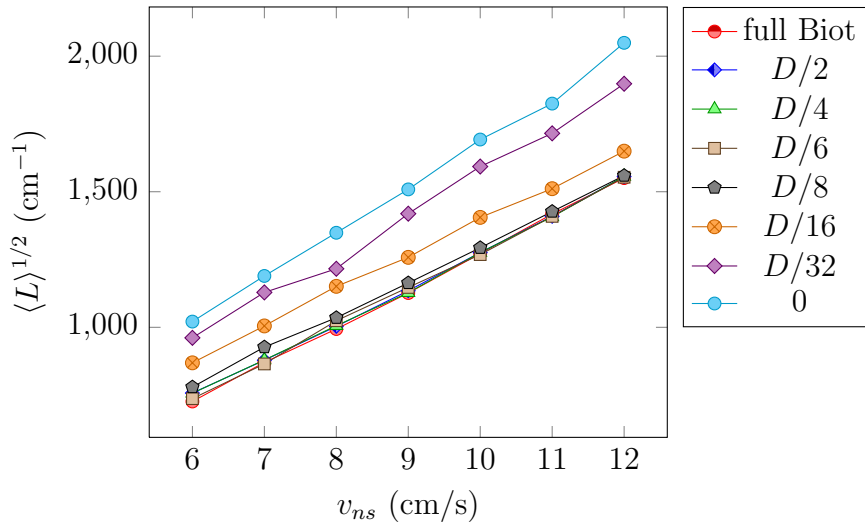


Figure 3.17: Effects of nonlocal interaction distance, d_{NL} , on the equilibrated line length density, $\langle L \rangle$. Each curve is a series of trials at the same d_{NL} , listed in the legend. The full Biot-Savart calculation has a range of $d_{NL} = \sqrt{3}D/2$. The length of a side of our periodic cube for each of these trials is $D = 0.005$ cm. Averages at each v_{ns} used the initial equilibrated range, similar to [Aarts \(1993\)](#), as in Figure 3.2.

is a continuum that we can tap into: the nonlocal interaction distance, which we denote with d_{NL} . For each point on the vortex, we only include contributions to the Biot-Savart integral, Equation 1.7, from other vortex segments that are within a distance, d_{NL} . Our results for $\langle L \rangle^{1/2}(v_{ns})$ are displayed in Figure 3.17, for a range of d_{NL} values. Our periodic cube has side length, $D = 0.005$ cm.

Figure 3.17 shows a series of curves, each at a different nonlocal interaction distance which is indicated in the legend in terms of the fraction of D , the length of one side of the periodic cube. The full Biot-Savart law has $d_{NL} = \sqrt{3}D/2$. As d_{NL} is

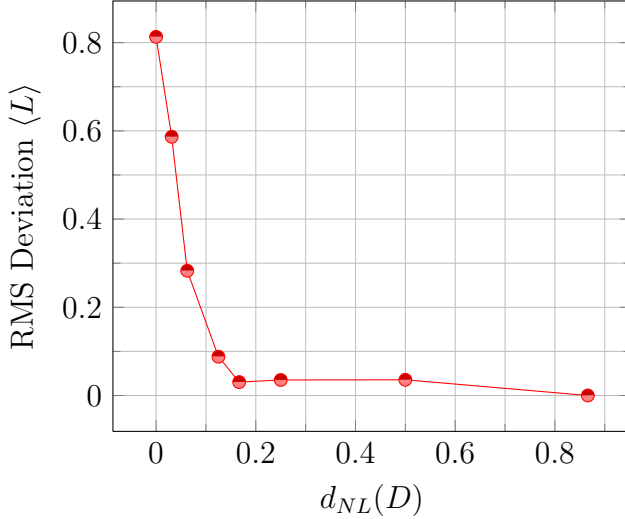


Figure 3.18: Root-Mean-Square fractional deviation of $\langle L \rangle$ from that of the full Biot-Savart calculation, for several nonlocal interaction distances, which are plotted as a factor of the length of one side of the periodic cube, $D = 0.005$ cm. The full Biot-Savart calculation has $d_{NL} = \sqrt{3}D/2 \approx 0.866$. The trials contributing to each mean came from Figure 3.17, and use the initial equilibration region for finding the average $L(t)$.

decreased over successive trials, the data still retains a remarkable similarity to that using the full Biot-Savart law, for quite a while. Eventually, a difference develops, though at what d_{NL} is hard to see from this figure. It becomes more distinct if we view the root-mean-square deviation of $\langle L \rangle^{1/2}$ from that of the full Biot-Savart calculation, over all velocities in one curve. Figure 3.18 shows how this quantity varies with d_{NL} .

Figure 3.18, shows good agreement between the full Biot-Savart calculation and

those performed with an interaction distance truncated to between $D/6$ and $D/8$. To be sure that we have a robust measure of when such a discrepancy from full nonlocality occurs, we wish to reduce the amount of subjective influences into the data as much as possible. These time averages all used the initial region of equilibration before the characteristic drop in $L(t)$, seen in Figures 3.2 and 3.4, i.e. before the degeneration into the open-orbit state occurs, which happens at the lower d_{NL} values. However, the transition between large and small d_{NL} in Figure 3.18 required making judgement calls about what time domain to include in the averages, which were not as clear as at the extreme d_{NL} values. And note that including only the initial region biases our time averages in a systematic way toward a higher $\langle L \rangle$. It would be nice to know that this trend still holds up without inserting the subjectivity of when to exclude data. If we take note of the fact that a decrease in $L(t)$ also leads to an increase in the standard deviation of our $L(t)$ distribution, we can fit the entire equilibrated time domain and use the standard deviation of $L(t)$ as a parameter for measuring deviation from the full Biot-Savart calculation. We will also show the same data in Figure 3.18 but with this new averaging region. Also, looking at Figures 3.3 and 3.4, since I_{\parallel} only deviates from the full Biot-Savart value outside of the initial equilibrated range, we can now use this quantity and its standard deviation, as well. There is still a limited sample of data, since we do not run trials forever. And we still have to pick out a time when the data starts to equilibrate. But these are unavoidable, so we have at least reduced our biases to the degree that we can. Figure 3.19 shows these quantities with the full equilibrated time domain used for averaging.

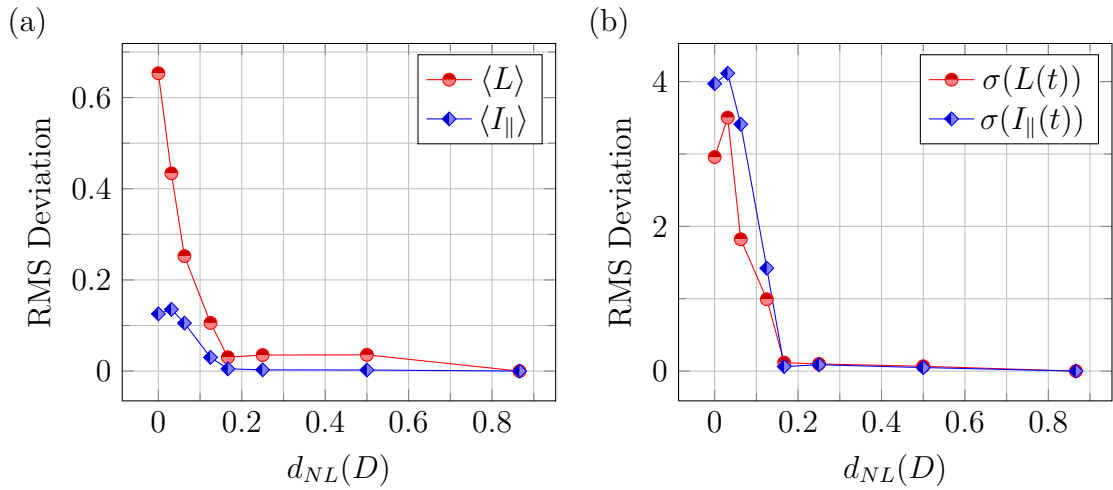


Figure 3.19: Root-Mean-Square fractional deviation of (a) $\langle L \rangle$ and $\langle I_{\parallel} \rangle$, and (b) the standard deviations of $L(t)$ and $I_{\parallel}(t)$, from that of the full Biot-Savart calculation, for several nonlocal interaction distances, which are plotted in terms of the length of one side of the periodic cube, $D = 0.005$ cm. The full Biot-Savart calculation has $d_{NL} = \sqrt{3}D/2$. Averages use the entire equilibration time domain. Compare $\langle L \rangle$ in (a) to Figure 3.18 to see effect of new choice in time domains used for averaging.

Figure 3.19 (a) shows that including the entire equilibrated range into the averages of $L(t)$ and $I_{\parallel}(t)$ still shows a transition in how good our truncated Biot-Savart integral is at $d_{NL} = D/6$. Part (b) indicates that the standard deviations of $L(t)$ and $I_{\parallel}(t)$ are very good parameters for measuring this critical d_{NL} . Notice the magnitude of the increase in $\sigma(L(t))$ and $\sigma(I_{\parallel}(t))$. The data are clear. We can use a small fraction of the nonlocal interaction volume ($(4/3)\pi d_{NL}^3$ when $d_{NL} \leq D/2$) and still get a very good approximation of the Biot-Savart integral for homogeneous superfluid turbulence.

Reducing the interaction distance to such a degree has the potential to provide a considerable savings in computation time. With interactions omitted beyond $D/6$, the interaction volume for each vortex segment is $\approx 1/50$ of the full Biot-Savart calculation. The nonlocal calculation has a growth rate $\mathcal{O}(N^2)$, where N we can think of as the number of vortex segments (or points) in our system. We still need to perform the calculation for each segment, but in the homogeneous regime, for each segment there are $1/50$ the number of other vortex segments contributing to the nonlocal velocity. Since computation time varies significantly with system load and hardware I will simply report that it was common for the program to run in $1/3$ to $1/10$ the computation time with the reduced interaction region.

We still need to be sure how this critical interaction distance, $D/6$, varies with system size. Just because I have presented it as a fraction of the dimension of our cube does not mean it necessarily scales that way. We simulated turbulence in two other system sizes, but all other parameters the same. $\langle L \rangle$ data for all three system sizes is shown in Figure 3.20. The fact that there is such good agreement

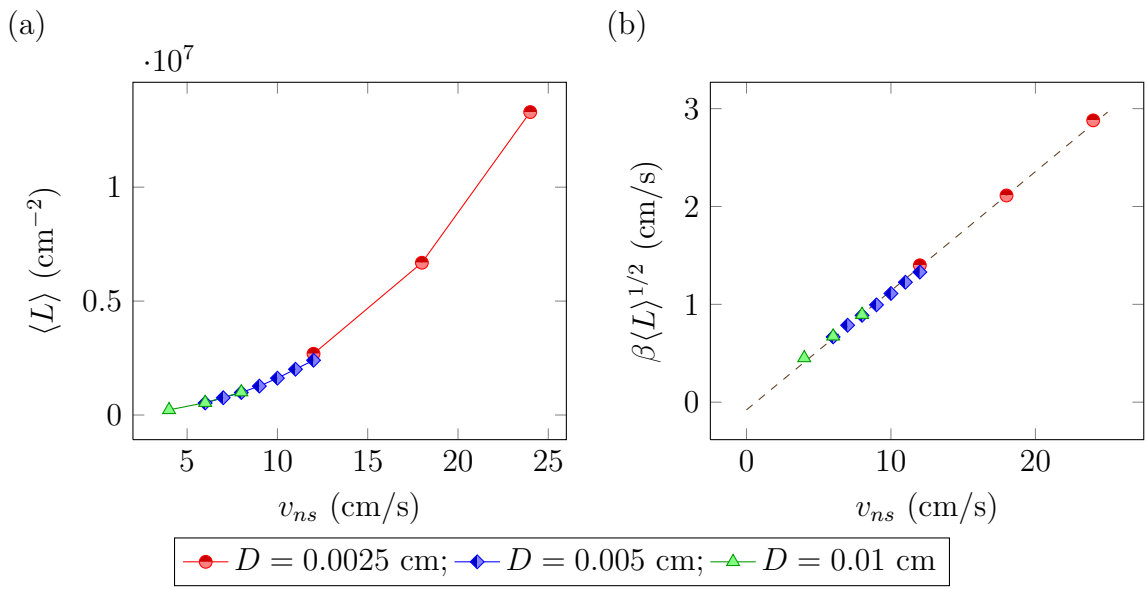


Figure 3.20: (a) $\langle L \rangle$ and (b) $\beta \langle L \rangle^{1/2}$ data for all system sizes, $D = 0.01$, 0.005, and 0.0025 cm.

on $\langle L \rangle$ for different system sizes is another mark of homogeneity. Since $\langle L \rangle$ is an intensive quantity, with a homogeneous system it must be independent of system size. Figure 3.21 shows the same quantities as Figure 3.19 but for $D = 0.0025$ cm and $D = 0.01$ cm.

Figure 3.21 shows that $D = 0.0025$ cm and $D = 0.01$ cm have quantitatively similar behavior with d_{NL} as does $D = 0.005$ cm, in Figure 3.19. $\langle L \rangle$ and I_{\parallel} vary by only approximately 5% from the fully nonlocal trials, until d_{NL} drops below $D/6$ and the standard deviations in these values stay similar to fully nonlocal trials until the same distance. From this, we can say that the interaction distance at which we regain the full Biot-Savart results should be approximately linear with system size, D . Any deviations from linearity should be small, given the factor of four change in D from 0.0025 cm to 0.01 cm with no detectable change in this critical d_{NL} .

It is not enough to know that including a nonlocal interaction out to $D/6$ will approximate fully-nonlocal, homogeneous, superfluid turbulence and still allow us to use periodic boundaries, saving us the hassle and computation time of simulating boundary walls. Why $D/6$? What is the physical significance of this distance?

First, I would like to justify averaging over all v_{ns} values. We can view the indicators $\sigma(L)$, and $\sigma(I_{\parallel})$ as we vary the driving velocity, v_n , within each interaction distance, d_{NL} . This breakdown of the data shown in Figure 3.22.

The deviation from the fully nonlocal calculation sets in at the highest velocities first, as d_{NL} is decreased. Apparently, higher velocities exacerbate any discrepancies from the full Biot-Savart law. But from a practical perspective, we want to choose an interaction distance such that every driving velocity we use produces turbulent

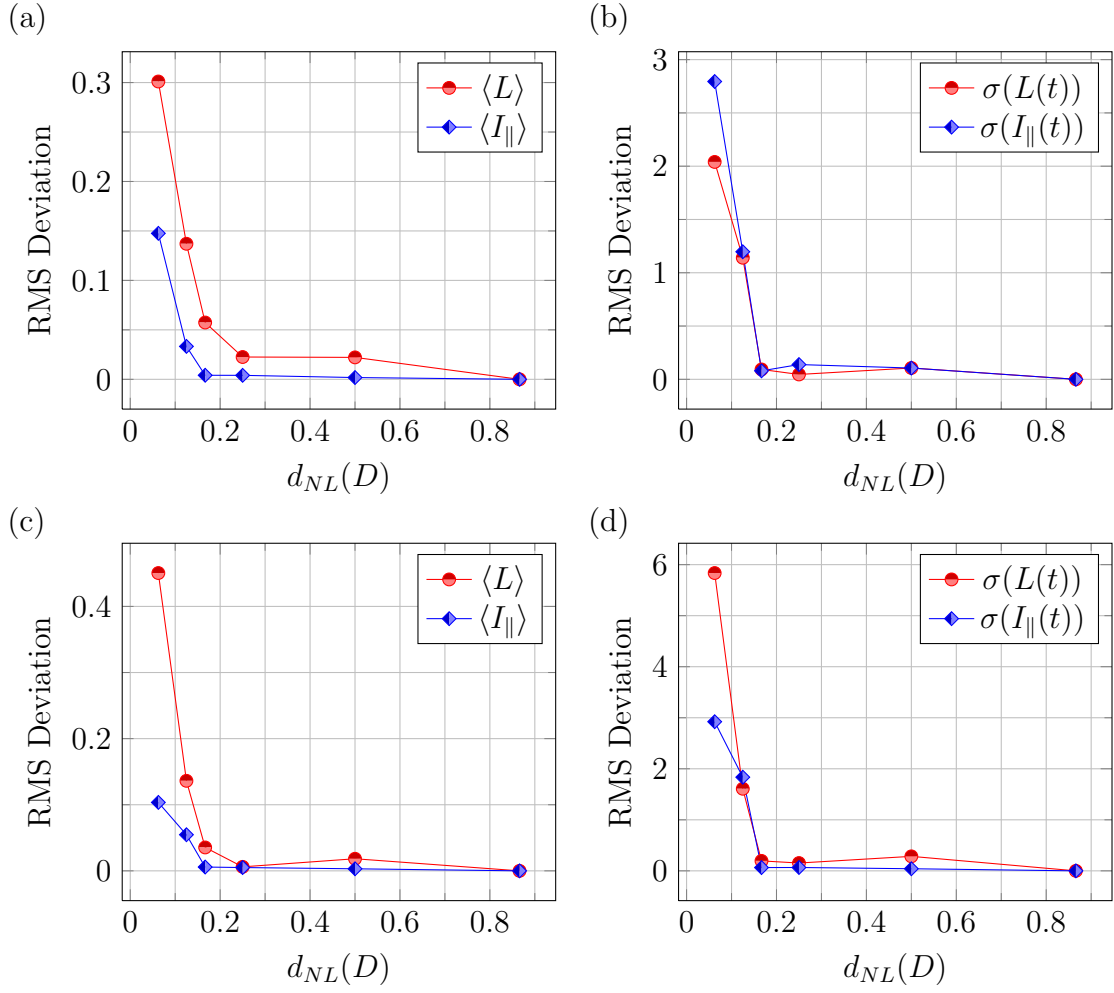


Figure 3.21: For comparison with Figure 3.19: Figures (a) and (b) have system side-length $D = 0.0025$ cm, while Figures (c) and (d) have side-length $D = 0.01$ cm. Root-Mean-Square fractional deviation of (a), (c) $\langle L \rangle$ and $\langle I_{\parallel} \rangle$, and (b), (d) the standard deviations of $L(t)$ and $I_{\parallel}(t)$, from that of the full Biot-Savart calculation, for several nonlocal interaction distances, d_{NL} , which are plotted as a factor of the length of one side of the periodic cube. The full Biot-Savart calculation has $d_{NL} = \sqrt{3}D/2$. Averages use the entire equilibration time domain.

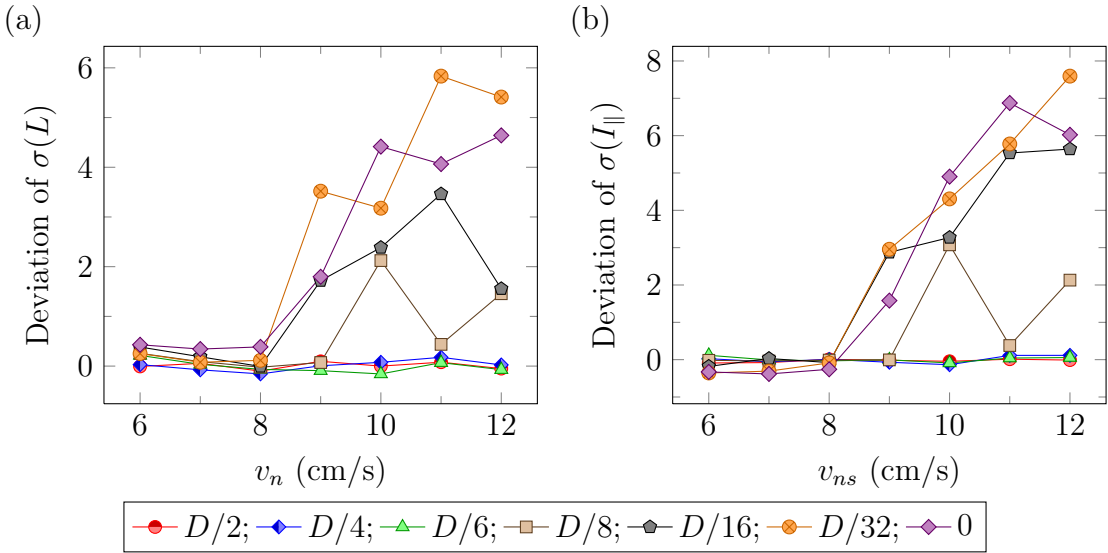


Figure 3.22: Fractional deviation of the standard deviations (a) $\sigma(L(t))$, and (b) $\sigma(I_{\parallel}(t))$, from that of the full Biot-Savart calculation as a function of driving velocity, v_{ns} . Each curve is a different nonlocal interaction distance, d_{NL} . The system size is $D = 0.005$ cm. The full Biot-Savart calculation has $d_{NL} = \sqrt{3}D/2$. Averages use the entire equilibration time domain.

behavior that matches that of the full Biot-Savart law. The root-mean-square over all velocities at one d_{NL} will pick out deviations at any v_{ns} , and helps simplify the search for the physical source of this critical $d_{NL} \lesssim D/6$.

A simple argument can be made that the important physical length scale should be the average intervortex distance, which we can get from $\langle \ell \rangle = \langle L \rangle^{-1/2}$. Adachi et al. (2010) found that the nonlocal interaction prevents turbulence from degenerating into this open-orbit state, which they described as having a “layered structure”. This state is what causes deviation from the full Biot-Savart calculation. Once the extent of the nonlocal interaction is too short to actually allow vortices to interact, we regain this open-orbit problem. The quantity $(\langle \ell \rangle - d_{NL})/D$ should serve as a useful indicator of whether we expect to deviate from the fully nonlocal calculation. The fractional root-mean-square deviation of $\langle L \rangle$, $\sigma(L)$, $\langle I_{\parallel} \rangle$, and $\sigma(I_{\parallel})$ from the full Biot-Savart calculation is plotted versus this quantity in Figure 3.23.

Figure 3.23 shows very good agreement. As the nonlocal interaction distance is decreased to the average vortex separation distance, interactions between vortices cannot prevent the system from falling into the open-orbit state. The simulation starts to deviate strongly from the full Biot-Savart law. So, as $\langle \ell \rangle - d_{NL}$ approaches 0, we can no longer accurately simulate superfluid turbulence.

3.4 References

Aarts, R. *A numerical study of quantized vortices in He II*. PhD thesis, Eindhoven University of Technology (1993).

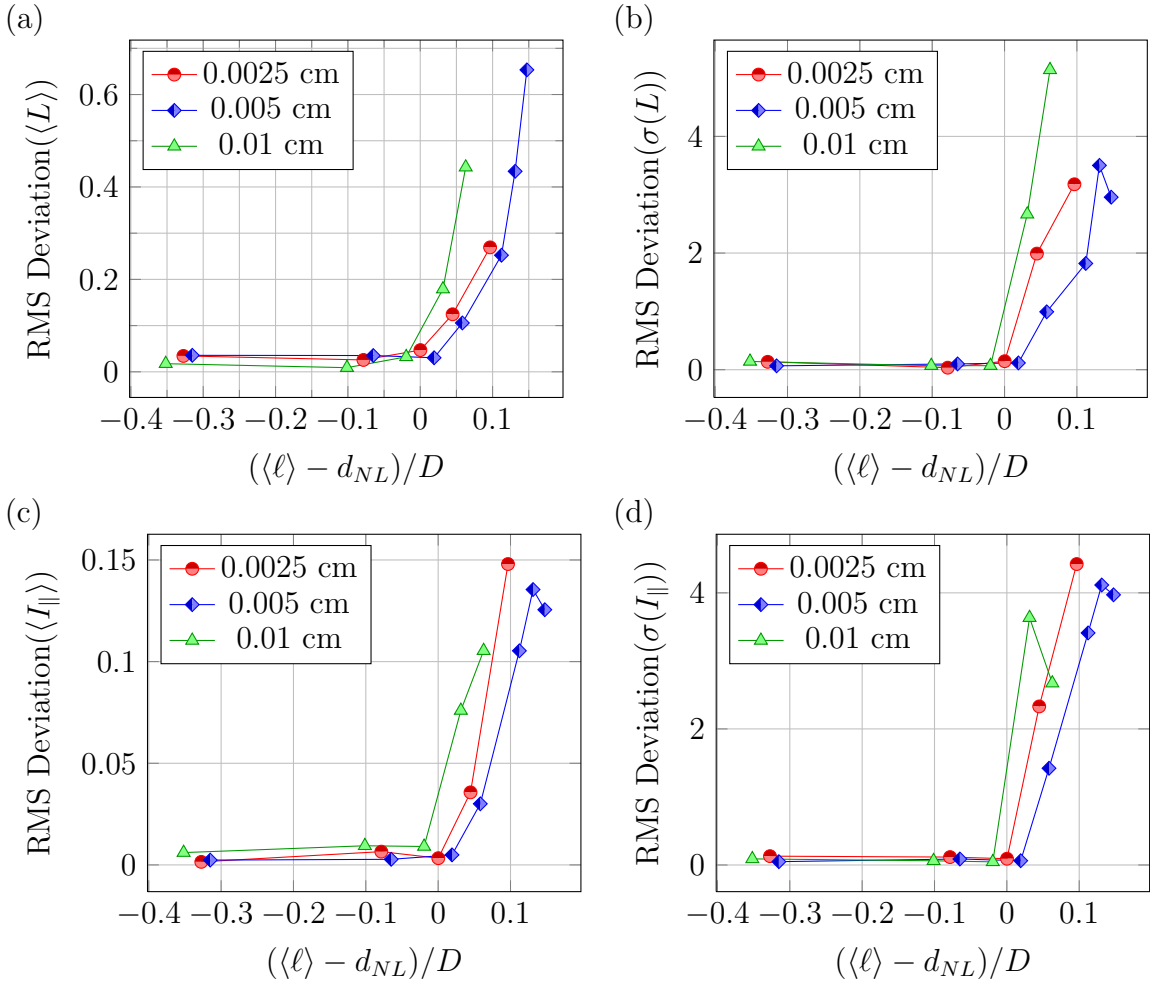


Figure 3.23: Root-Mean-Square fractional deviation of (a), (c) $\langle L \rangle$ and $\langle I_{||} \rangle$, and (b), (d) the standard deviations of $L(t)$ and $I_{||}(t)$, from that of the full Biot-Savart calculation. Each curve within a graph is for a different system size, $D = 0.0025$ cm, $D = 0.005$ cm, and $D = 0.01$ cm. Every point within a curve gives the data from all v_{ns} trials for a single interaction distance, d_{NL} . The factor of $1/D$, simply scales the data so they are easier to view in the same graph.

- Adachi, H., Fujiyama, S., and Tsubota, M. *Physical Review B*, **81**, 1 (2010).
- Arms, R. J. and Hama, F. R. *The Physics of Fluids*, **8**, 553 (1965).
- Barenghi, C. and Samuels, D. *Journal of Low Temperature Physics*, **136**, 281 (2004).
- Buttke, T. F. *Physical Review Letters*, **59**, 2117 (1987).
- Childers, R. K. and Tough, J. T. *Physical Review B*, **13**, 1040 (1976).
- Feynman, R. P. *Progress in Low Temperature Physics*, volume 1. North Holland (1955).
- Kondaurova, L. P., Andryuschenko, V. A., and Nemirovskii, S. K. *Journal of Low Temperature Physics*, **150**, 415 (2008).
- Martin, K. P. and Tough, J. *Physical Review B*, **27**, 2788 (1983).
- Nemirovskii, S. *Physical Review Letters*, **96**, 015301 (2006).
- Schwarz, K. W. *Physical Review Letters*, **49**, 283 (1982).
- Schwarz, K. W. *Physical Review B*, **31**, 5782 (1985).
- Schwarz, K. W. *Physical Review Letters*, **59**, 2118 (1987).
- Schwarz, K. W. *Physical Review B*, **38**, 2398 (1988).
- Swanson, C. E. and Donnelly, R. J. *Journal of Low Temperature Physics*, **61**, 363 (1985).

Tough, J. *Progress In Low Temperature Physics*, volume VIII. North-Holland Publishing Company (1982).

Tsubota, M., Araki, T., and Nemirovskii, S. *Physical Review B*, **62**, 11751 (2000).

Vinen, W. F. *Proceedings of the Royal Society A*, **242**, 493 (1957).

Chapter 4

3-sphere

4.1 Motivation

As we have seen thus far, simulating superfluid turbulence in periodic boundary conditions can carry baggage. This is the open-orbit problem addressed in Chapter 3. On the other hand, it lets us avoid treating the walls in a special way. It also lets us have a larger volume of homogeneous turbulence, so our system does not have to be as big. The open-orbit state is topologically distinct from normal vortices motion. There is no way for the vortex to deform continuously and get out of the open-orbit state under the action of the equation of motion. Only another topological event can do this: a vortex reconnection.

Ways of dealing with this problem have progressed to the point that we now have a system that behaves physically, without any ad hoc mechanism of dealing with open-orbit vortices. Adachi et al. (2010) implemented the full Biot-Savart calculation, as opposed to using the local induction approximation (LIA), and this nonlocal interaction prevents the open-orbit state from forming. In Chapter 3.3, I

discussed our method of recovering much of the savings that the LIA calculation afforded without sacrificing accuracy. A nonlocal interaction that extends to about the average intervortex distance, $\langle \ell \rangle$, is sufficient to accurately model homogeneous superfluid turbulence.

There is another approach to this problem of simulating homogeneous turbulence, which is in some ways more obvious. The open-orbit vortex state is completely topologically different from normal vortex behavior because the vortex surrounds one of the one-dimensional holes of the periodic cube: the flat 3-torus. A one-dimensional curve cannot continuously deform to a point when it surrounds one of the 3-torus's three holes. If topology got us into this mess, what could a new topology do to address it? Unlike the 3-torus, the 3-sphere (S^3) is simply-connected. It is plausible that the 3-sphere would not suffer from such an anomaly as the open-orbit problem. In this chapter, I shall discuss our investigation of the 3-sphere as an alternative geometry for simulating homogeneous superfluid turbulence. Adapting the simulation to the 3-sphere requires some consideration, which I will discuss in Section 4.2. In Section 4.3, I discuss the characteristics of turbulence in our system when using nonlocal interaction. We find that turbulence on the 3-sphere is distinctly different from that of the periodic cube. Then, similar to Chapter 3.3, I discuss what happens to these characteristics when we reduce the nonlocal interaction distance d_{NL} so as to isolate the effect of the nonlocal interaction.

4.2 Adaptations

The 3-sphere we use is embedded in \mathbb{R}^4 . Thus, it is defined as the locus of points (x, y, z, w) such that $x^2 + y^2 + z^2 + w^2 = r_0^2$. There are several issues that have to be addressed when converting to this new geometry, not the least of which is, once the code has been fully adapted, how we can visualize our system.

Simply viewing the vortex tangle is a powerful tool for understanding what is actually happening. Humans have powerful (although somewhat biased) pattern-recognition capabilities that computers cannot fully mimic. The global structure of the 3-sphere is not something we can easily picture. But we can project the 3-sphere in different ways onto flat space to help us with this task. A few common and useful ways of doing this are the stereographic projection, hyperspherical coordinates, and the Hopf projection (or Hopf fibration). Appendix E discusses these projection methods in more detail. However for large volumes of data, finding patterns in these projections can be inefficient. So at several points in the analysis, we rely on looking for behavior in the resultant characteristics, such as the equilibrated line length density, $\langle L \rangle$, and anisotropy I_{\parallel} .

We must also rethink the applied velocity field used to sustain turbulence. The driving velocity in a periodic cube is usually uniformly in the \hat{z} direction, as it is in our implementation from Chapter 3. This obviously will not work on S^3 . A uniform velocity in \mathbb{R}^4 would drive the vortices immediately off of our S^3 surface. The relevant mathematical construct is the tangent space (or tangent bundle). We need the velocity field driving our system to lie everywhere tangent to S^3 . This is what is done in a periodic cube, too. The uniform \hat{z} velocity lies within the tangent

bundle of the periodic cube because at no spot in the cube does it have a component along some fourth, orthogonal dimension.

The appropriate velocity field to use in S^3 is called the Hopf velocity, or Hopf vector field. It is given in \mathbb{R}^4 components as: $\vec{v} = |v|(-y, x, -w, z)/r_0$. The Hopf velocity field possesses several useful properties. It is tangent to S^3 , uniform magnitude, and divergence-free. However, it is not irrotational. The curl of this field is: $\text{curl}(\vec{v}) = 2\vec{v}/r_0$, tangent to itself. This is a little disconcerting because the driving velocity is supposed to be an average velocity, and does not include contributions from the vortex filaments. The way around this is to make our driving velocity only come from the normal fluid velocity. While this is slightly restrictive, it is also handy for simulation. Since vortices move roughly with the superfluid velocity (see Appendix B.2), using the normal fluid velocity means we get less translational motion of the vortex filaments, making them easier to visualize. Appendix F discusses properties of the Hopf velocity field in more detail.

There is another significant difference between S^3 and the periodic cube: the 3-sphere has a curvature and the periodic cube does not. The fact that the 3-sphere is non-Euclidean means that the familiar expression of the Biot-Savart law, derived for 3-dimensional Euclidean space, is not completely accurate. The 3-sphere is a smooth manifold and, thus, looks locally like \mathbb{R}^3 , but the Biot-Savart law is nonlocal. We could use the S^3 Biot-Savart law, see for example DeTurck and Gluck (2004), or Kuperberg (2008), but there is a practical reason to avoid this, and simply proceed by modifying the Euclidean form. It is a closer analogue to the periodic cube. From the perspective of simulating superfluid turbulence, periodic boundaries are chosen

because they mimic the real world in a very large, periodic system. The choice benefits us with simplicity and less computation time. We wish to approach the problem from a similar perspective. Embed our superfluid system in a geometry with only the most necessary changes. Instead of a vortex leaving one wall and emerging from the opposite, like with a periodic cube, travel along a great circle for half the circumference, in any direction, and you begin to return to your original point. In effect, we wish to make this a change in the “boundary” conditions. I will start with the analogy to the 3-torus. We still define our 3-sphere as the locus of \mathbb{R}^4 points such that $x^2 + y^2 + z^2 + w^2 = r_0^2$, but we use the Euclidean Biot-Savart law up to a certain d_{NL} and require the local dynamics to behave as if the 3-sphere is flat. There are several modifications that make our vortices move in this fashion.

Distances between points on S^3 must be calculated along the geodesic between the two points, not through the 4-dimensional volume. And vectors that exist on a 3-sphere are members of the tangent space of that point. Vectors from the tangent spaces of two different points need to be parallel transported along the geodesic connecting them, before any vector operation can be performed. This is as simple as applying a rotation in \mathbb{R}^4 between the two points. Additionally, when the Runge-Kutta-Fehlberg routine iterates our vortex points, the new point has been iterated along a vector in the tangent space of the original point. So the new point is placed off of the 3-sphere. Projecting directly back onto the 3-sphere would yield a slight decrease in the distance traveled during that time step. So we scale the distance traveled so it is the same magnitude as the \mathbb{R}^4 difference vector, but now lying along the geodesic below this vector.

Since our vectors are represented in \mathbb{R}^4 , they obviously have an extra dimension to them. Dot products are easily extended to \mathbb{R}^4 , but cross products are a bit trickier. A cross product in \mathbb{R}^3 between two non-collinear vectors results in a vector perpendicular to both. Those initial two vectors span a two-plane and the resultant vector is normal to it. In \mathbb{R}^4 , a two-plane is normal to another two-plane, not a vector. Thus, the cross product requires 3 vectors. The natural choice for this third vector is the radius vector at the point on the 3-sphere where the cross product is taking place. We always want vortex motion to be within the 3-sphere surface, which is always perpendicular to the radius vector to the point in question. As in \mathbb{R}^3 the cross product can be computed with a determinant. In \mathbb{R}^3 , we can compute the cross product of two vectors \vec{v}_1 , and \vec{v}_2 with:

$$\text{cross}(\vec{v}_1, \vec{v}_2) \cdot \vec{u} = \det(\vec{v}_1, \vec{v}_2, \vec{u}),$$

where \vec{u} is the vector of unit vectors $(\hat{x}, \hat{y}, \hat{z})$. In \mathbb{R}^4 , we simply include another vector, \vec{r}_0 , the position vector to the location of the tangent vectors v_1 , and v_2 :

$$\text{cross}(\vec{v}_1, \vec{v}_2, \vec{r}_0) \cdot \vec{u} = \det(\vec{v}_1, \vec{v}_2, \vec{r}_0, \vec{u}).$$

Finally, the vortex tangent, \hat{s}' , and curvature vector, \vec{s}'' , discussed in Chapters 2.2 and Appendix C, involve these vector operations in \mathbb{R}^4 . And, thus, they can have components along the 3-sphere radius vector at their locations. The cross product does remove components along this 3-sphere radius but the dot product does not. However, we explicitly remove components along \vec{r}_0 . When calculating \vec{s}'' with

the cross product, we are automatically removing the intrinsic 3-sphere curvature. While normally the minimum curvature vector on S^3 has magnitude $1/r_0$, removing the component along \vec{r}_0 gives the radius the same allowed range as on the periodic cube. This is our adherence to a flat system.

Now, since we are in a new geometry, which requires modification of our code, it would be worthwhile to do an independent demonstration that our code produces accurate data. While we have demonstrated in Chapter 3 that we reproduce homogeneous turbulence, some modifications have been made. Our ultimate test for accuracy in the periodic cube was empirical: our simulations match previous experiment and theory. Our task is more difficult on the 3-sphere since no experiments can be done in such a geometry and, to our knowledge, no other simulations have been performed to compare to. We do know that our unmodified vortex dynamics work on the periodic cube. Our parameters have not changed significantly from the torus and added error comes from simple modifications such as projecting our vortices back onto the 3-sphere and parallel transporting between tangent spaces. It also turns out that we have qualitative agreement with the 3-sphere Biot-Savart law. However, I will discuss this further in Section 5.2, since it was only after our simulations had been performed that we realized such predictions could have been made. We shall now look at our results for simulating superfluid turbulence on S^3 .

4.3 S^3 with Nonlocal Interactions

We start out by investigating the regime with significant nonlocal interaction. I have already discussed how Adachi et al. (2010) showed this can eliminate the open-orbit problem from periodic boundaries. Figure 3.4 on page 50 showed that using the LIA artificially inflates the equilibrated $\langle L \rangle$ compared to the full Biot-Savart calculation. Figure 3.23 on page 80 showed that, for the periodic cube, there is relatively little sacrifice in accuracy from reducing the nonlocal interaction distance, d_{NL} , down to some critical value on order of $\langle \ell \rangle$. For the 3-sphere, we use $d_{NL} = 0.5\pi r_0$ as our maximum interaction interaction distance. This is the arclength along the 3-sphere, meaning that a point on the vortex experiences the nonlocal velocity field from vortices within the nearest half of the 3-sphere.

4.3.1 Homogeneity

Similar to Chapter 3.2.2, we start with the most direct test of homogeneity. We can easily split our 3-sphere volume, embedded in \mathbb{R}^4 , into its 16, Euclidean orthants (the n -dimensional name for an octant). Figure 4.1 shows the evolution of $L(t)$ within each orthant for some example driving velocities, v_{ns} .

The two graphs in Figure 4.1 (a) and (d) do appear homogeneous, similar to those for the 3-torus, in Figure 3.6 on page 53. But (b) and (c) do not. We want any deviations between the orthants to be relatively short-lived and these two velocities lead to some orthants with long-term differences in their L , over time. This inhomogeneity reveals itself more clearly by looking at each orthant's equilibrated $\langle L \rangle$.

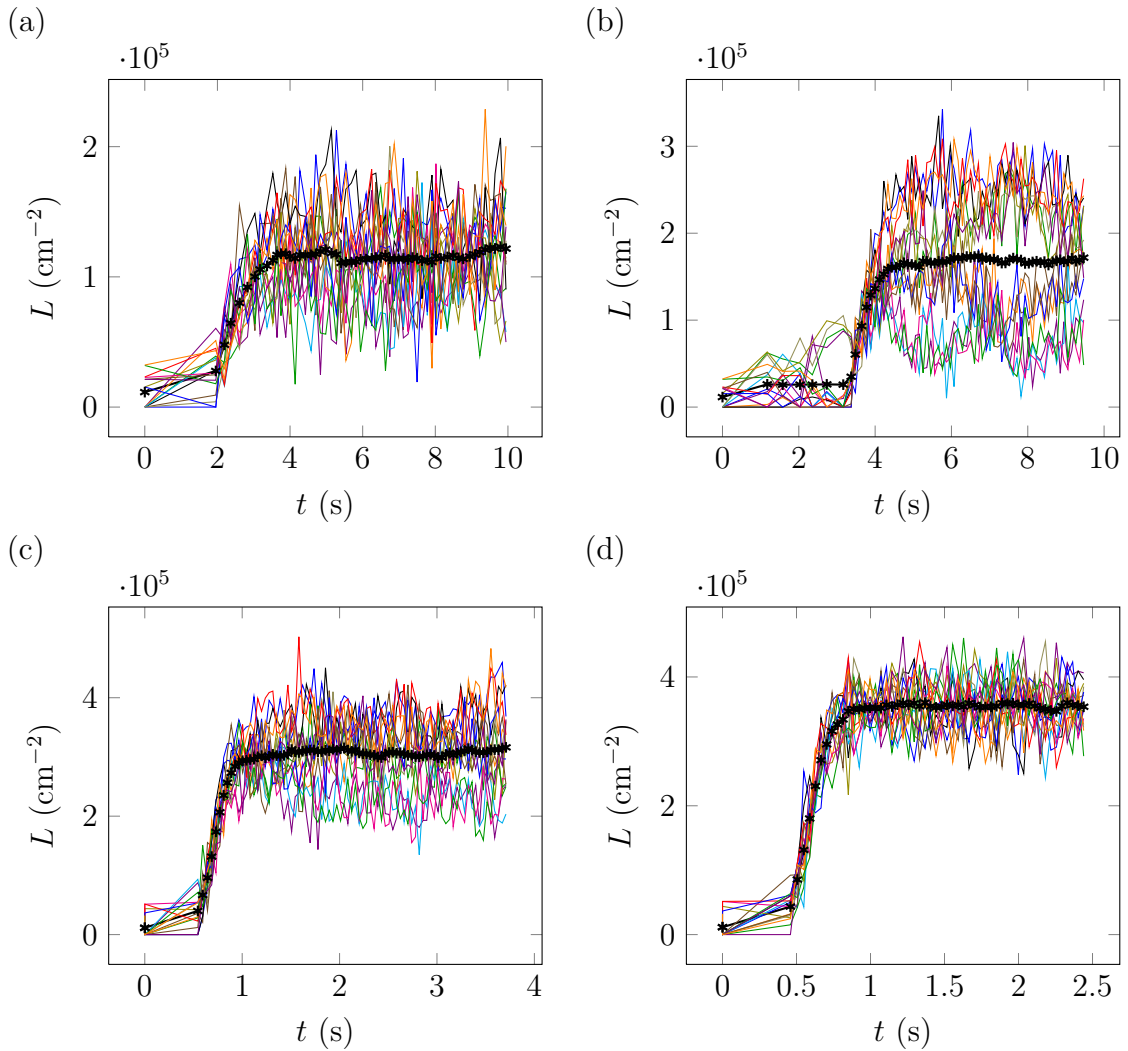


Figure 4.1: Evolution of $L(t)$ for each of the 16 \mathbb{R}^4 orthants of our 3-sphere. Each curve in (a) and (b) gives the $L(t)$ of one orthant. The 3-sphere radius, $r_0 = 0.005$ cm and the driving velocity is (a) $v_{ns} = 1.0$ cm/s, (b) $v_{ns} = 1.2$ cm/s, (c) $v_{ns} = 1.8$ cm/s, and (d) $v_{ns} = 2.0$ cm/s. The curves, ---*--- , show $L(t)$ using the total system volume. The erratic features near $t = 0$ are due to fewer files being saved per unit time interval.

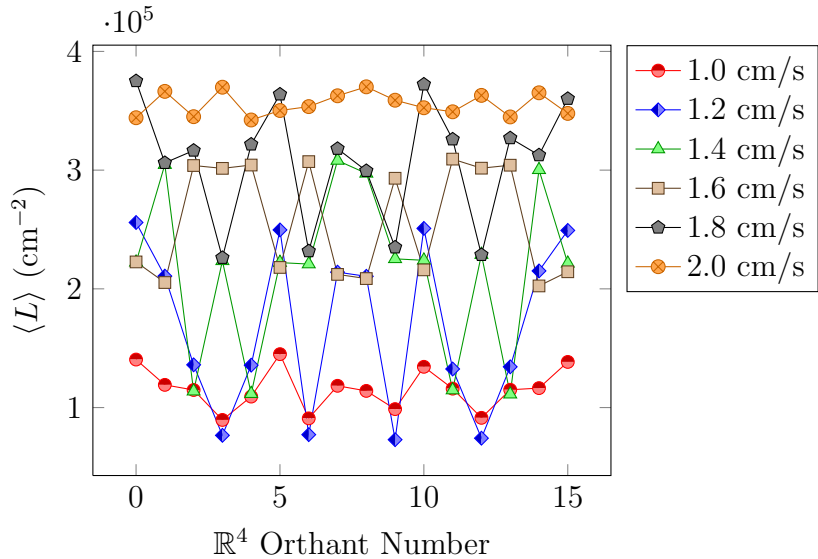


Figure 4.2: Average equilibrated line length density, $\langle L \rangle$, within each \mathbb{R}^4 orthant of the 3-sphere, with radius $r_0 = 0.005$ cm, at multiple velocities.

These averages are displayed in Figure 4.2.

The inhomogeneity in the 3-sphere turbulence is even more striking from Figure 4.2. It is unusual that the system, at low velocity, starts out relatively homogeneous and eventually returns to a similar state. But there is a deeper apparent structure within Figure 4.2. The line length densities in orthants 0 through 7 are approximately mirrored in 8 through 15. I plot just a few of these velocity curves in Figure 4.3.

The numbering scheme for these orthants is such that each of the four coordinates is assigned one bit. The negative coordinate gets a bit value of 0, and positive gets a 1. Then the orthants are numbered in binary such that, x is in the 2^0 position, and

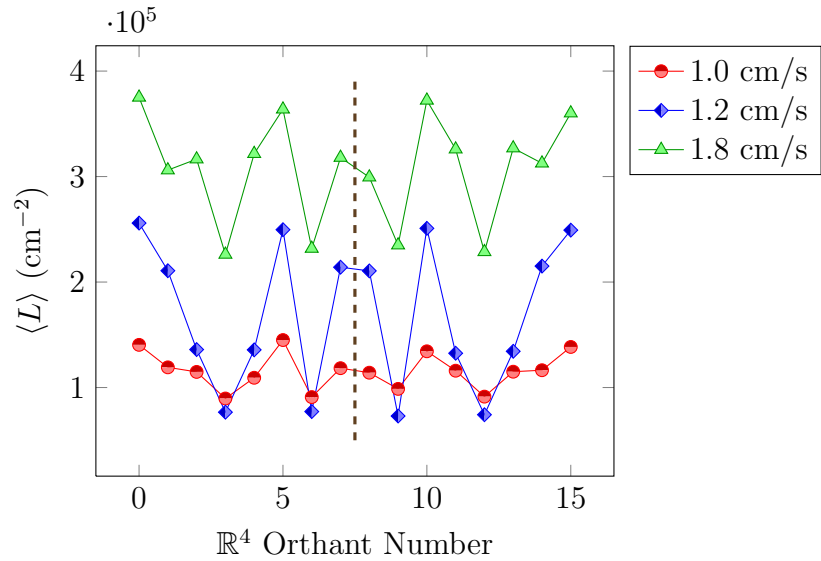


Figure 4.3: Average equilibrated line length density, $\langle L \rangle$, within each \mathbb{R}^4 , orthant of the 3-sphere, showing approximate mirror symmetry between orthants on each side of the vertical line. The curves are example velocities taken from Figure 4.2.

Orthant	Binary # Inversion	Orthant
0	0000 \leftrightarrow 1111	15
1	0001 \leftrightarrow 1110	14
2	0010 \leftrightarrow 1101	13
3	0011 \leftrightarrow 1100	12
4	0100 \leftrightarrow 1011	11
5	0101 \leftrightarrow 1010	10
6	0110 \leftrightarrow 1001	9
7	0111 \leftrightarrow 1000	8

Table 4.1: Demonstration that a mirror symmetry in the $\langle L \rangle$ for each \mathbb{R}^4 orthant equates to an inversion symmetry in the vortex tangle from trials in Figure 4.2.

w is in the 2^3 position. So, for example, $(x \geq 0, y < 0, z < 0, w < 0)$ is orthant 1 and $(x \geq 0, y \leq 0, z \geq 0, w \geq 0)$ is orthant 13. If $d_x = \{0, 1\}$ is the x digit, the binary number should be read $d_w d_z d_y d_x$. With this knowledge it is clear that the mirror symmetry in the orthant number equates to inversion symmetry in \mathbb{R}^4 , as shown in Table 4.1.

It would be a remarkable coincidence if the $\langle L \rangle$ for orthants inverted through the origin from each other were the same without the same vortices actually passing through both orthants. This suggests that vortices lie approximately on great circles since a great circle passing through one point will pass through that point's antipode.

There is a deeper symmetry to this system. For example, from $v_{ns} = 1$ cm/s, orthants 0, 5, 10, and 15 all have about the same $\langle L \rangle$. As do orthants 3, 6, 9, and 12. We can hypothesize that the symmetry is the same as the Hopf vector field: $(-y, x, -w, z)$. This vector field points along particular great circles of the 3-sphere

called Hopf fibers. I shall refer to the particular rotations from this Hopf vector field acting on a point (x, y, z, w) as Hopf symmetry. Under this symmetry, $x \mapsto -y$, $y \mapsto x$, $z \mapsto -w$, and $w \mapsto z$. Taking the orthants 0, 5, 10, and 15, and applying the Hopf symmetry (and remembering $d_w d_z d_y d_x$):

$$(0, 5, 15, 10) : 0000 \mapsto 0101 \mapsto 1111 \mapsto 1010 \mapsto 0000$$

These orthants, possessing similar $\langle L \rangle$ values, follow the Hopf symmetry. This helps explain the other orthants, too.

$$(1, 7, 14, 8) : 0001 \mapsto 0111 \mapsto 1110 \mapsto 1000 \mapsto 0001$$

$$(2, 4, 13, 11) : 0010 \mapsto 0100 \mapsto 1101 \mapsto 1011 \mapsto 0010$$

$$(3, 6, 12, 9) : 0011 \mapsto 0110 \mapsto 1100 \mapsto 1001 \mapsto 0011$$

There are two other Hopf vector fields that are perpendicular to our chosen Hopf velocity: $(z, -w, -x, y)$, and $(-w, -z, y, x)$. These, however, do not explain the symmetry displayed in Figures 4.2 and 4.3. For example, $(z, -w, -x, y)$ gives us a map:

$$(0, 6, 15, 9) : 0000 \mapsto 0110 \mapsto 1111 \mapsto 1001 \mapsto 0000.$$

This still has inversion symmetry because this vector field still lies along great circles on S^3 and every point shares a great circle with its antipode. But these are not the same great circles that pass through orthants of the same $\langle L \rangle$ value, from Figure 4.2.

The symmetry of our Hopf velocity field is that. Note that while $(z, -w, -x, y)$, and $(-w, -z, y, x)$ are also called Hopf vector fields and the great circles they follow are Hopf fibers, I refer specifically to those associated with our driving velocity, $(-y, x, -w, z)$.

This analysis suggests that the vortex tangle preferentially aligns with Hopf fibers of S^3 (at least to a significant degree). But we can look at the anisotropy measure I_{\parallel} (Equation 3.3 from Chapter 3.1) for a more quantitative look at the structure of the turbulence on the 3-sphere. Before we leave this topic, however, notice that there is one last structure visible in Figure 4.3. In addition to having the orthant $\langle L \rangle$ follow Hopf symmetry, the particular values for $\langle L \rangle$ that these orthants take have a structure to them. The $\langle L \rangle$ value varies between orthants in a similar way for different velocities. This suggests that there may be an asymmetry among which great circles on the 3-sphere are occupied more by vortices than others. To discern this secondary structure, we need to remove the primary Hopf symmetry. We can do this with use of the Hopf projection.

Hopf Projection

The Hopf projection is a map from S^3 with radius r_0 , to S^2 with radius r_0^2 (see Appendix E). Every point on the codomain, S^2 , is the image point of a great circle on, S^3 . And since flow lines from the Hopf velocity lie along great circles of S^3 , how close a vortex is to being condensed to a single point gives a visual indication of how closely the vortex lies along the same great circle. Appendix E also contains a comparison of Hopf fibers of the 3-sphere under the Hopf projection versus a

stereographic projection, in Figure E.6 on page 190. The Hopf projection allows us to see which great circles on the 3-sphere are occupied by at least one vortex point. Furthermore, if the Hopf projection of a vortex lies very nearly on one point on S^2 , then it lies very nearly along one great circle on S^3 . Snapshots of the vortex tangle from the trials in Figure 4.1 are displayed under the Hopf projection in Figure 4.4.

Our \mathbb{R}^4 homogeneity data showed there is some tendency for vortices to align with the Hopf fibers of S^3 , but not how strong this tendency is. Figure 4.4 gives us more information. If vortices were aligned perfectly, we would expect these Hopf projections of the vortex tangle to look like single points. But this is not what we see. There must still be some alignment or our \mathbb{R}^4 homogeneity data would not show the Hopf symmetry. So a vortex segment aligns partially with a local Hopf velocity at its location, but its deviation causes the following vortex segment to lie away from the great circle of the previous segment. And now this new vortex segment aligns partially with this new local velocity. To what degree these vortices align is answerable by the anisotropy parameter data, I_{\parallel} , which is discussed in Section 4.3.2.

Looking at (a) of this figure, it appears that a large section of the the projected S^2 is unoccupied. But note that the tangles displayed in Figure 4.4 are simply snapshots. Figure 4.2 gave us the first clue of an underlying Hopf symmetry to how the vortex tangle was aligning. One benefit of using the Hopf projection is that it gives us another way to analyze the structure of our vortices. Instead of plotting the $L(t)$ for the 16 \mathbb{R}^4 orthants, we can look at the 8 \mathbb{R}^3 octants of our Hopf-projected system of vortices. That is, we count the line length density in the octants formed when the projected coordinates (h_1, h_2, h_3) are each either less than or greater than 0. Viewing

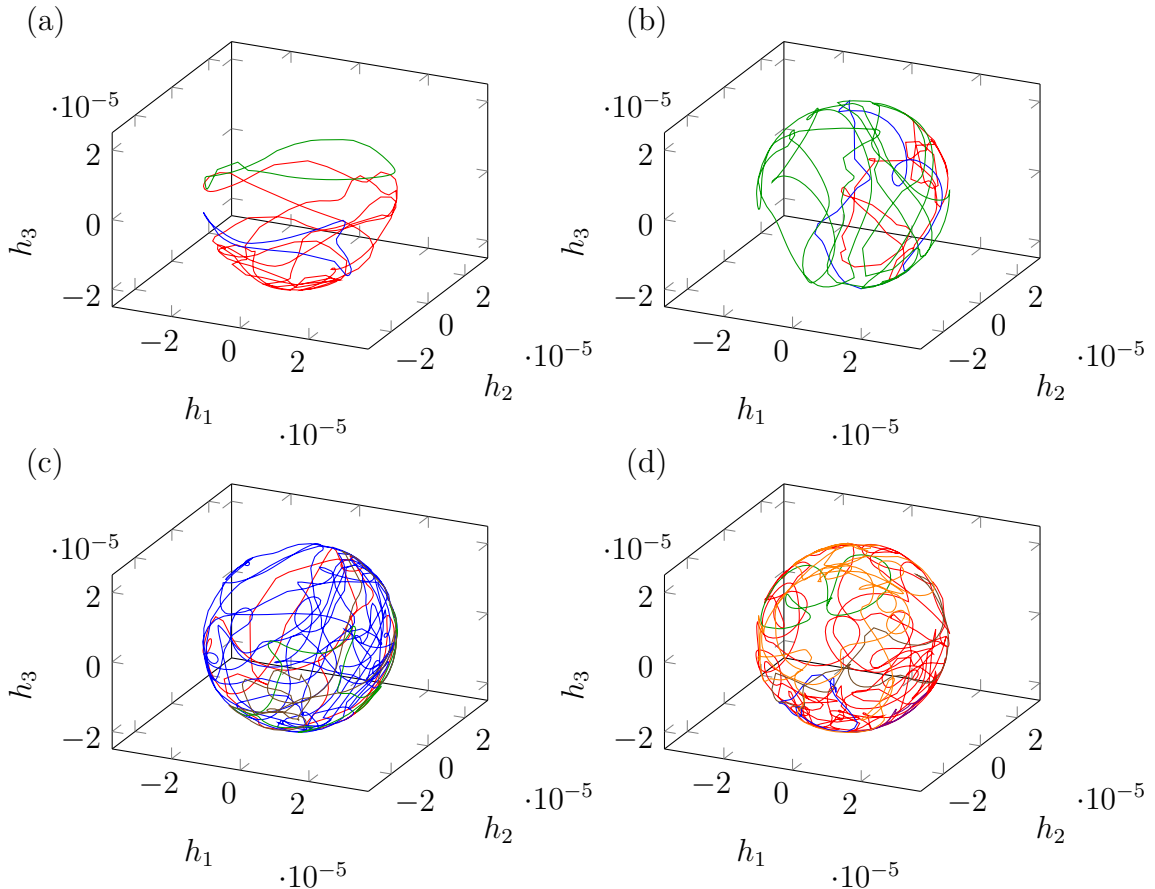


Figure 4.4: Hopf projections of snapshots of the vortex tangles, after equilibration, for trials from Figure 4.1: (a) $v_{ns} = 1.0 \text{ cm/s}$, (b) $v_{ns} = 1.2 \text{ cm/s}$, (c) $v_{ns} = 1.8 \text{ cm/s}$, (d) $v_{ns} = 2.0 \text{ cm/s}$.

this homogeneity data removes the Hopf symmetry we saw in Figure 4.2 and allows secondary structures to appear in greater relief. Perhaps vortices preferentially align along particular Hopf fibers. First, we shall look at the time evolution of $L(t)$ within each Hopf octant, shown in Figure 4.5.

Comparing this Hopf-projected $L(t)$ data to the \mathbb{R}^4 , $L(t)$ data of Figure 4.1 on page 100, the inhomogeneity is even more distinct under this projection. Also note that, although in every trial in Figure 4.1 the total $L(t)$ seems to have fully equilibrated, the same trials under the Hopf projection seem to have more variation in time. We can look at the time averages of all of these Hopf-projected $L(t)$ trials in Figure 4.6.

It is not until near $v_{ns} = 2.0$ cm/s that the system becomes approximately homogeneous, which is distinct from the periodic cube where even the lowest sustainable velocities were homogeneous. Figure 4.6 does seem to contain a couple of subtle structures, but neither are completely consistent across different v_{ns} curves. The 1, 1.2, and 1.8 cm/s curves show staggering, where the odd-numbered Hopf octants have a larger $\langle L \rangle$ value than their neighboring even-numbered octants. This does not hold well for the other velocities, however. For example, the trend reverses itself for 2.0 cm/s, after octant 3. The numbering scheme for the octants is similar to Figure 4.2, where binary numbers are assigned such that $h_i < 0 \rightarrow d_{h_i} = 0$ and $h_i \geq 0 \rightarrow d_{h_i} = 1$. The binary number should be read, $d_{h_3}d_{h_2}d_{h_1}$. If one labels the octants this way, odd-numbered octants having greater $\langle L \rangle$ means the $+h_1$ octants are more densely occupied. The fact that this trend reverses after octant 3 for the 2.0 cm/s curve indicates that when h_3 is negative, the $+h_1$ octants are more densely

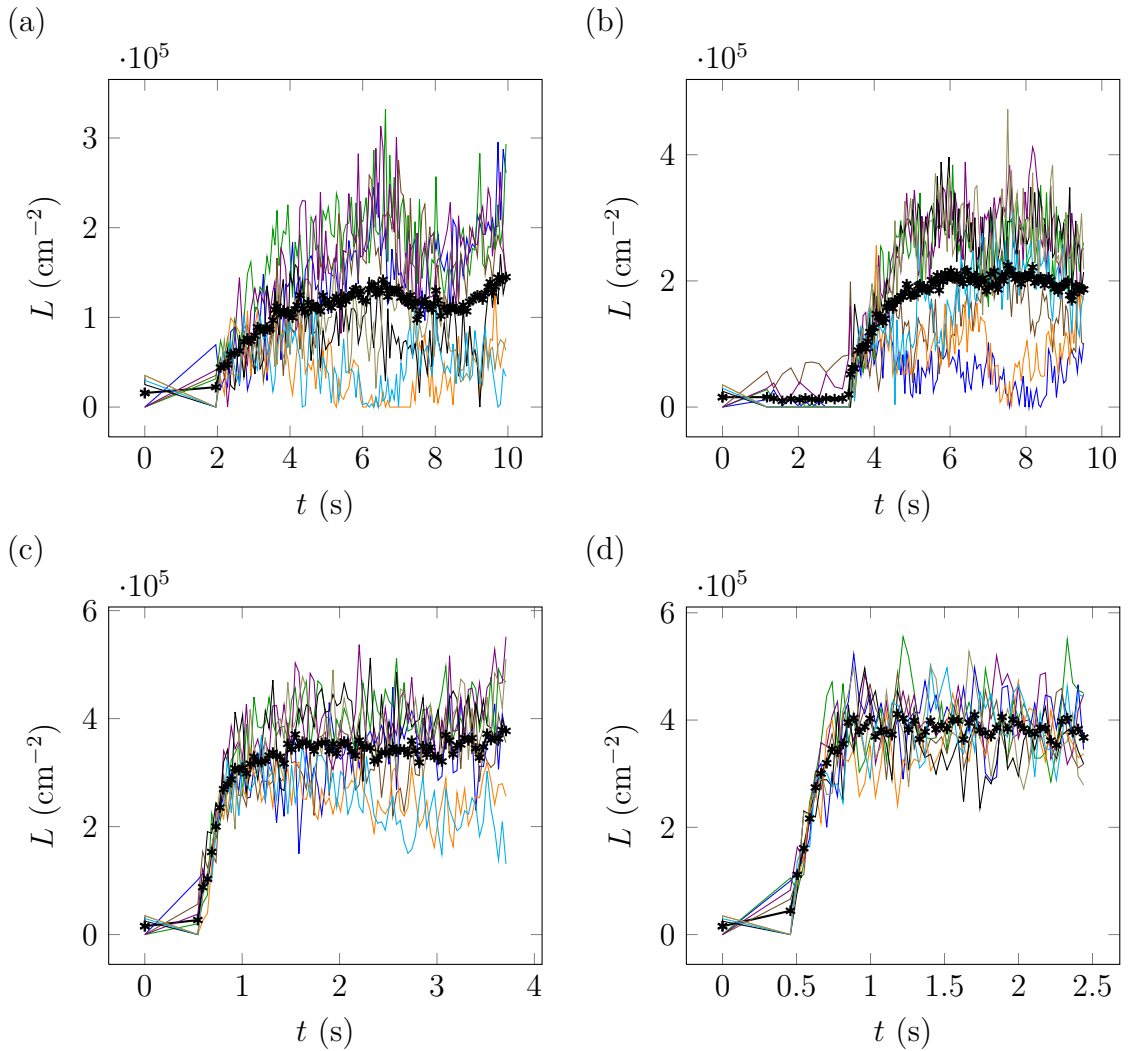


Figure 4.5: Evolution of $L(t)$ for each of the 8, \mathbb{R}^3 octants of the Hopf-projected image of our 3-sphere. These are the same trials shown in Figure 4.1 on page 91. Each curve in (a) and (b) gives the $L(t)$ of one octant. The driving velocity in each figure is (a) $v_{ns} = 1.0 \text{ cm/s}$, (b) $v_{ns} = 1.2 \text{ cm/s}$, (c) $v_{ns} = 1.8 \text{ cm/s}$, and (d) $v_{ns} = 2.0 \text{ cm/s}$. The curves, ---*--- , show $L(t)$ using the total surface area of the Hopf-projected 2-sphere, $4\pi(r_0^2)^2$.

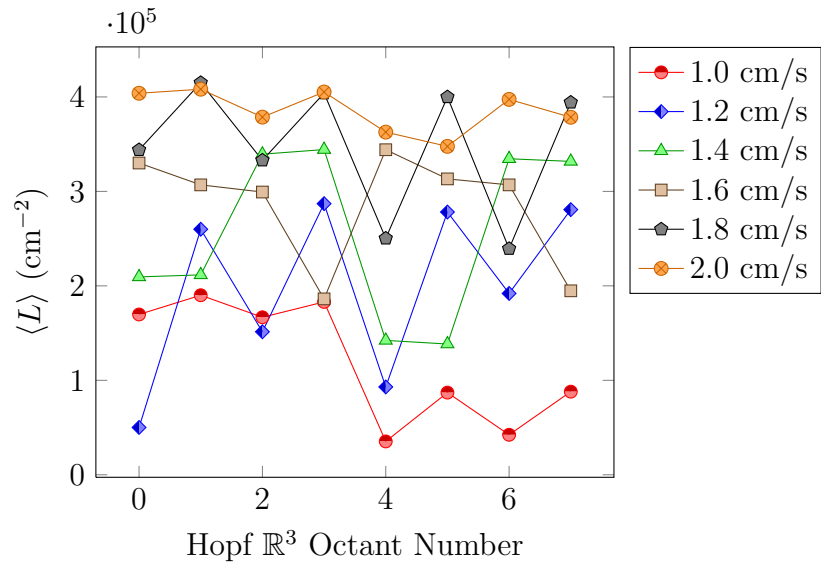


Figure 4.6: Average equilibrated line length density, $\langle L \rangle$, within each Hopf-projected octant, with radius $r_0 = 0.005$ cm, at multiple velocities. Compare to the unprojected Figure 4.2 on page 92. A similar octant numbering scheme is used, where binary numbers are assigned such that $h_i < 0 \rightarrow d_{h_i} = 0$ and $h_i \geq 0 \rightarrow d_{h_i} = 1$. The binary number should be read, $d_{h_3}d_{h_2}d_{h_1}$.

Octant	Binary # Inversion	Octant
0	$000 \leftrightarrow 111$	7
1	$001 \leftrightarrow 110$	6
2	$010 \leftrightarrow 101$	5
3	$011 \leftrightarrow 100$	4

Table 4.2: Demonstration that a mirror antisymmetry in the Hopf-projected octant number equates to an inversion antisymmetry in the vortex tangle from trials in Figure 4.6.

occupied, and for $+h_3$, the $-h_1$ octants are more densely occupied.

The other structure, which is a bit more consistent, is an approximate mirror antisymmetry in the Hopf octant $\langle L \rangle$ values. This mirror antisymmetry is equivalent to an inversion antisymmetry in \mathbb{R}^3 , as shown in Table 4.2. Figure 4.7 shows a few curves from Figure 4.6 isolated to help show this mirror antisymmetry.

If the $\langle L \rangle$ data for each octant number on one side of the vertical line is reflected about their average value and about the vertical line, it matches approximately with data on the other side. It is interesting that, even though the 1 cm/s trial has such a distinct disparity, its \mathbb{R}^4 orthant structure, from Figure 4.2, was fairly homogeneous. This is likely due to the fact that dissecting the system into orthants splits the data into fairly large bins. Note that other velocities, such as the 1.6 cm/s curve from Figure 4.6, do not appear to obey this symmetry well.

It is a bit tricky to interpret this inversion antisymmetry in the Hopf \mathbb{R}^3 octants. It could mean the vortex tangle is shifted from one region of the Hopf S^2 to the antipode. This needs to persist for a long enough time that it shows up in the

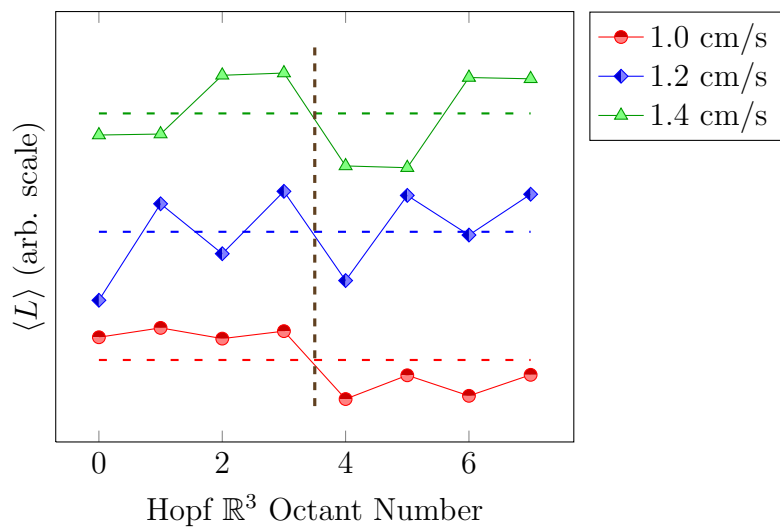


Figure 4.7: Select velocity curves from Figure 4.6 showing mirror antisymmetry in $\langle L \rangle$ within each Hopf-projected octant. Average lines are displayed for each velocity curve. The curves are shifted vertically to separate them for easier viewing.

average. Since this is a projection from great circles to points, an increase in line length could come from vortices on \mathbb{R}^4 diverging from the Hopf fibers they lie along, and thus expanding away from a point on the projected S^2 . This would increase the $\langle L \rangle$ in one region of the projected S^2 . This inversion antisymmetry would then equate to vortices aligning with particular great circles found on one region of the projected S^2 while other vortices simultaneously diverge from their great circles which project to the opposite side of the 2-sphere. With such large disparities in some of the $\langle L \rangle$ values between the pairs of antipodal octants, this seems unlikely. Such synchronous behavior would require an interaction to synchronize it, and our nonlocal interaction only reaches to half the S^3 . The fact that each point is really a great circle and the S^2 we are viewing actually has an extra dimension makes this explanation difficult to assess from this data alone.

Actually watching the Hopf projected vortex tangle evolve (for which Figure 4.4 on page 98 gave snapshots), the vortices do not shift back and forth dynamically between opposite ends of this S^2 after they have equilibrated. Nor is the reduced line length in a region of the projected 2-sphere due to vortices being better aligned with these corresponding great circles, thus condensing to points. Instead the vortices at this lowest velocity tend to coalesce on one side of the S^2 space and are lacking from the opposite side. The snapshot in Figure 4.4 (a) is fairly representative of the tangle as it moves in time. Something must be selecting this region of the projected S^2 , these particular Hopf fibers of S^3 . If this is the case, the initial conditions seem a likely explanation but the alternative may simply be that the system has not had enough time to fluctuate significantly. The large variation in octant $L(t)$ during our

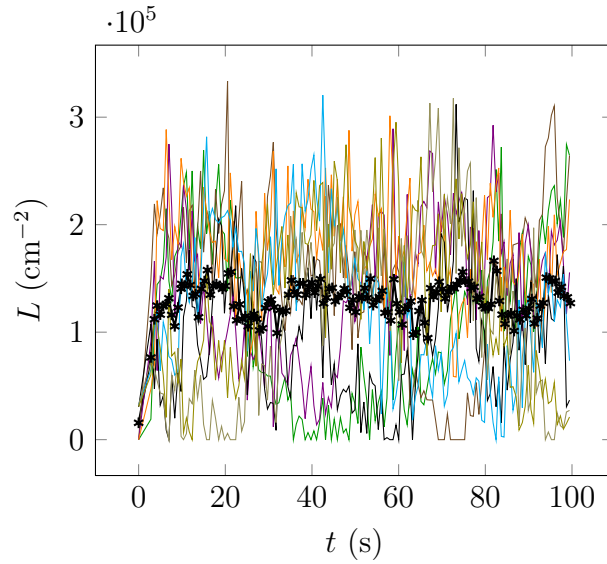


Figure 4.8: Extended $L(t)$ data for each of the 8, \mathbb{R}^3 octants of the Hopf-projected image of Figure 4.5 (a), which uses $v_{ns} = 1.0$ cm/s. The curve, ---*--- , shows $L(t)$ using the total surface area of the Hopf-projected 2-sphere, $4\pi(r_0^2)^2$.

time domain included in Figure 4.5 leads us to consider the latter. Perhaps if we extend beyond this range, the particular disparity in octant $\langle L \rangle$ values will shift. It may even be that the system will become homogeneous. Let us extend the data in Figure 4.5 (a) by 10-fold, shown in Figure 4.8.

For clarity, Figure 4.9 separates the $L(t)$ for each octant over several axes so we can look for any periodic nature to the line length density in this projection.

The per-octant $L(t)$ does not seem to settle down. It still deviates significantly from the total, Hopf-projected $L(t)$. So the system never does reach homogeneity. To further explore the change in structure, we shall look at the average octant $\langle L \rangle$

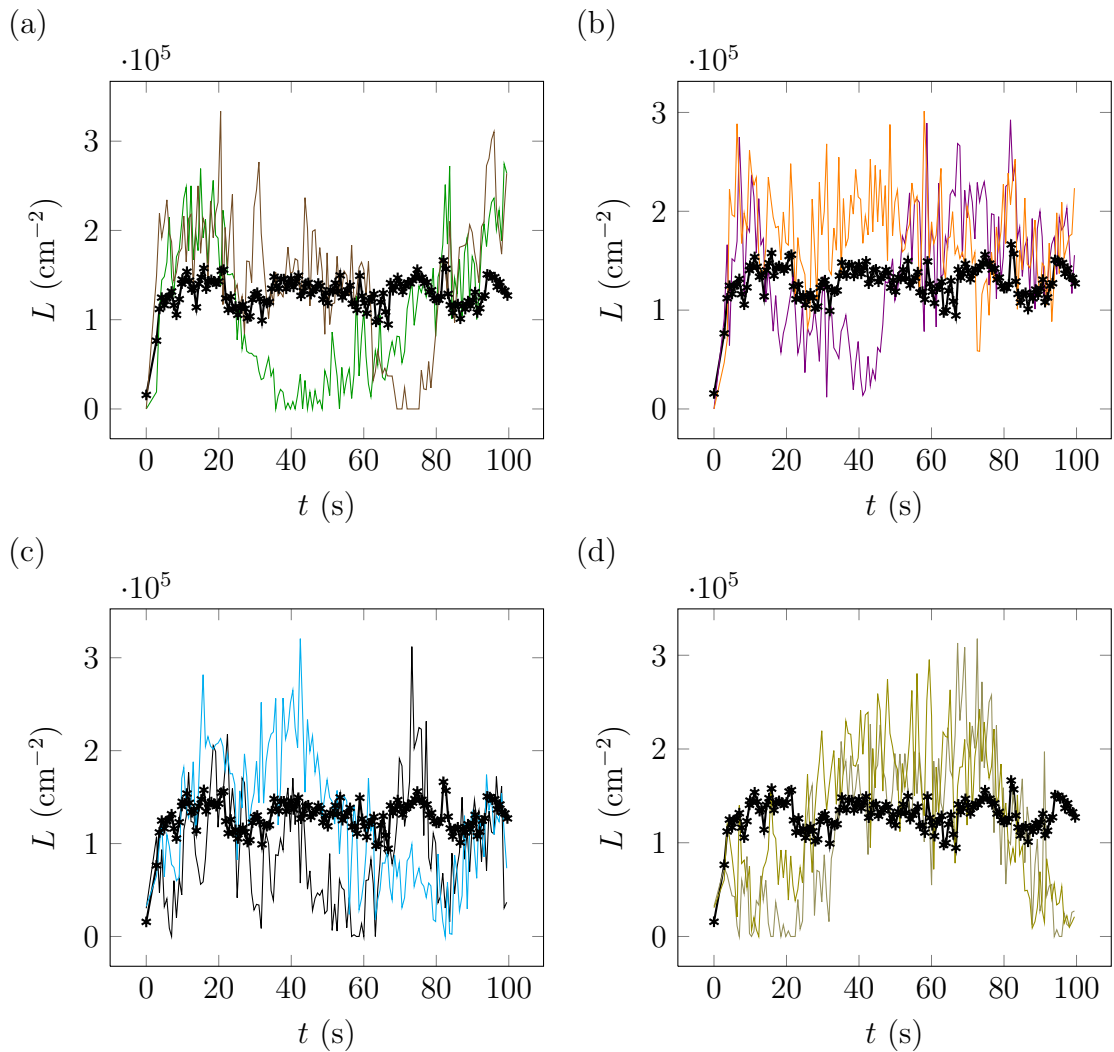


Figure 4.9: The same data from Figure 4.8, but separating the $L(t)$ octant data between different graphs. Part (a) contains octants 0 and 1, part (b) contains octants 2 and 3, et cetera.

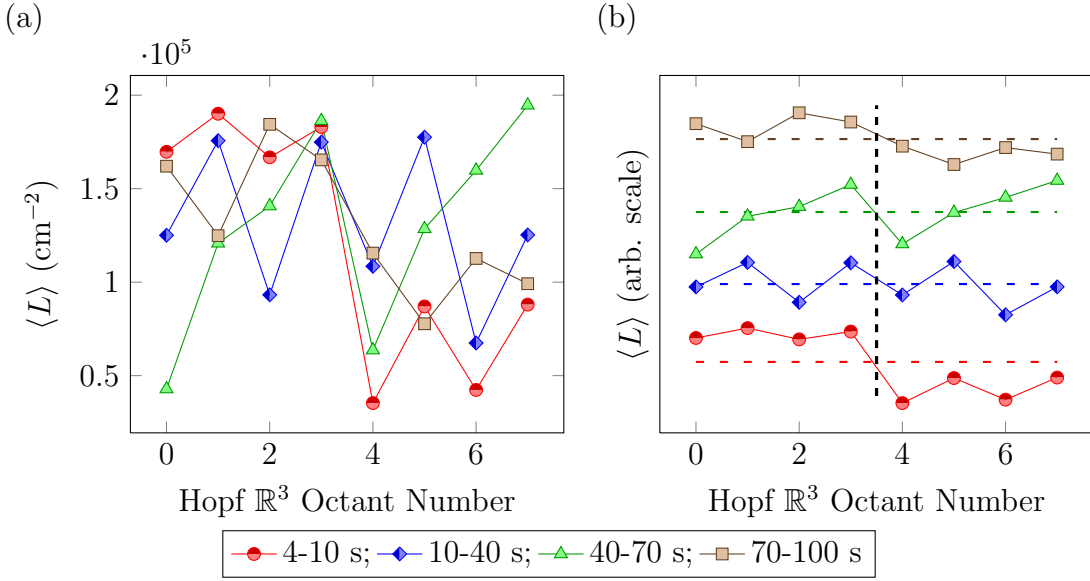


Figure 4.10: Average equilibrated line length density, $\langle L \rangle$, within each Hopf-projected octant, with $v_{ns} = 1.0$ cm/s. Both (a) and (b) compare the initial equilibrated fit domain (4-10 s) to that of the extended simulation (10-100 s). (b) includes a vertical shift for clarity. The averages and mirror reflection line demonstrate inversion antisymmetry in the Hopf-projected \mathbb{R}^3 , for all fit domains.

for different regions of the equilibrated data, 4-100 seconds, displayed in Figure 4.10.

The different fit domains for averaging show that the particular structure changes over time. The first region, up to 10 seconds, showed that the $+h_3$ half of the projected 2-sphere was less dense than the $-h_3$ half. But over the next 30 seconds, this is no longer true. The vortex tangle has distributed more uniformly over the projected 2-sphere, that is, over the different Hopf fibers of the 3-sphere. In the

following 30 seconds we see another shift, and finally another for the last 30 seconds. The tangle is slowly shifting between different regions of the 3-sphere. But with every time domain, the system obeys the inversion antisymmetry (shown in Figure 4.10 (b)) that we saw with other velocities in Figure 4.7 on page 103. So the vortex does not fully occupy the 3-sphere at this velocity. It stays condensed more toward one subset of great circles, and away from another. But the occupied region of the 3-sphere shifts in time. But, this inversion antisymmetry is approximate, and not noticeable at higher velocities, as the total line length increases and more of the 3-sphere is occupied.

4.3.2 Anisotropy and Line Length Density

We have established that superfluid turbulence on the 3-sphere is not homogeneous for the velocity regime in question. Rather, there is a definite Hopf symmetry to the vortices suggesting they lie preferentially tangent to the Hopf velocity. Again, this is in contrast with that of the periodic cube from Chapter 3, which has a very slight anisotropy in the opposite direction. Vortices there lie preferentially in planes perpendicular to the driving velocity. We also know this alignment in the 3-sphere is not perfect, since our vortices would appear as points under the Hopf projection. We shall now look at the effect of this new geometry on the anisotropy parameter, I_{\parallel} (from Equation 3.3), for a more quantitative difference between the 3-sphere and periodic cube. Figure 4.11 shows a comparison of these systems.

There is a dramatic difference between the two geometries. Recall that $I_{\parallel} = 2/3$ indicates the vortices are completely isotropic, and $I_{\parallel} = 0$ means the vortices lie

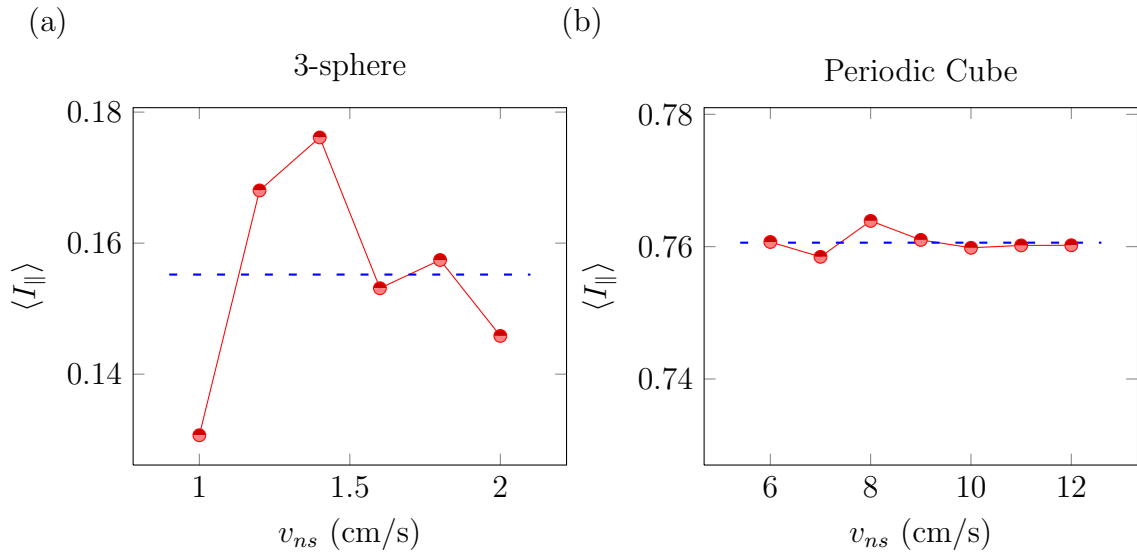


Figure 4.11: The anisotropy parameter $\langle I_{\parallel} \rangle$, for (a) the S^3 simulations found in Figure 4.13, and (b) the fully nonlocal periodic cube simulations from Figure 3.9. The dashed lines give averages of these values and are inserted for guides to the eye.

perfectly tangent to the velocity field. The periodic cube had anisotropy parameter $I_{\parallel} = 0.76$. So, vortices in the 3-torus tended to lie slightly less along the velocity field than would a completely isotropic system, so more in the planes perpendicular to this driving velocity. The 3-sphere has an average, $I_{\parallel} = 0.155$, which means a vortex that deviates only slightly from the driving velocity, about 5-10%. The I_{\parallel} of the periodic cube is also more consistent than on the 3-sphere, although there is no consistent trend with velocity in this data. We already know from our analysis of the Hopf projections in Figure 4.4 that this deviation is enough to drive a vortex away from a particular great circle. Vortices do not remain approximately fixed to one great circles, but can explore the space enough to interact.

We can investigate exactly how much these vortices interact. In Figure 3.16 on page 68, we presented data on the predicted relation between vortex reconnection rate and line length density. For isotropic homogeneous turbulence the reconnection rate takes the form, $\dot{N} \propto \langle L \rangle^{5/2}$ (Tsubota et al., 2000, Barenghi and Samuels, 2004, Nemirovskii, 2006). The analog of this figure for the 3-sphere is shown in Figure 4.12. Figure 4.12 (a) shows the number of reconnections with time for trials with a range of velocities.

Figure 4.12 (a) tells us the vortices still interact. However, our value for the exponent is now 1.63. A reduced exponent is expected with polarized turbulence due to fewer interactions compared with an isotropic tangle. This reduced value is consistent with predictions and simulations for polarized turbulence (Barenghi and Samuels, 2004, Tsubota et al., 2004).

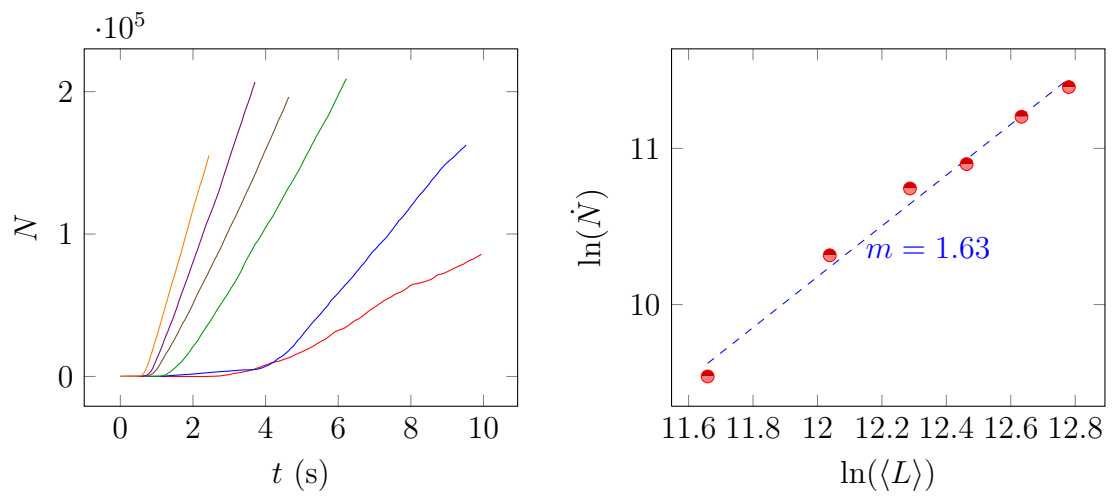


Figure 4.12: Part (a) shows the number of reconnections, N , with time for a series of trials with different velocities. Part (b) shows a plot of $\ln(\dot{N})$ versus $\ln(\langle L \rangle)$, finding the exponent of $\dot{N} = dN/dt \propto \langle L \rangle^m$, $m = 1.63$.

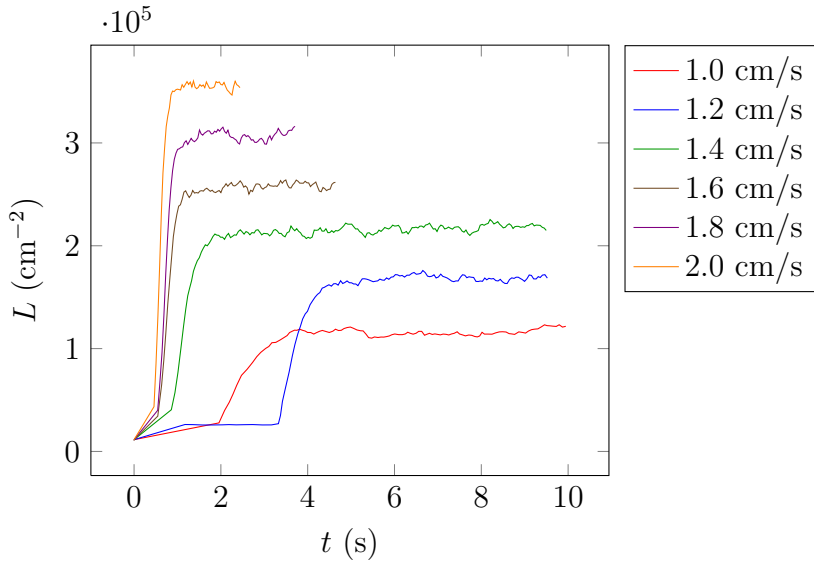


Figure 4.13: Evolution of 3-sphere line length density, $L(t)$. These simulations use the parameters, $r_0 = 0.005$ cm, nonlocal interaction distance is $\pi r_0/2$.

Line Length Density

Figure 4.13 shows the evolution of $L(t)$ for a series of 3-sphere velocities. One can already see that, with a factor of two increase in velocity between the lowest and the highest values, there is only about a factor of three increase in equilibrated $\langle L \rangle$. The scaling argument in Swanson and Donnelly (1985) and Schwarz (1988) showed that $\beta\langle L \rangle^{1/2}$ is proportional to v_{ns} . Scaling with β to remove the intercept often used for fitting this quantity, $\langle L \rangle^{1/2} = \gamma(v - v_0)$, such as in Tough (1982, ch. 3). Figure 4.14 (a) shows the $\beta\langle L \rangle^{1/2}(v_{ns})$ data for 3-sphere turbulence.

The intercept in Figure 4.14 (a) is clearly nonzero, indicating the data does not follow the predicted relation. In addition, there is concave downward trend in the

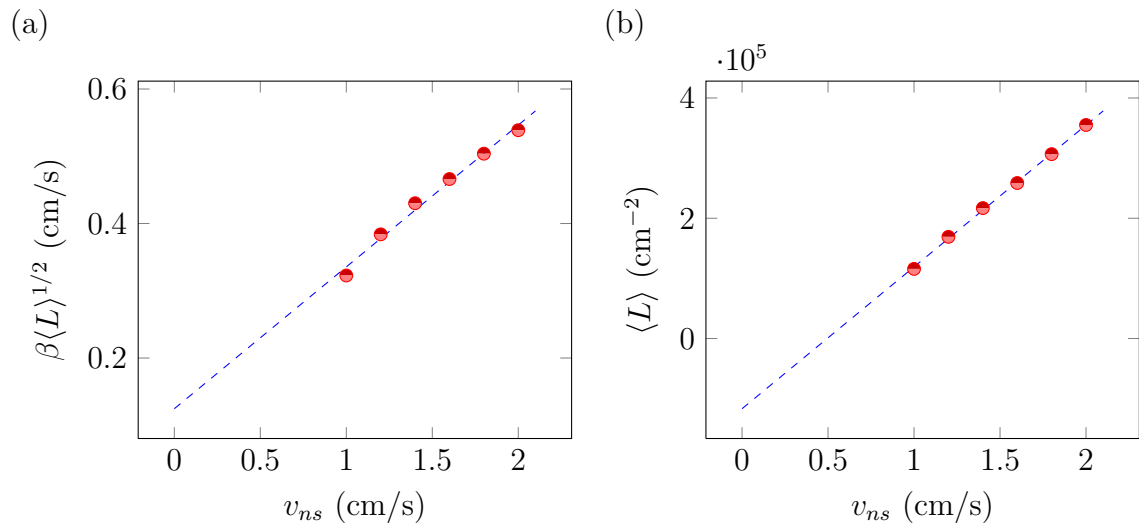


Figure 4.14: Part (a) shows a fit of $\beta \langle L \rangle^{1/2}(v_{ns})$, using averages of equilibrated data in Figure 4.13. For comparison sake, part (b) shows a fit of the same data in the linear relation $\langle L \rangle(v_{ns})$.

data that we should not overlook. Fitting the linear relation $\langle L \rangle(v_{ns})$ seems more appropriate, which is shown in Figure 4.14 (b). The fact that turbulence on the 3-sphere does not conform to conventional homogeneous turbulent relations is no surprise. We already know the system is not homogeneous. And only homogeneous turbulence is marked by this quadratic dependence of $\langle L \rangle$ on v_{ns} .

However, we saw in Figure 4.2 on page 92 and Figure 4.6 on page 101 that the $v_n = 2.0$ cm/s trial is fairly homogeneous. Do we regain homogeneous behavior above this value? And if so, do we also regain the $\langle L \rangle \propto v^2$ behavior, indicative of homogeneous turbulence in other geometries? We have extended the range of driving velocities and Figure 4.15 shows the per-orthant $\langle L \rangle$ data for this extended velocity range using (a) the 16 \mathbb{R}^4 orthants and (b) using the Hopf-projected octants.

This figure shows that, above 2 cm/s, S^3 turbulence does, indeed, remain homogeneous. Now we can see if the characteristic $\langle L \rangle(v_{ns})$ behavior is similar to Euclidean space. Figure 4.16 shows a nonlinear fit of this homogeneous turbulence $\langle L \rangle$ data in this extended v_{ns} domain.

The nonlinear fit in Figure 4.16 yields an exponent of 1.17, far below the $\langle L \rangle \propto v^2$ dependence in conventional homogeneous turbulence. These data can be explained from the scaling argument used to obtain $\langle L \rangle \propto v^2$ omitting dependence on anisotropy, which we also mention in Appendix D. Schwarz himself recognized in Schwarz (1988, p. 2403) that anisotropy affects this approximate scaling relation. In fact, an exponent x less than 2, $\langle L \rangle \propto v^x$, makes sense. Vortices on the 3-sphere predominantly align with the driving velocity. If we imagine perfect alignment with the driving velocity, our vortex equation of motion, Equation 1.9, gives zero contribution to

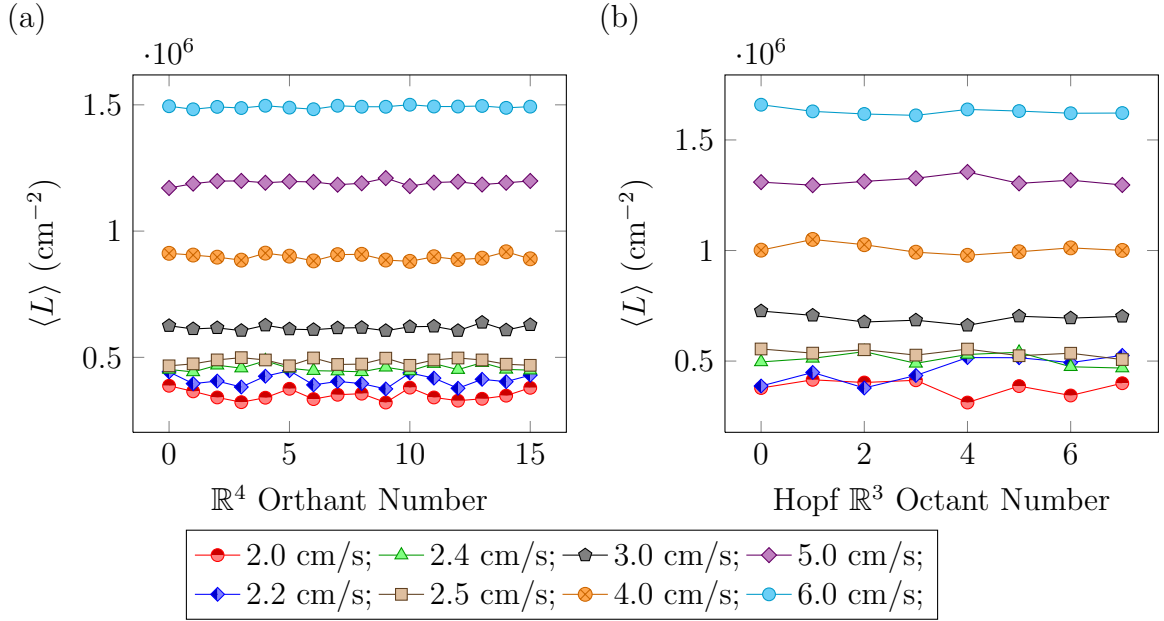


Figure 4.15: The per-orthant $\langle L \rangle$ data for $v_{ns} : [2, 6] \text{ cm/s}$ using (a) the 16 \mathbb{R}^4 orthants, and (b) the 8 Hopf-projected octants. Compare to $v_{ns} < 2 \text{ cm/s}$ from Figures 4.2 on page 92 and 4.6 on page 101.

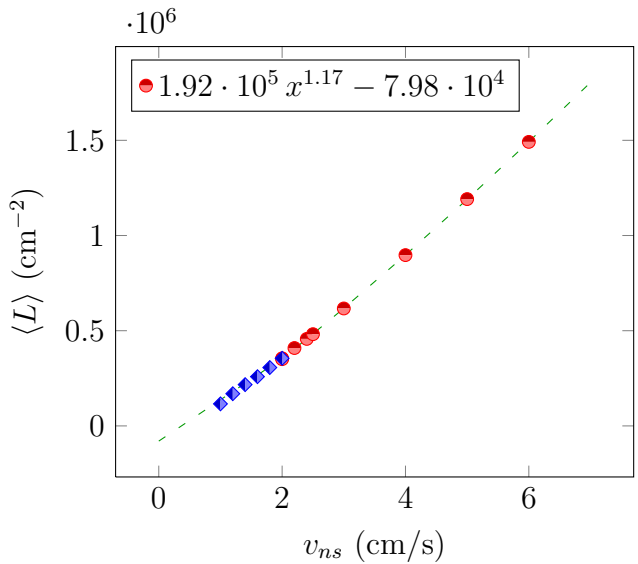


Figure 4.16: Fit of $\langle L \rangle(v_{ns})$ using averages of $v_n : [2, 6]$ cm/s, where all trials are homogeneous, both between the 16, \mathbb{R}^4 orthants and between the Hopf-projected 8, S^2 orthants. The $v_n < 2.0$ cm/s was not included in the fit but does show reasonable consistency even before homogeneity sets in at 2 cm/s.

growth from anything but the nonlocal term. The driving velocity part of the friction term, $\hat{s}' \times (\vec{v}_{ns})$, is zero because this alignment. And the local term, $\beta \hat{s}' \times \vec{s}''$ is zero because the curvature is zero. If we momentarily ignore the nonlocal field, our vortex line length would not grow with increased driving velocity: $\langle L \rangle \propto v^0$. For an isotropic system, therefore, we should expect the v^2 behavior, but if the vortex deviates greatly from isotropic, this exponent should be greatly reduced. It turns out the nonlocal field does not change this. I shall discuss these effects further in Section 4.3.4.

4.3.3 Dependence on Initial Conditions

Unlike with periodic boundaries, turbulence on the 3-sphere remains inhomogeneous for a significant range of velocities above its critical velocity. This inhomogeneity is even more clear under the Hopf fibration than in \mathbb{R}^4 . There is a notable aspect of this inhomogeneity: the equilibrated system does not depend on initial conditions. Homogeneous turbulence does not depend on initial conditions, but apparently inhomogeneous turbulence does not imply that it is dependent. The degree of randomness involved in homogeneous turbulence obliterates the way the system began. Here, even though the system is inhomogeneous, it is random enough that information from its initial state is lost.

We start most of our trials with a sinusoidally perturbed vortex ring lying parallel to the xy -plane. Figure 4.17 shows a stereographic projection of this configuration, projected from the $w = -r_0$ location. In this figure, the tangent vector points counter clockwise around the ring, such that fluid is flowing in the $+\hat{z}$ direction through the

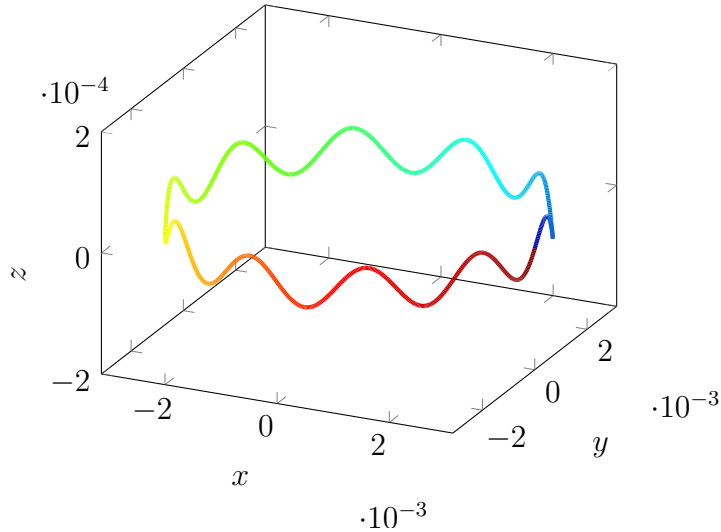


Figure 4.17: The stereographic projection of a common initial condition: a sinusoidally perturbed vortex ring lying just outside of the xy -plane. The stereographic projection is taken from the projection point, $w = -r_0$. See Appendix E.2 for details. The vortex tangent vector points along the vortex as blue fades to green and then to red – counter clockwise as viewed from above.

ring's center.

An unperturbed vortex ring precisely within the xy -plane would have a particular symmetry under the influence of the Hopf driving velocity, $\vec{v} = (-y, x, -w, z)$. Every point on this perfect ring would be carried to another point on itself by the velocity field that it experiences: $(-y, x, 0, 0)$. Now, we have a perturbed ring, so oscillations can grow and distort, forming the tangle that fills the 3-sphere. But we can compare this to another initial condition, which does not have the same symmetry as the previous: a perturbed ring oriented parallel with the yz -plane. Figure 4.18

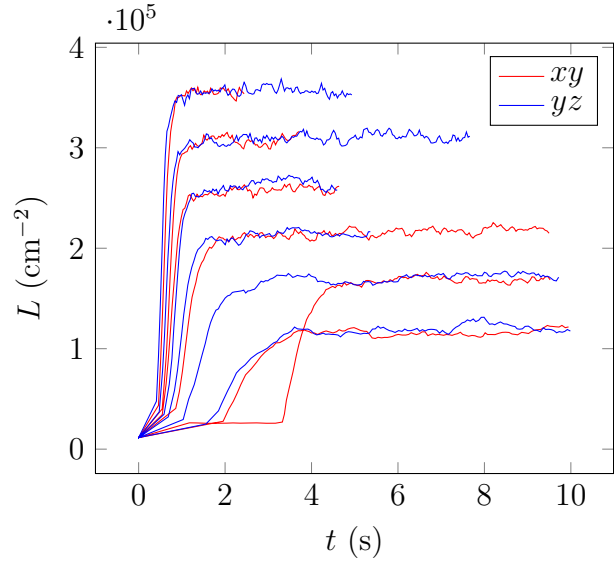


Figure 4.18: Evolution of $L(t)$ for velocities $v_{ns} = \{1, 1.2, 1.4, 1.6, 1.8, 2\}$ (cm/s), starting from different initial conditions: — a perturbed vortex ring oriented with the xy -plane, — a perturbed vortex ring oriented with the yz -plane. The — data is the same as that in Figure 4.13.

shows trials for this new initial condition as well as those starting from the perturbed vortex oriented with the xy -plane, from Figure 4.13.

Figure 4.18 shows that initial condition has little effect on the equilibrated $\langle L \rangle$. However, there is an effect on the transient state. This is apparent from the pair of curves with the second smallest $\langle L \rangle$ value ($\approx 1.7 \cdot 10^5$ cm $^{-2}$). This pair of trials both used driving velocity, $v_{ns} = 1.2$ cm/s, but it took much longer for the vortex starting aligned with the xy -plane to gain line length.

It is possible that simply changing which plane our initial perturbed vortex is

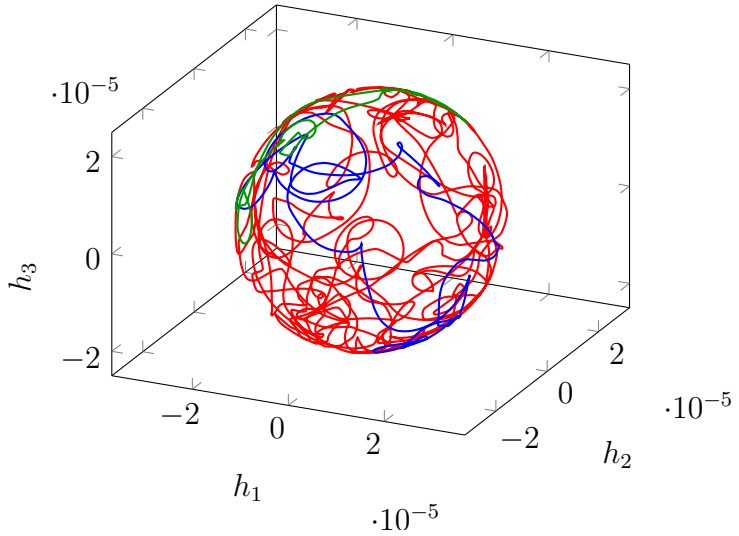


Figure 4.19: Hopf projection of the initial condition used in Figure 4.20.

aligned with is not enough to fully test the dependence of this system on its initial conditions. So, we also took the vortex tangle resulting from a higher driving velocity and used that as the seed for a new trial with lower velocity. These are truly different conditions since there is no way for the lower-velocity trial to have passed through a configuration like the higher velocity trial at any time in its development. The Hopf projection of this initial seed is shown in Figure 4.19.

The vortex tangle in this figure, indeed, appears sufficiently random. The driving velocity used to obtain this vortex tangle was, $v_{ns} = 2.0 \text{ cm/s}$. The evolution of this new trial which now uses $v_{ns} = 1.2 \text{ cm/s}$, is displayed in Figure 4.20, along with trials from Figure 4.18 with the same v_{ns} . This new driving velocity of 1.2 cm/s was selected because, according to Figure 4.2 on page 92 and Figure 4.6 on page 101, 1.2 cm/s is fairly inhomogeneous.

Clearly this higher- $\langle L \rangle$ initial configuration does not affect the final equilibrated

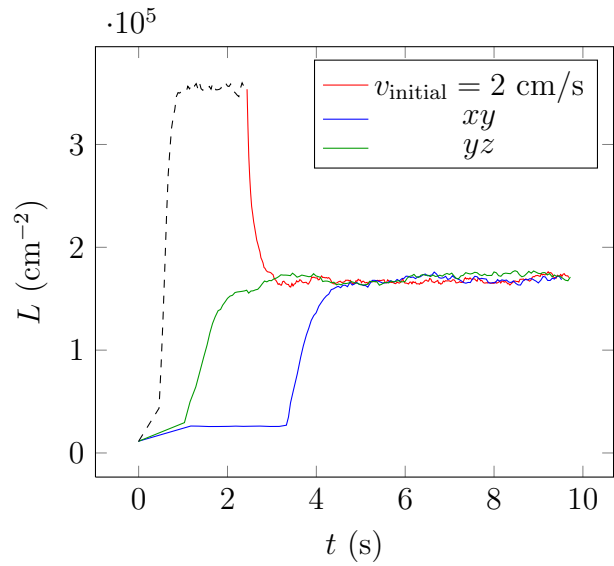


Figure 4.20: Evolution of $L(t)$ with $v_{ns} = 1.2 \text{ cm/s}$, —, but starting from a previous trial, ---, with a higher initial velocity, 2.0 cm/s . The comparison is made to two other trials, both at $v_{ns} = 1.2 \text{ cm/s}$, from Figure 4.18, starting with the initial conditions: — a perturbed ring oriented with xy -plane, — a perturbed vortex ring oriented with the yz -plane.

state. It appears that, although S^3 superfluid turbulence is significantly less homogeneous than with periodic boundaries, it is still random enough and consistent enough that the tangle obliterates information about its initial conditions.

It is interesting to note that there are some initial conditions that have a dramatic effect on the behavior of the system. I have already mentioned one, the unperturbed ring in the xy -plane. This would simply rotate in place. But a more interesting example is the perturbed ring in the xy -plane, but with tangent vector pointing opposite to that shown in Figure 4.17. The flipped xy ring is actually driven by \vec{v}_{ns} to annihilation, while other configurations (including the flipped yz ring) are sustainable.

During the initial growth period, the driving velocity needs to be responsible for an increase in the line length. Since we use only the normal fluid in this work, the only term in our equation of motion, 1.9, that we need to look at is the friction term: $\dot{\vec{s}}_g = \alpha \hat{s}' \times \vec{v}_n$. The flipped xy ring has a component of the velocity pointing along \hat{n} , nearly uniformly around the ring. We can look at the applied velocity field along the different orientations, stereographically projected in Figure 4.21. This figure shows that, for the xy ring, \vec{v}_{ns} points consistently along the binormal direction with some small tangential component. Tangential velocity does nothing to the length of the vortex, since $\alpha \hat{s}' \times \vec{v}_{ns}$ becomes zero. But depending on the orientation of the ring (the direction of \hat{s}') the binormal component can either shrink or expand the vortex. This is not true for a perturbed ring in the yz -plane. Judging from part (b) of Figure 4.21, the applied velocity field will not drive motion of the vortex in the normal direction everywhere around the ring. So the initial yz ring will not be driven

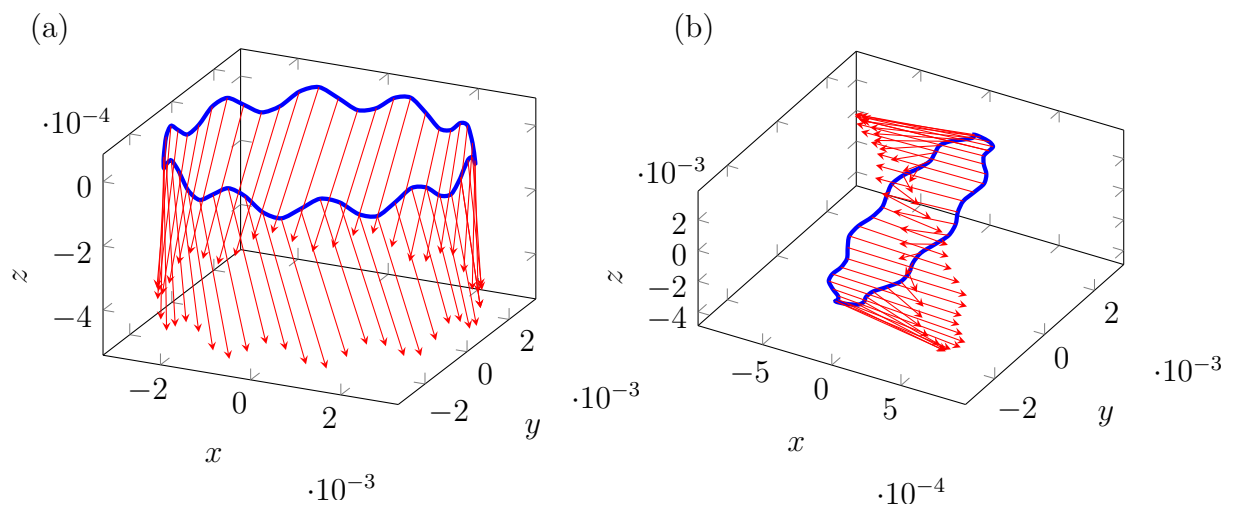


Figure 4.21: Stereographic projections of the Hopf vector field along the vortex initial conditions, (a) a perturbed ring in the xy -plane, and (b) a perturbed ring in the yz -plane.

to annihilation, but the xy ring can be, with one of the two possible orientations.

4.3.4 Discussion

We have seen that turbulence on the 3-sphere is distinct from conventional turbulence. The system is inhomogeneous for a range of velocities up to twice the critical velocity. However, the most significant difference is that vortices are polarized with the driving velocity. The I_{\parallel} data indicates significant polarization, yet the system is still highly interactive. The vortex reconnection rate is consistent with predictions for polarized turbulence. The $\langle L \rangle$ dependence on v_{ns} is also explainable by decreased growth from the driving velocity term in the equation of motion. The only other source of growth could come from the nonlocal field.

However, despite the inclusion of the Biot-Savart law, up to some significant interaction distance, our vortices still align with great circles. It turns out, this is a property of the Biot-Savart law on S^3 : divergence-free vector fields on the 3-sphere are eigenfields of the Biot-Savart law ([DeTurck and Gluck, 2004](#)). This means that if a vortex aligns with the driving velocity (which is divergence-free) the nonlocal term will drive this vortex in the same direction as the driving velocity instead of away from it. By reducing the nonlocal interaction distance, we can investigate the effects of nonlocal field further, as well as make further comparisons between 3-sphere turbulence and the periodic cube.

4.4 Varying the Nonlocal Interaction Distance, d_{NL}

All of our simulations so far have been using a particular cutoff for the flat-space Biot-Savart law: $d_{NL} = \pi r_0/2$, where this is the maximum distance along the S^3 surface that is included in the nonlocal interaction. With this value, a vortex point will interact with vortices on the nearest half of the 3-sphere. We know from Chapter 3.3 that with periodic boundaries, for d_{NL} greater than the average intervortex distance, ℓ , simulations give a good approximation to the full Biot-Savart law. We will see how properties of 3-sphere turbulence are affected by reducing d_{NL} .

4.4.1 Homogeneity

Recall from Section 4.3.1, with nonlocal interaction ($d_{NL} = 0.5\pi r_0$) the dominant structure found in the \mathbb{R}^4 orthant $\langle L \rangle$ data was the Hopf symmetry. This continues to be true with decreasing interaction distance, as shown in Figure 4.22.

The fact that this Hopf symmetry is still so prevalent with decreased d_{NL} suggests that this alignment is insensitive, perhaps immune, to changes in the nonlocal interaction. We can look deeper to see how these occupied Hopf fibers are distributed over the 3-sphere. Figure 4.23 shows the Hopf-projected \mathbb{R}^3 octant $\langle L \rangle$ data.

Here, we see again that some of trials exhibit the inversion antisymmetry we saw in Figures 4.6 and 4.7. But we have more data to work with now, which allows us to make more general conclusions. Take for example the $v_{ns} = 1.2$ cm/s trials from Figure 4.7 and from (a), (b) and (c) of Figure 4.23. At $d_{NL} = \{0.5\pi r_0, 0.33\pi r_0, 0.25\pi r_0\}$, there is an approximate inversion antisymmetry. At $d_{NL} = 0.42\pi r_0$, there is not. It

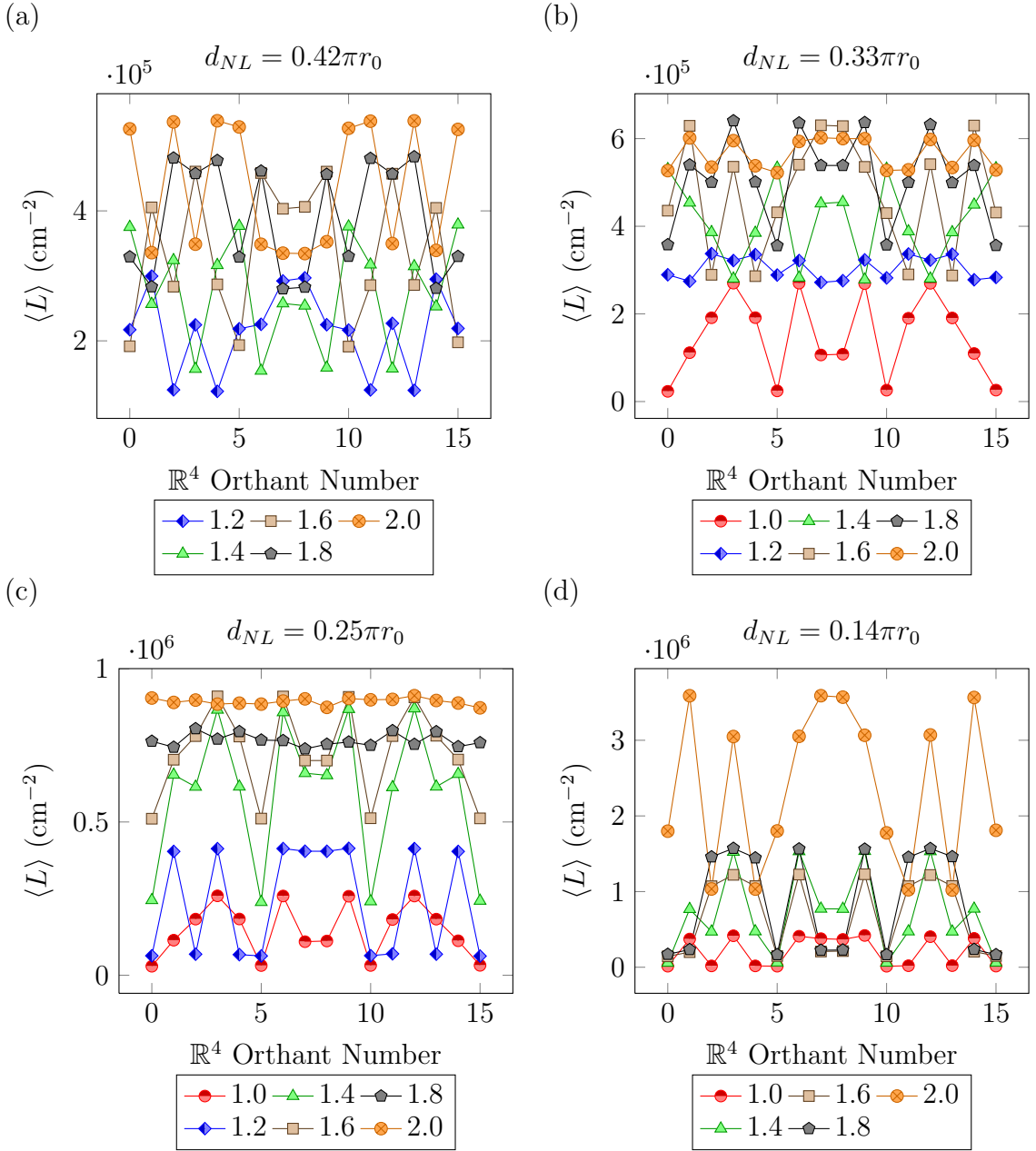


Figure 4.22: Average \mathbb{R}^4 orthant $\langle L \rangle$ data for several velocities, at d_{NL} values of (a) $0.42\pi r_0$, (b) $0.33\pi r_0$, (c) $0.25\pi r_0$, and (d) $0.14\pi r_0$. Within every figure, each curve represents a different v_{ns} (cm/s) labeled within the legend. Note a strong Hopf symmetry, as with $d_{NL} = 0.5\pi r_0$ in Figure 4.2.

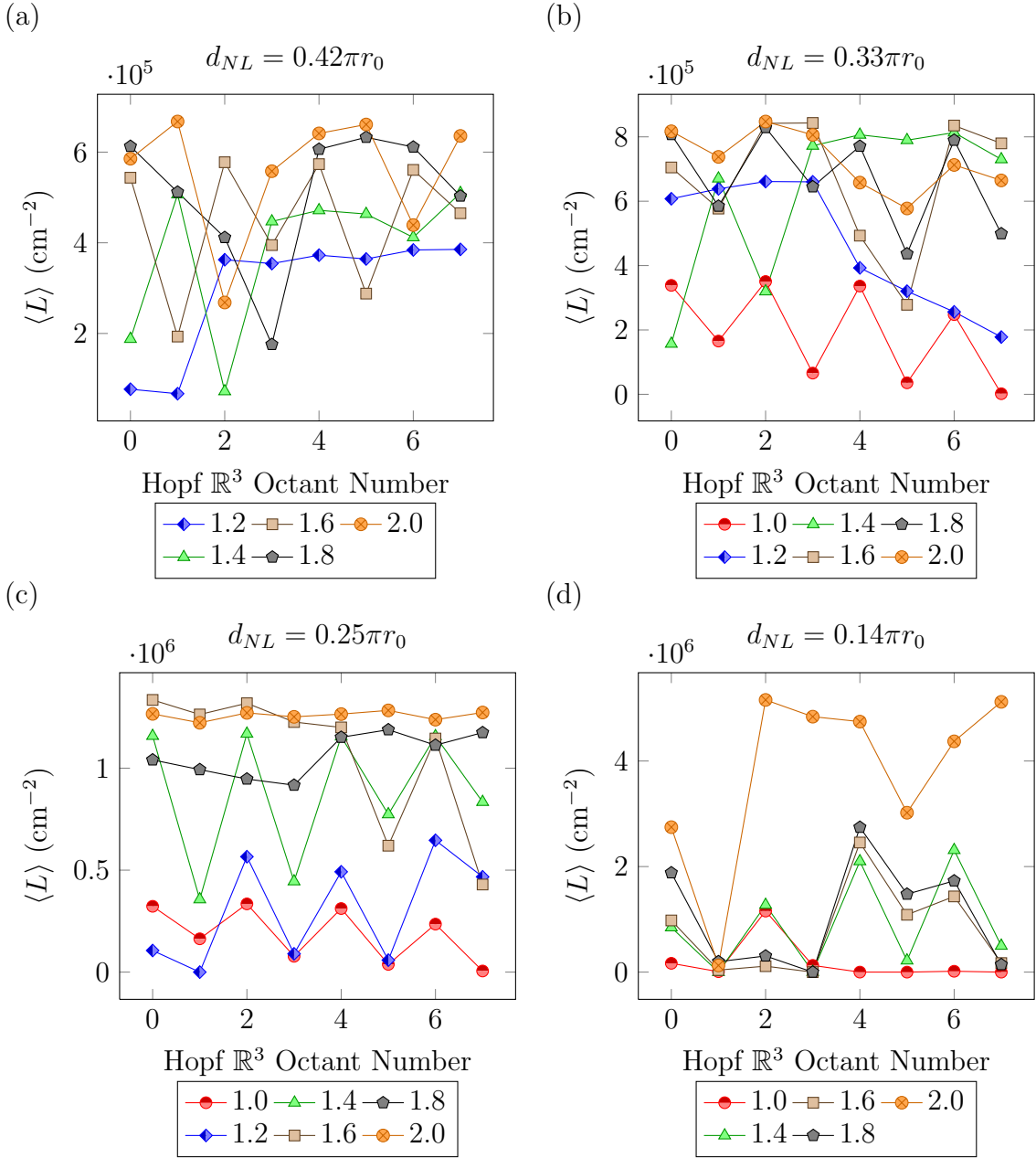


Figure 4.23: Average Hopf-projected \mathbb{R}^3 orthant $\langle L \rangle$ data for several velocities, at d_{NL} values of (a) $0.42\pi r_0$, (b) $0.33\pi r_0$, (c) $0.25\pi r_0$, and (d) $0.14\pi r_0$. Within every figure, each curve represents a different v_{ns} (cm/s) labeled within the legend.

appears sporadically for the other velocities, as well. We concluded that when the vortex tangle does not occupy the full S^3 volume, it tends to condense somewhat to one region and away from the antipode. There is also the tendency for this region to shift and distort over time, which we saw in the extended simulation from Figure 4.10. Given the sporadic nature, the inversion antisymmetry of our Hopf-projected \mathbb{R}^3 octant data appears to be slight and dependent on the time domain over which we perform averages.

4.4.2 Anisotropy and Line Length Density

Figure 4.24 (a) shows the average anisotropy parameter, I_{\parallel} , as a function of applied v_{ns} for a range of interaction lengths, d_{NL} . Figure 4.24 (b) shows the average $\langle L \rangle(v_{ns})$ with varied d_{NL} for the same trials.

I_{\parallel} does not show a consistent trend as d_{NL} is varied in this range of d_{NL} values. However, in all cases the low values of I_{\parallel} still show alignment with the Hopf driving velocity \hat{v}_{ns} . These anisotropy values equate to an average of about 85-95% alignment of the tangent vector with the driving velocity. This is useful information. One worry may be whether these results would be similar if we had used the full S^3 form of the Biot-Savart integral instead of modifying the Euclidean form. I show in Section 4.4.4 that our adapted integral produces qualitatively similar nonlocal velocity fields to the S^3 form.

Let us now turn to the line length density in Figure 4.24 (b). At low velocities, $\langle L \rangle$ does not deviate much from the largest d_{NL} values. But as v_{ns} increases, the deviation gets more pronounced as d_{NL} is decreased. This particular trend with

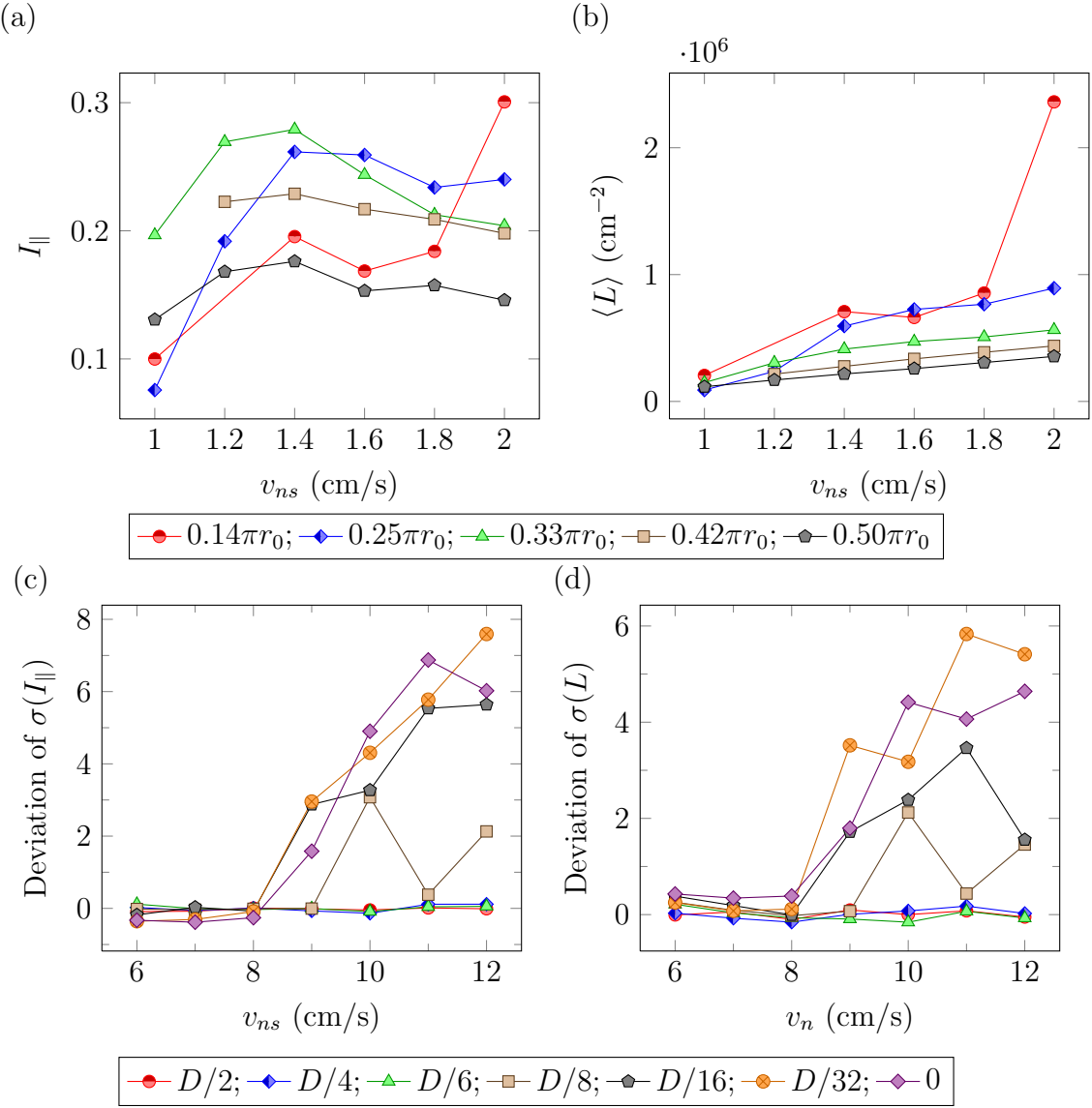


Figure 4.24: Comparison of (a) $I_{\parallel}(v_{ns})$ and (b) $\langle L \rangle(v_{ns})$ for S^3 turbulence. Each curve represents a series of trials at different d_{NL} values, given in the legend. Omitted data in $d_{NL} = 0.14\pi r_0$ and $0.42\pi r_0$ are due to turbulence being unsustainable for the initial configuration used throughout these trials: a sinusoidally perturbed ring in the xy -plane. For convenience, Parts (c) and (d) show the deviation of $\sigma(I_{\parallel})$ and $\sigma(L)$, respectively, from the full Biot-Savart calculation for different d_{NL} values using the periodic cube geometry, (taken from Figure 3.22 on page 78).

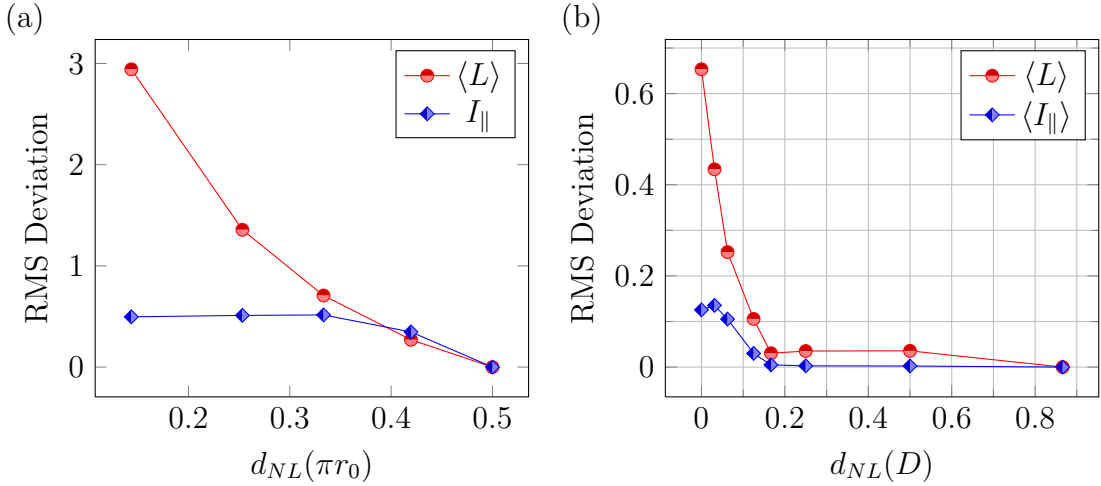


Figure 4.25: Part (a) shows the Root-Mean-Square fractional deviation of $\langle L \rangle$ and I_{\parallel} as a function of d_{NL} for S^3 turbulence ($r_0 = 0.005$ (cm)). Part (b) shows similar data for the periodic cube geometry, taken from Figure 3.19 (a) on page 73.

v_{ns} is qualitatively similar to the behavior with periodic boundaries (best shown in the standard deviations of the quantities L and I_{\parallel} in Figure 3.22 and repeated in Part (c) and (d) of Figure 4.24). However, the 3-sphere $\langle L \rangle$ changes gradually and significantly with decreasing d_{NL} , while the periodic cube behavior stays relatively constant until a critical d_{NL} value is reached. This is particularly clear when viewing Figure 4.25. Part (a) shows the root-mean-square deviation of $\langle L \rangle$ and I_{\parallel} from that with $d_{NL} = \pi r_0 / 2$ for the 3-sphere. Part (b) shows similar data for the periodic cube geometry, taken from Figure 3.19 (a).

While deviations from nonlocal calculations transition discretely in the periodic cube, the 3-sphere deviates much more gradually. This is understandable from the

degree of vortex polarization. Turbulence in the periodic cube is much more isotropic. Thus, contributions to the nonlocal field experience large cancellations, leading to a relatively small mean field. However, significant alignment of vortices in the 3-sphere means contributions from different vortices do not experience this cancellation. So decreasing the d_{NL} has a more significant and gradual effect on the system.

4.4.3 Dependence on Initial Conditions

We have seen that 3-sphere turbulence with long-range nonlocal interactions is independent of initial condition, despite being inhomogeneous. We will now look at how this property is affected by reducing d_{NL} . Figure 4.26 compares the $\langle L \rangle$ data for the initial conditions discussed previously, a perturbed ring in the xy -plane or yz -plane, for different d_{NL} values.

Figure 4.26 (a) shows no significant variation between the two different initial conditions. Reducing d_{NL} even further shows a dependence on initial conditions at the lowest velocity of $d_{NL} = 0.25\pi r_0$. By $d_{NL} = 0.14\pi r_0$, the system depends strongly on its initial state. We can view this dependence for $d_{NL} = 0.25\pi r_0$ in a graph of the evolution of $L(t)$ shown in Figure 4.27.

It makes sense that lower-velocity trials should depend more on their initial conditions, since there is more change in line length from the initial state with higher velocities. Like with longer nonlocal interactions in Section 4.3.3, we have also started the system from a vortex tangle produced by a higher driving velocity. These data are shown in Figure 4.28.

Here, we see more evidence of dependence on initial conditions for $d_{NL} \leq 0.25\pi r_0$.

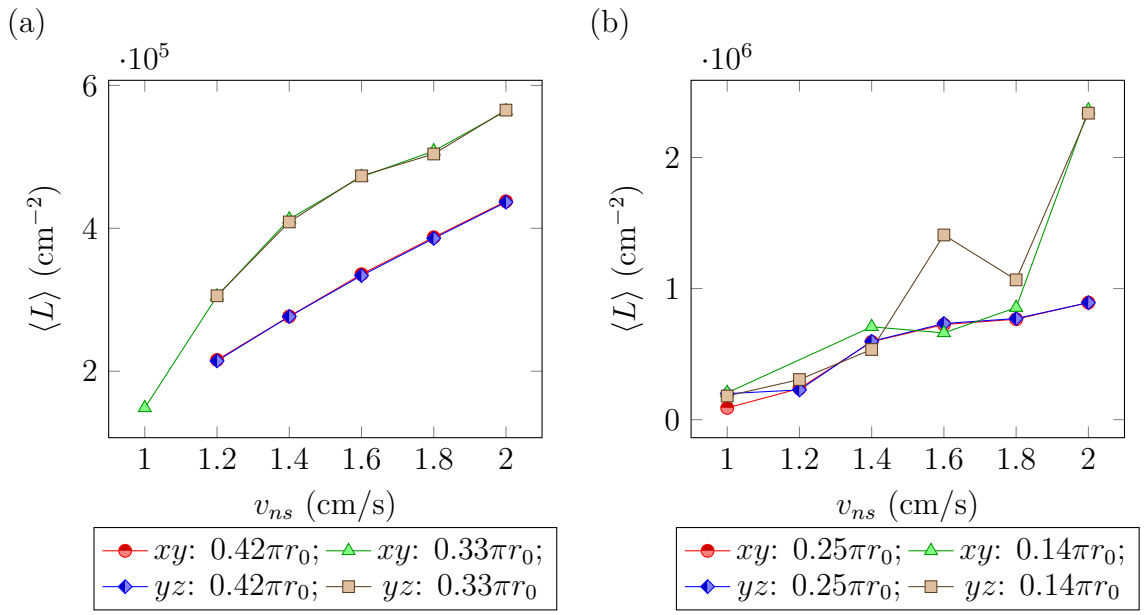


Figure 4.26: The equilibrated $\langle L \rangle$ is shown comparing the two initial conditions: a perturbed ring in the xy -plane or yz -plane. (a) Shows curves for $d_{NL} = 0.42\pi r_0$ and $0.33\pi r_0$ and (b) shows curves for $d_{NL} = 0.25\pi r_0$ and $0.14\pi r_0$.

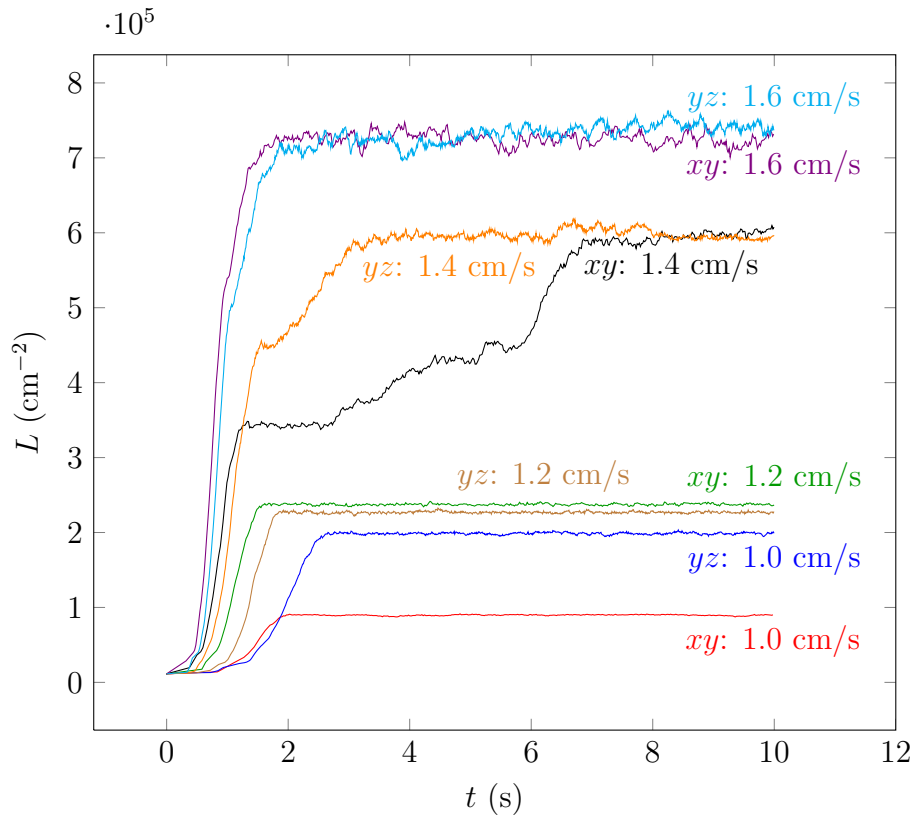


Figure 4.27: Evolution of $L(t)$ for the two initial conditions: a perturbed ring in the xy -plane or yz -plane, all at $d_{NL} = 0.25\pi r_0$, is shown for v_{ns} values up to 1.6 cm/s. This shows the trend that the equilibrated states depend more on initial conditions at lower velocities than at higher velocities.

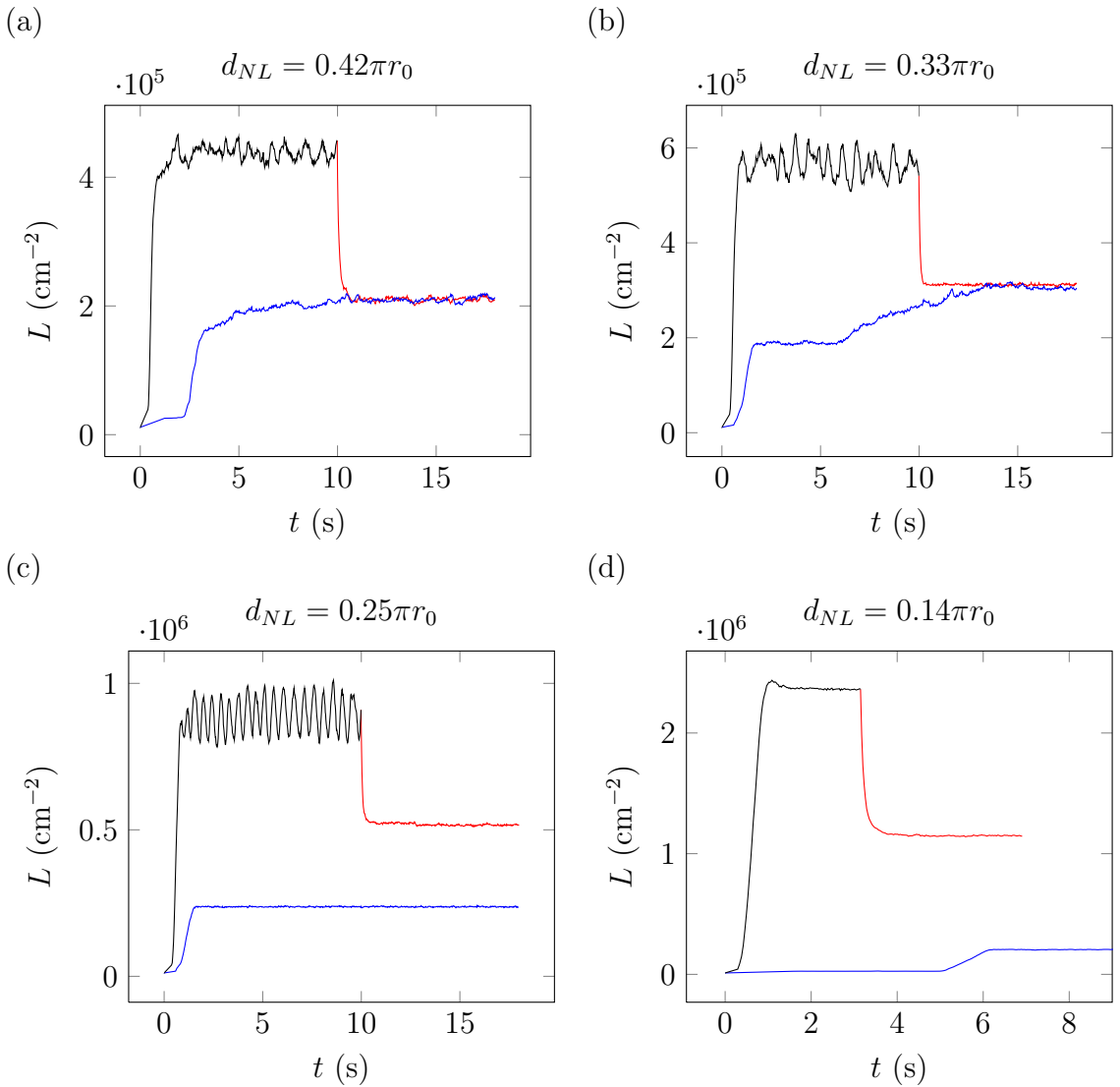


Figure 4.28: Evolution of $L(t)$ showing dependence on initial conditions for d_{NL} equal to (a) $0.42\pi r_0$, (b) $0.33\pi r_0$, (c) $0.25\pi r_0$, and (d) $0.14\pi r_0$. For each figure, two trials are shown with driving velocity $v_{ns} = 1.2 \text{ cm/s}$, except (d) where both trials use 1.0 cm/s . These two trials were started either from a perturbed vortex ring in the xy -plane or from a vortex tangle obtained from a trial using a higher velocity (black curves). For $d_{NL} \leq 0.25\pi r_0$, the equilibrated system depends on initial conditions.

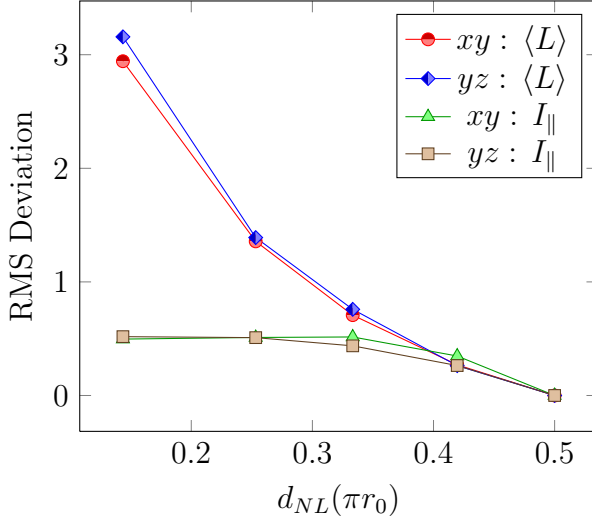


Figure 4.29: A comparison is shown of the Root-Mean-Square fractional deviation of $\langle L \rangle$ and I_{\parallel} as a function of d_{NL} for the two initial conditions: a perturbed ring in the xy -plane and yz -plane. xy -plane data was taken from Figure 4.25.

It appears that the interactions help destroy this dependence on the system's beginnings. This makes sense from the simple perspective that any interactions will drive the system away from its earlier state. Having a greater interaction volume means depending less on initial conditions. This means that the root-mean-square deviation from our nonlocal calculations is affected primarily at the low d_{NL} end. Figure 4.29 shows these data for both the perturbed ring in the xy -plane and yz -plane.

Figure 4.29 shows the same gradual, significant change in the system behavior for S^3 turbulence between the two initial conditions. This gradual change obviated, to some degree, the need to look at the average intervortex distance, $\langle \ell \rangle = \langle L \rangle^{-1/2}$. Recall that with periodic boundaries, $\langle \ell \rangle$ was the physical length scale that told us

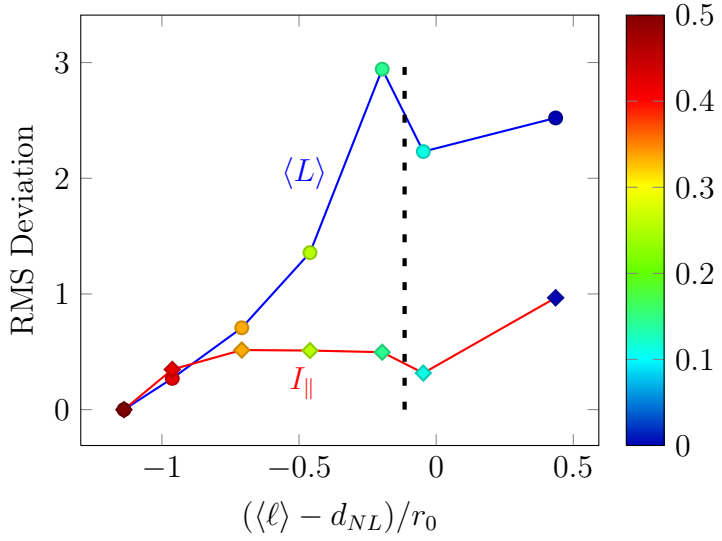


Figure 4.30: Root-Mean-Square fractional deviation of the two curves $\langle L \rangle$ and I_{\parallel} as a function of the difference between the average intervortex distance, $\langle \ell \rangle$, and the interaction distance, d_{NL} . Each data point represents data from a series of trials at that particular d_{NL} value, and uses the average $\langle \ell \rangle$ over all trials in the series. The color scale gives the d_{NL} value for each trial and the vertical line marks the shortest interaction distances discussed thus far.

how long an interaction distance we needed to accurately mimic the full Biot-Savart calculation. Thus far, the calculations presented all involve nonlocal interactions $\langle \ell \rangle < d_{NL}$, so there was still significant interaction. Figure 4.30 shows how $\langle \ell \rangle$ compares to d_{NL} for the trials discussed thus far. Since $\langle \ell \rangle$ depends on $\langle L \rangle$ which also depends on d_{NL} , the color scale shows the d_{NL} value for the set of trials contributing to each data point.

If the qualitative behavior of the periodic cube carries over, Figure 3.23 on page 80 tells us that decreasing d_{NL} until $\langle \ell \rangle - d_{NL} \ll r_0$ will lead to a significant change in the system behavior.

4.4.4 The Effects of Nonlocal Interactions

Thus far, we have seen that as the nonlocal interaction distance decreases, the homogeneity maintains roughly the same structure. There is still evidence of the Hopf structure in the \mathbb{R}^4 orthant homogeneity (Figure 4.22) and some trials show a hint of vortices condensing from some region of the 3-sphere to its antipode, as seen in the Hopf octant homogeneity (Figure 4.23). The \mathbb{R}^4 inhomogeneity is in line with the anisotropy, I_{\parallel} , showing that, although there is some variation, vortices still align significantly with the Hopf fibers along \hat{v}_{ns} (Figure 4.24 (a)). The largest changes to the system occur in the line length density (Figure 4.24 (b)) and the dependence on initial conditions (Figure 4.28).

We will now look at how the system behaves if nonlocal interactions are removed entirely. Since we are already aware of the strong dependence on initial conditions at this interaction range, we will primarily be attempting to use the data to understand qualitative behavior and trends. The $\langle L \rangle$ behavior is similar to Figure 4.24 (b): erratic at higher velocities and significantly larger than for $d_{NL} = 0.5\pi r_0$. Figure 4.31 shows the anisotropy parameter for the lowest values of d_{NL} .

There is a steady decrease in I_{\parallel} as d_{NL} is decreased, indicating that vortices align even further with the driving velocity. This is the dominant factor in the system's homogeneity, which leads to a more distinct presence of the Hopf symmetry in the

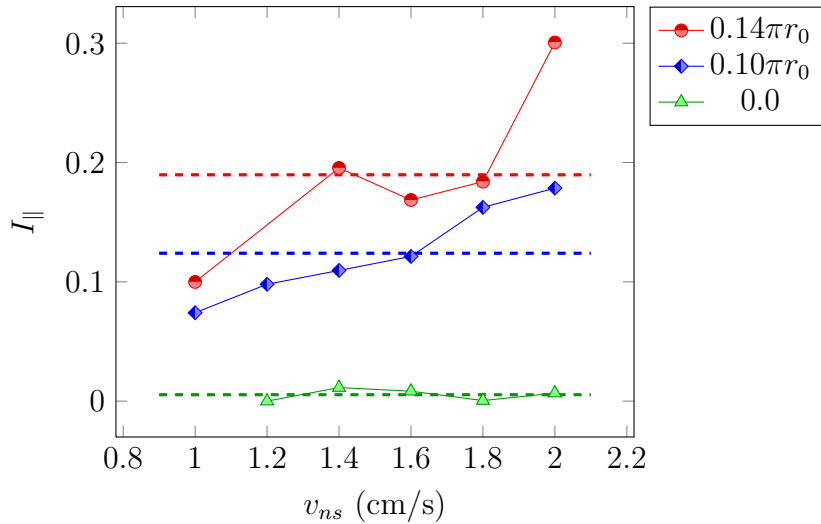


Figure 4.31: Comparison of $I_{\parallel}(v_{ns})$ for small d_{NL} . Each curve represents a series of trials at different d_{NL} values, given in the legend. Dashed lines show averages for each d_{NL} series, and are inserted as guides to the eye. Omitted data are due to turbulence being unsustainable for the initial configuration used throughout these trials: a sinusoidally perturbed ring in the xy -plane.

\mathbb{R}^4 orthant homogeneity data. But there is a more significant change in the system than this, which is best revealed with snapshots of the system in the equilibrated state. These are shown in Figure 4.32.

Figure 4.32 reinforces the I_{\parallel} data indicating that removing the nonlocal interaction increases alignment with the Hopf velocity, \hat{v}_{ns} . But furthermore, there is a tendency in the local regime for vortices to cluster in the same region of space. This demonstrates the well-known ability for parallel vortices to repel each other via the nonlocal interaction, as noted by Schwarz (1985). Of course, two parallel vortex segments are still able to reconnect but drive each other to distort until the angle is more appropriate, before doing so.

The Hopf fibers that foliate the 3-sphere are parallel (DeTurck and Gluck, 2004), but vortices could occupy these great circles in random orientations. They do not do so because of the way that the vortex tangle grows. Deviations of the initial vortex from the great circle grow until the vortex folds over on top of itself. A vortex reconnection occurs leading to two parallel vortices. The nonlocal interaction prevents these vortices from occupying great circles too near each other. Figure 4.33 shows an example of this process under stereographic projection.

The simple fact that vortices occupy great circles requires some investigation. It suggests that great circles are a stable point for the vortex equation of motion. DeTurck and Gluck (2004) states that for a divergence-free vector field, the full Biot-Savart law on the 3-sphere is expected to yield a resultant vector field which lies tangent to the original. Our vortices lie primarily tangent to the Hopf velocity, which as we discussed in Section 4.2, is divergence free. Our vortices are the

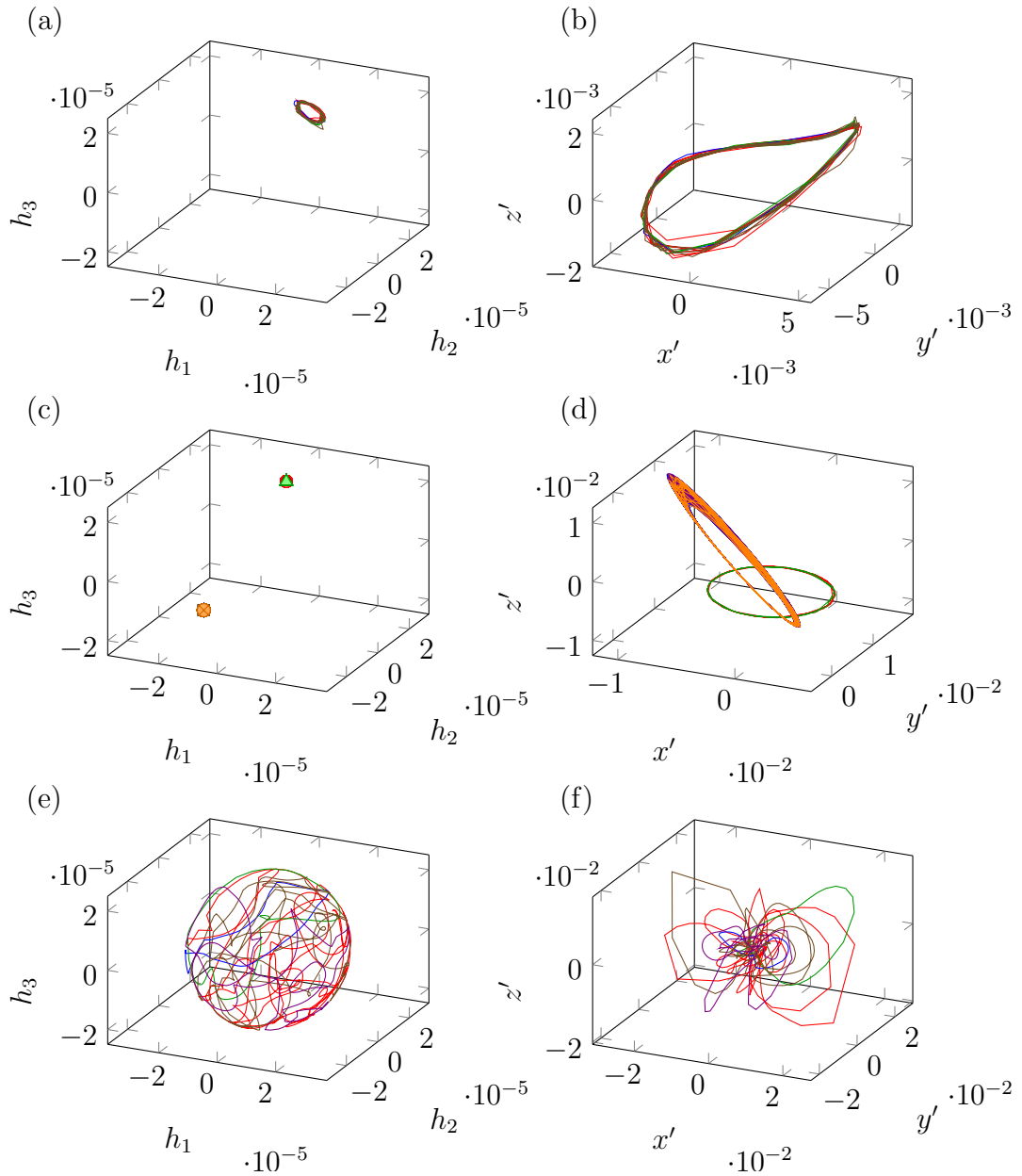


Figure 4.32: Snapshots of the equilibrated vortex tangle with $d_{NL} = 0$ for (a), (b) $v_{ns} = 1.6$ cm/s, and (c), (d) $v_{ns} = 1.8$ cm/s. Figures (a) and (c) use the Hopf projection, and (b) and (d) use the stereographic projection. Similar snapshots with nonlocal interactions, $d_{NL} = 0.5\pi r_0$, and with $v_{ns} = 1.8$ cm/s are shown in (e) and (f).

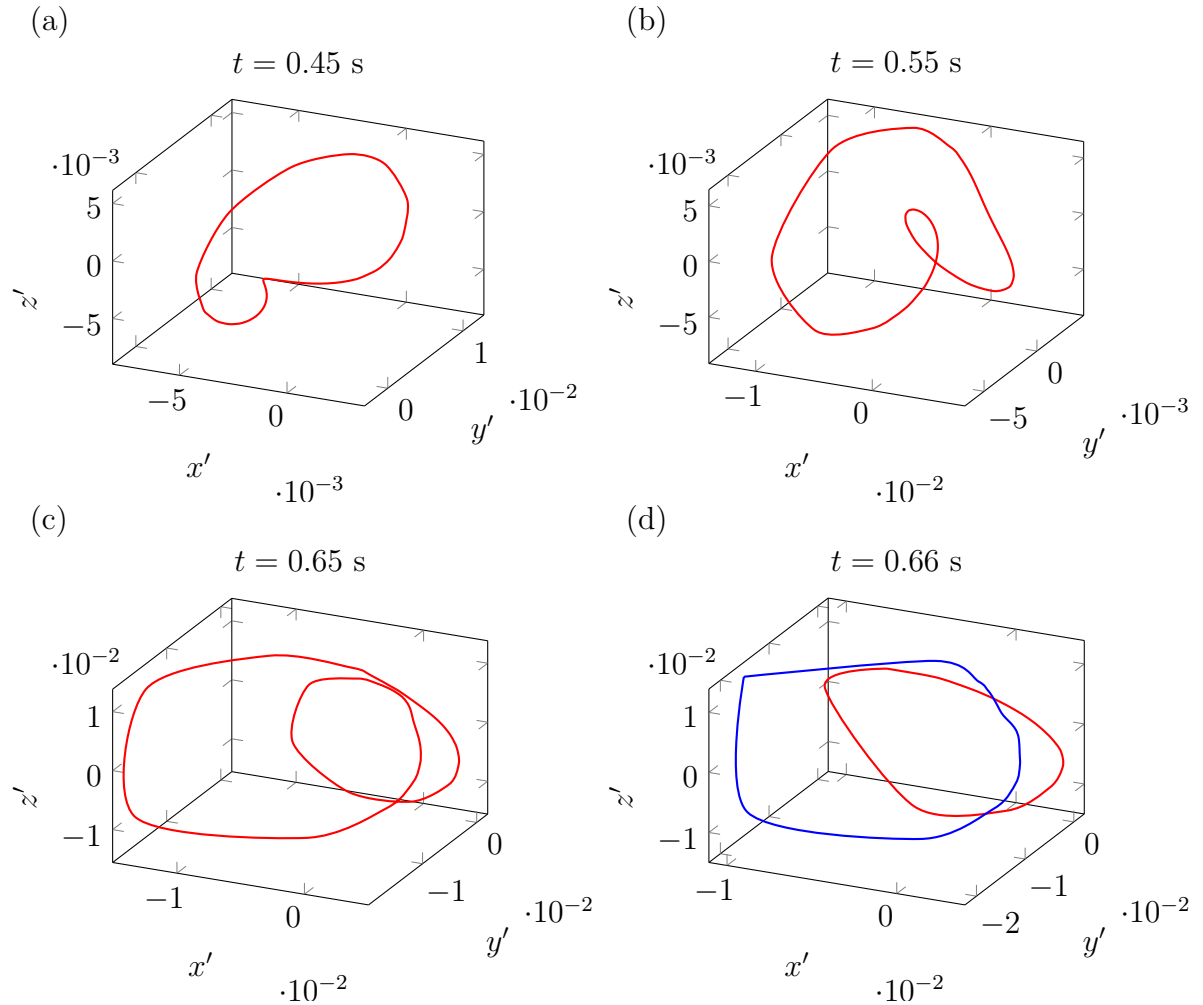


Figure 4.33: Snapshots of the growth of a vortex with $d_{NL} = 0$, demonstrating the initial perturbed vortex, under stereographic projection.

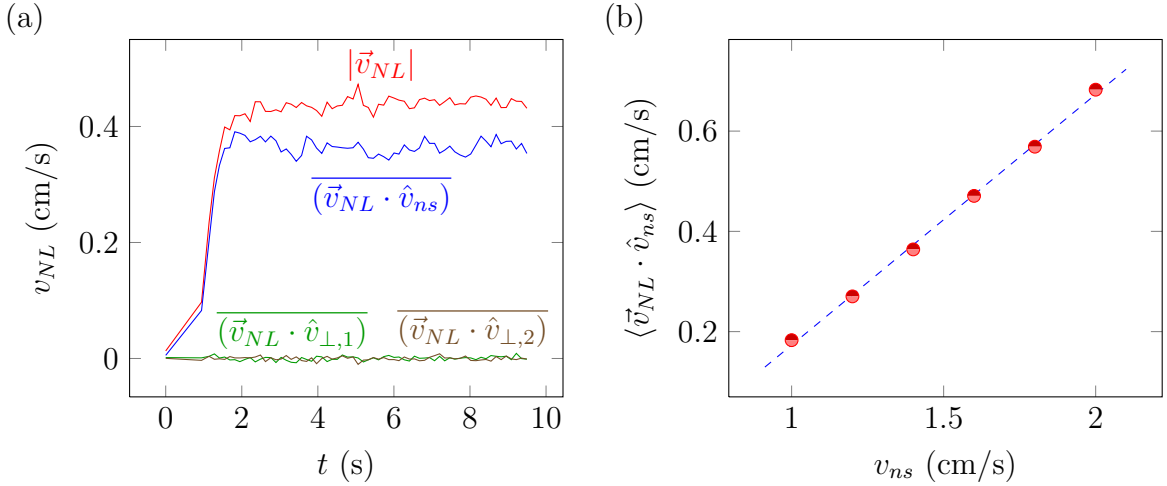


Figure 4.34: Figure (a) shows the average components of the nonlocal velocity, v_{NL} , along \hat{v}_{ns} , and the two perpendicular components, $\hat{v}_{\perp,i}$. The quantities are averaged over the vortex line length. This trial uses $v_{ns} = 1.4$ cm/s, and $d_{NL} = 0.5\pi r_0$. Figure (b) shows the average equilibrated $\vec{v}_{NL} \cdot \hat{v}_{ns}$ for a series of velocities, with $d_{NL} = 0.5\pi r_0$.

source vector field producing a nonlocal velocity parallel with \hat{v}_{ns} : $BS(\hat{s}') = c\vec{v}_{ns}$, where c is positive since our velocity field is right-invariant (see Appendix F.1). Figure 4.34 (a) shows the evolution of components of the nonlocal velocity averaged over a representative vortex tangle.

The fact that vortices do not perfectly align with \hat{v}_{ns} means we should not expect perfect alignment of \hat{v}_{NL} with \hat{v}_{ns} . We also may not expect c to be constant with changing v_{ns} . We use the Euclidean Biot-Savart integral, which is only over the vortex filaments, and only those within d_{NL} of each vortex point. Clearly the nonlocal

velocity should depend on the line length density, however this also increases with driving velocity. Figure 4.34 (b) shows the relation between the average nonlocal velocity, tangent to \hat{v}_{ns} , for the equilibrated time domain. This figure provides a degree of validation to our choice to use the Euclidean Biot-Savart law, which we originally made on other grounds, as a new approach to the open-orbit problem that occurs with periodic boundaries. Our qualitative agreement with the S^3 Biot-Savart law suggests qualitatively similar behavior if we chose to use this form of the integral in our equation of motion.

Having noted this property of the nonlocal interaction, analyzing the relevant part of the vortex equation of motion can show us how great circles are a vortex stationary state on the 3-sphere.

$$\dot{\vec{s}} = \vec{v}_{local} + \vec{v}_{NL} + \alpha \hat{s}' \times (\vec{v}_{ns} - \vec{v}_{NL} - \vec{v}_{local})$$

When the vortex tangle aligns perfectly with \hat{v}_{ns} , the local velocity is zero, since vortices along great circles have zero local curvature. The nonlocal velocity for a given trial is given by: $\vec{v}_{NL} = c\vec{v}_{ns}$, with $0 < c < 1$, and thus they both point along great circles. With both \vec{v}_{ns} and \vec{v}_{NL} parallel to \hat{s}' , the friction term is zero. And lastly, \vec{v}_{NL} simply rotates a vortex filament along the great circle upon which it lies. However, when the vortex tangle only aligns with \hat{v}_{ns} on average, the dominant nonlocal term cancels some of the driving velocity but there are other components (including \vec{v}_{local}) that can maintain some of the randomness of the tangle. Outside of the friction term, \vec{v}_{local} preserves line length (Buttke, 1986, e.g.) and inside the friction term, the resultant vector always points in the \hat{n} direction, straightening the

vortex (reducing its curvature). The driving velocity, however, can cause sections of the vortex not aligned with \hat{v}_{ns} to grow.

It is worth noting that it seems like great circles should not be stationary states. A vortex along the a great circle has a curvature vector which points toward the center of the 3-sphere. While it seems like this should result in local motion, this is not the case. Imagine a vortex lying along a great circle, say in the xy -plane. In \mathbb{R}^4 , there is no one vector in the direction of the local velocity, binormal to the vortex. Now, the entire zw -plane is perpendicular to the plane of the vortex. Another way to view it is that the curvature vector points perpendicular to this S^3 space, and we are left with the a vortex with zero curvature in the three dimensional system volume. A perfectly “straight” vortex on the 3-sphere cannot leave the great circle it is on with local motion alone.

4.5 References

- Adachi, H., Fujiyama, S., and Tsubota, M. *Physical Review B*, **81**, 1 (2010).
- Barenghi, C. and Samuels, D. *Journal of Low Temperature Physics*, **136**, 281 (2004).
- Buttke, T. F. *A Numerical Study of Superfluid Turbulence in the Self-Induction Approximation*. PhD thesis, University of California, Berkeley (1986).
- DeTurck, D. and Gluck, H. *arXiv:math/0406276* (2004).
- Kuperberg, G. *arXiv:math/0610904v3* (2008).
- Nemirovskii, S. *Physical Review Letters*, **96**, 015301 (2006).

- Schwarz, K. W. *Physical Review B*, **31**, 5782 (1985).
- Schwarz, K. W. *Physical Review B*, **38**, 2398 (1988).
- Swanson, C. E. and Donnelly, R. J. *Journal of Low Temperature Physics*, **61**, 363 (1985).
- Tough, J. *Progress In Low Temperature Physics*, volume VIII. North-Holland Publishing Company (1982).
- Tsubota, M., Araki, T., and Nemirovskii, S. *Physical Review B*, **62**, 11751 (2000).
- Tsubota, M., Barenghi, C. F., Araki, T., and Mitani, A. *Physical Review B*, **69**, 134515 (2004).

Chapter 5

Conclusion

5.1 Periodic Boundaries

Periodic boundaries provide a valuable tool for simulating He II superfluid turbulence. A periodic system has the benefit of saving computation time by eliminating the complexity of real-wall boundaries, and by allowing turbulence to become homogeneous throughout the entire system volume. However it also allows a vortex to reconnect with itself while straddling one of these periodic walls, creating an open-orbit vortex. Since the periodic box is equivalent to a flat 3-torus, this state is topologically distinct from normal vortex behavior and another reconnection is required to break free from it. The stability of open-orbit vortices leads to a system of parallel straight vortices, which is by no means turbulent.

There have been several attempts at solving the open-orbit vortex problem in the past. The most physical and successful of which involved using the fully non-local Biot-Savart integral (Adachi et al., 2010), in contrast to the local induction approximation that was previously used for simulating homogeneous He II turbu-

lence. However, the fully nonlocal integral is also more computationally expensive. We sought a more nuanced approach to this problem by truncating the maximum allowed nonlocal interaction distance.

I began by showing that our simulation accurately produces the behavior characteristic of homogeneous He II turbulence using the full Biot-Savart law. We focused on a system temperature of $T = 1.6$ K for easy comparison with previous simulations. This temperature is equivalent to parameter values $\alpha = 0.1$ and $\alpha' = 0$ in the vortex equation of motion. The line length density produced by our simulation obeys the approximate scaling relation $\langle L \rangle \propto (v_{ns}/\beta)^2$. The anisotropy parameters are consistent with previous simulations in that vortices are approximately isotropic with a slight tendency toward aligning in planes normal to the driving velocity ($I_{\parallel} = 0.76$). The mutual friction force density is proportional to v_{ns}^3/β^2 , in line with experiment and prior simulations. Similarly, the average vortex drift velocity is proportional to v_{ns} . Quantitative comparisons for these values show good agreement with previous works, as seen in Table 3.1 on page 66. Lastly, I showed that the vortex reconnection rate obeys $\dot{n} = 0.42\kappa\langle L \rangle^{2.47}$, which is consistent with previous studies.

Decreasing the maximum nonlocal interaction distance d_{NL} from that of the full Biot-Savart law led to very little change in $\langle L \rangle$, I_{\parallel} , or their standard deviations. Not until a critical d_{NL} does the system deviate from the full nonlocal calculation, as shown in Figure 3.23 on page 80. This critical d_{NL} value is equal to the average inter-vortex distance $\langle \ell \rangle$. Truncating the Biot-Savart integral to less than this value results in significant errors in the resultant vortex tangle. However, maintaining interactions much greater than this distance produces only a marginal increase in accuracy. In

addition to reducing the number of computations, this result characterizes the interactions necessary for maintaining homogeneous turbulence. It indicates that the average nearest-neighbor interactions are the dominant vortex-vortex interactions necessary for maintaining homogeneity in He II turbulence.

5.2 3-sphere

We also looked at superfluid turbulence on the 3-sphere geometry as an answer to the open-orbit problem. The resultant vortices effectively loop around a hole in the 3-torus (periodic box), a state which is topologically different from normal vortex motion. The 3-sphere geometry is simply connected and thus offered an unusual potential solution to the open-orbit problem. To do so requires use of the Hopf velocity field, $(-y, x, -w, z)$. This velocity field has the interesting characteristic of being an eigenfield of its curl on the 3-sphere: a Beltrami field.

The most striking characteristic of He II turbulence on the 3-sphere is the anisotropy: vortices tend to align with the driving velocity. Homogeneous superfluid turbulence on the 3-torus is characterized by a slight anisotropy where vortices align in planes perpendicular to the driving velocity, $I_{\parallel} \gtrsim 2/3$. Vortices on S^3 align significantly more along the driving velocity, \hat{v}_{ns} (Figure 4.11 on page 109). This polarization is visible as a Hopf symmetry in the \mathbb{R}^4 orthant line length density data (Figure 4.3 on page 93). With high enough velocity, this particular structure disappears. Though the system becomes homogeneous for $v_{ns} \geq 2$ cm/s, even in this domain turbulence does not regain the characteristic scaling behavior, $\langle L \rangle = c_L^2(v_{ns}/\beta)^2$ (Figure 4.16

on page 116). This is understandable from the system's anisotropy. While $I_{\parallel} \approx 0.2$, vortices are unable to gain significant line length from increased driving velocity.

If we apply the Hopf projection to our system, taking Hopf fibers on S^3 to distinct points on S^2 , the structure of this projected line length per octant volume can show whether vortices preferentially align along particular great circles over others. There is a slight tendency for vortices to contract toward a region of the projected S^2 , away from the antipode of this point. This shows up as a mirror antisymmetry in the Hopf orthant $\langle L \rangle$, as shown in Figure 4.7 on page 103. The tendency for vortices to coalesce in a region of great circles of the 3-sphere is much more prominent when nonlocal interactions are removed, however, as shown in Figure 4.32 on page 140.

As we decrease the nonlocal interaction distance, d_{NL} , the system behavior is qualitatively similar over a large range of d_{NL} . However, the equilibrated $\langle L \rangle$, although robust at longer nonlocal interaction distances, becomes dependent on initial conditions (Figure 4.28 on page 134). One significant deviation from turbulence in the periodic cube is how much the system varies with decreased d_{NL} . The periodic cube changes very little with decreased d_{NL} until approaching the average intervortex distance (Figure 3.23 on page 80 in Chapter 3). However there is significant deviation long before this point in the 3-sphere (Figure 4.30 on page 136). This is likely due to the polarization of the vortices with the great circles of the 3-sphere. The nonlocal interaction for a highly random vortex tangle has a great deal of cancellation. The fact that vortices on the 3-sphere align so significantly with parallel great circles means the Biot-Savart law value will also change significantly as the interaction region is decreased, leading to an appreciable change in the vortex dynamics. In other

words, the mean field due to an organized system of vortices is appreciable.

Finally, removing nonlocal interactions altogether revealed the tendency for parallel vortices to repel each other, since without nonlocality they were unable to do so (Figure 4.32 on page 140). We also investigated why these vortices were parallel and not a random distribution of parallel and antiparallel vortices, largely aligned with the Hopf fibers. The vortex system tends to grow by a vortex folding over onto itself, which means vortices are preferentially parallel with each other. We showed that Hopf fibers are stationary states of the vortex equation of motion on the 3-sphere, as we know they must be from our data. This is true because of the nature of Biot-Savart law on the 3-sphere. Although we simply modified the Euclidean Biot-Savart law as an approximation to this, we found the same qualitative behavior from the 3-sphere Biot-Savart law, that having our vortices aligned with the Hopf velocity, yielded a nonlocal field also parallel with the Hopf velocity. We chose to do so to present a new practical approach to the open-orbit problem with the periodic cube, the equivalent of choosing new boundary conditions. However, the fact that we still agree qualitatively with the 3-sphere Biot-Savart integral is reassurance that our results would be similar had we chosen differently.

Others have also viewed superfluid turbulence systems with added rotation. Swanson et al. (1983) performed the first experiment including a combination of rotation and counterflow. Several attempts at numerically simulating this system have followed (Araki et al., 2003, Tsubota et al., 2003, 2004). These studies find a range of driving velocities, $v_{c1} < v_{ns} < v_{c2}$, and rotation, Ω , where vortices align with $\hat{v}_{ns} = \hat{z}$: polarized turbulence. The lower critical velocity matches the Donnelly-Glaberson in-

stability. For a given Ω , this velocity is given by $v_{DG} = 2(2\Omega\beta)^{1/2}$. Physically, Kelvin waves of a specific wave number and phase velocity match the driving velocity at v_{DG} , which allows an efficient transfer of energy into them. Above the higher critical velocity, turbulence becomes unpolarized and shows the $\langle L \rangle \propto v_{ns}^2$ behavior characteristic of homogeneous turbulence. Figure 5.1 (a) shows the polarization from Tsubota et al. (2003) for an example trial using a cubic system with only one pair of periodic boundaries. Figure 5.1 (b) shows this polarization, using the Hopf velocity field on the 3-sphere.

Turbulence on the 3-sphere is significantly more polarized than with rotating counterflow in the partially-periodic system in Tsubota et al. (2003). Typical values for the polarization with rotating counterflow vary from 0.2 to 0.7, with the example in Figure 5.1 (a) being quite common. In this system, the driving velocity and rotation rate are independent. Rotation on the 3-sphere comes from the curl of the velocity field. We can attempt to compare these two situations, however.

An analogous Ω on the 3-sphere could be given by $\text{curl}(\vec{v}_{ns})/2$. On the 3-sphere, $\text{curl}(\vec{v}_{ns}) = 2\vec{v}_{ns}/r_0$, which gives v_{DG} values ranging from 1.25 to 2.9 cm/s, corresponding to v_{ns} values of 1 to 6 cm/s, from Figure 4.16 on page 116. While these ranges overlap, we should not expect to see a transition, and indeed Figure 4.16 shows none visible. The simple fact that our velocity field, and thus our rotation, is comprised only of the normal fluid component obviously changes the dynamics. Kelvin waves cannot absorb energy efficiently by the normal fluid driving velocity matching their phase velocities. Instead of this mechanism behind the Donnelly-Glaberson instability, we still find perturbations causing vortices to grow and reconnect, as de-

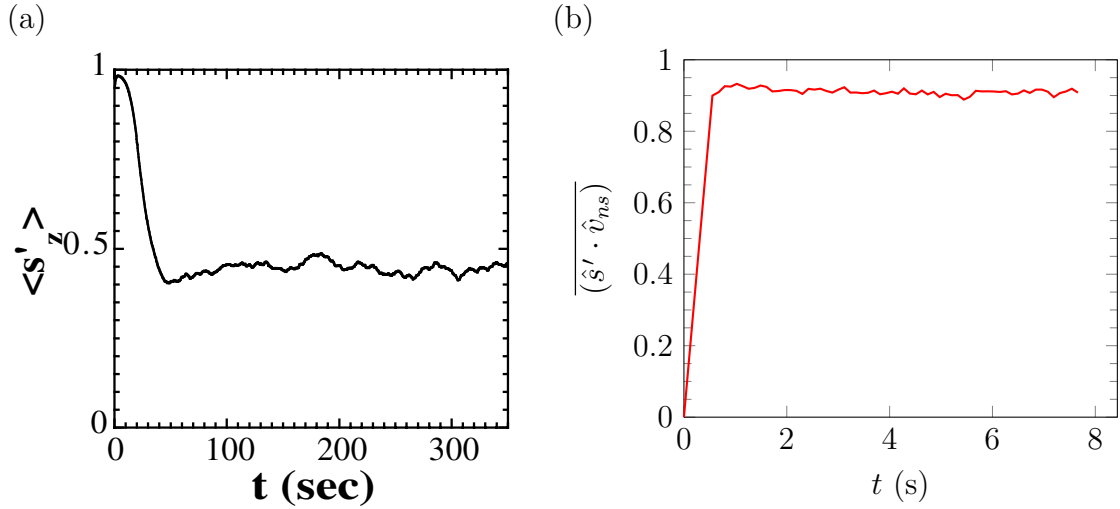


Figure 5.1: Comparison of the vortex polarization along the driving velocity for ${}^4\text{He}$ superfluid turbulence using different rotational systems, both at $T = 1.6$ K. Part (a) gives an example trial from [Tsubota et al. \(2003\)](#) using a rotating counterflow in a cube with one periodic boundary, with $v_{ns} = 0.08$ cm/s and $\Omega = 4.98 \cdot 10^{-2}$ rad/s. Part (b) gives an example trial from the present work on S^3 , using the Hopf velocity, with $v_{ns} = 1.8$ cm/s.

scribed in Section 4.4.4. Additionally, the Hopf velocity is uniform in magnitude, containing no stagnation points. These facts should lead us to expect polarization in our 3-sphere simulations to vary significantly from that of the rotating counterflow. Despite the greater degree of polarization in our system, however, there is still a significant degree of interaction. Indeed, the vortex reconnection rate, shown in Figure 4.12 on page 111, is consistent with predictions for polarized turbulence ([Barenghi and Samuels, 2004](#)).

In a way, 3-sphere turbulence is similar to the pathological open-orbit state on the periodic cube. Once open-orbit vortices form, if they do not reconnect, they tend to straighten under the friction term of the vortex equation of motion. Viewing the periodic cube in an extended zone scheme shows these open-orbit vortices are, effectively, infinitely long. This is the same as great circles on the 3-sphere. One difference between the two systems is that adding nonlocal interaction prevents such a state from forming in the periodic cube, but does not with the 3-sphere. It is conceivable that some initial conditions could start with a dense system of vortices on a small enough scale to mimic periodic boundaries better. But this is likely to only be temporary given the consistency with which this polarized state formed. Our initial vortices polarize very rapidly, as shown in Figure 5.1 (b). The other primary difference is that 3-sphere turbulence, like other polarized turbulence, is sustainable. However, the open-orbit state in the periodic cube degenerates into arrays of perfectly straight vortices. Despite the favorable topology of the 3-sphere, it is no alternative to the periodic cube for modeling homogeneous turbulence. Nevertheless, it does provide an excellent example of highly-polarized turbulence.

5.3 References

- Adachi, H., Fujiyama, S., and Tsubota, M. *Physical Review B*, **81**, 1 (2010).
- Araki, T., Tsubota, M., and Barenghi, C. F. *Physica B*, **329-333**, 226 (2003).
- Barenghi, C. and Samuels, D. *Journal of Low Temperature Physics*, **136**, 281 (2004).
- Swanson, C. E., Barenghi, C. F., and Donnelly, R. J. *Physical Review Letters*, **50**, 190 (1983).
- Tsubota, M., Araki, T., and Barenghi, C. F. *Physical Review Letters*, **90**, 205301 (2003).
- Tsubota, M., Barenghi, C. F., Araki, T., and Mitani, A. *Physical Review B*, **69**, 134515 (2004).

Appendix A

Biot-Savart Law

A.1 Derivation of the Biot-Savart Law for \vec{v}_s

Starting from the fact that the superfluid is incompressible, $\nabla \cdot \vec{v}_s = 0$, we wish to derive an equation for \vec{v}_s in terms of the vortex configuration, which will take the form of the Biot-Savart Law.

Any vector field that can be written as the curl of another, is divergenceless. So we can define the vector potential,

$$\vec{v}_s = \nabla \times \vec{A}. \quad (\text{A.1})$$

The vorticity vector is given by the curl of the velocity field, so:

$$\begin{aligned} \vec{\omega} &= \nabla \times (\nabla \times \vec{A}) = \nabla(\nabla \cdot \vec{A}) - \nabla^2 \vec{A} \\ \vec{\omega} &= -\nabla^2 \vec{A}, \end{aligned} \quad (\text{A.2})$$

where the final line follows from our choice of gauge, $\nabla \cdot \vec{A} = 0$. We are left with a

set of Poisson's Equations, one along each vector component. The Green's function solution, found in Section A.2, is given by:

$$\vec{A}(\vec{r}) = \frac{1}{4\pi} \int_{\mathcal{V}} \frac{\vec{\omega}(\vec{s}')}{|\vec{r} - \vec{s}'|} d\tau'.$$

It is sometimes helpful to realize that $\vec{\omega}$ is a vector field that is zero everywhere except at the locations along the vortex filament. To make this distinction, \vec{r} is the position vector in all space, \vec{s} signifies the position along a vortex core, and \vec{s}' is given a prime to indicate that it's an integration variable. If we look at the integrand:

$$\begin{aligned} d\vec{A} &= \frac{1}{4\pi} \frac{\vec{\omega}(\vec{s}') d\tau'}{|\vec{r} - \vec{s}'|} \\ &= \frac{1}{4\pi} \frac{\vec{\omega}(\vec{s}') d\vec{S}' \cdot d\vec{l}'}{|\vec{r} - \vec{s}'|}, \end{aligned} \quad (\text{A.3})$$

where $d\vec{l}'$ is the incremental direction pointing along the vorticity vector, $\vec{\omega}(\vec{s}')$, and $d\vec{S}'$ is the arbitrary area drawn around the vortex filament, through which $\vec{\omega}(\vec{s}')$ passes.

Recall the circulation Γ , from Equation 1.3:

$$\begin{aligned} \Gamma &= \oint \vec{v}_s \cdot d\vec{l} \\ &= \int \nabla \times \vec{v}_s \cdot d\vec{S} \\ d\Gamma &= \vec{\omega} \cdot d\vec{S}. \end{aligned}$$

We can make this substitution into Equation A.3, simplifying it while we manipulate

terms. If we rewrite our vector potential integrand, $d\vec{A}$ using triple product rule:

$$\vec{B}(\vec{A} \cdot \vec{C}) = \vec{C}(\vec{A} \cdot \vec{B}) + \vec{A} \times (\vec{B} \times \vec{C}),$$

$$\begin{aligned}\vec{\omega}(d\vec{S}' \cdot d\vec{l}') &= d\vec{l}'(\vec{\omega} \cdot d\vec{S}') + d\vec{S}' \times (\vec{\omega} \times d\vec{l}') \\ \vec{\omega} \times d\vec{l}' &= 0 \\ \vec{\omega}(d\vec{S}' \cdot d\vec{l}') &= d\vec{l}' d\Gamma \\ \Rightarrow d\vec{A} &= \frac{1}{4\pi} \frac{d\Gamma d\vec{l}'}{|\vec{r} - \vec{s}'|}\end{aligned}\tag{A.4}$$

Take the curl of Equation A.4 with respect to \vec{r} to find $d\vec{v}_s$, using the relation:

$$\nabla \times (f\vec{A}) = f(\nabla \times \vec{A}) - \vec{A} \times (\nabla f).$$

$$\begin{aligned}d\vec{v}_s &= \frac{1}{4\pi} \nabla \times \left(\frac{d\Gamma}{|\vec{r} - \vec{s}'|} d\vec{l}' \right) \\ &= \frac{1}{4\pi} \left[\frac{d\Gamma}{|\vec{r} - \vec{s}'|} (\nabla \times d\vec{l}') - d\vec{l}' \times \left(\nabla \frac{d\Gamma}{|\vec{r} - \vec{s}'|} \right) \right] \\ &= -\frac{1}{4\pi} d\Gamma d\vec{l}' \times \left(\nabla \frac{1}{|\vec{r} - \vec{s}'|} \right),\end{aligned}\tag{A.5}$$

where the last line follows because ∇ is a derivative with respect to \vec{r} , while $d\vec{l}'$ and $d\Gamma$ exist at \vec{s}' . The skeptical reader may question whether it is valid to say that $d\vec{v}_s = \nabla \times d\vec{A}$, so, whether it is valid to take the curl of the integrand rather than the resulting integral. This is also explained by recognizing that, $\nabla = \nabla(\vec{r})$. So, had we used the full integral, this operation can pass inside of it. In effect, doing it this way just allowed us to drop the integral sign for much of the derivation.

Now, using the relation $\nabla(1/|\vec{r} - \vec{s}'|) = -(\vec{r} - \vec{s}')/|\vec{r} - \vec{s}'|^3$, we can solve this part

to find $d\vec{v}_s$.

$$\begin{aligned} d\vec{v}_s &= \frac{1}{4\pi} \frac{d\Gamma}{|\vec{r} - \vec{s}'|^3} d\vec{l}' \times (\vec{r} - \vec{s}') \\ d\Gamma &= \vec{\omega} \cdot d\vec{S}' \\ d\vec{v}_s &= \frac{1}{4\pi} \frac{(\vec{\omega} \cdot d\vec{S}') d\vec{l}' \times (\vec{r} - \vec{s}')}{|\vec{r} - \vec{s}'|^3} \end{aligned} \quad (\text{A.6})$$

Now integrate over our volume, $d\tau'$. In the process, recognize that the vorticity is confined to the vortex filament, so we can choose the for dS' such that $dS' = \pi a_0^2$, and $a_0 \ll |\vec{r} - \vec{s}'|$. This implies that the surface integral has little effect on the integral along the vortex line, so can be separated, yielding:

$$\vec{v}_s(\vec{r}) = \frac{1}{4\pi} \int \vec{\omega} \cdot d\vec{S}' \int \frac{(\vec{s}' - \vec{r}) \times d\vec{l}'}{|\vec{s}' - \vec{r}|^3}$$

The integral over $d\vec{S}'$, for an isolated vortex in He II, yields the quantum of circulation: $\kappa = h/m_4$:

$$\vec{v}_s(\vec{r}) = \frac{\kappa}{4\pi} \int \frac{(\vec{s}' - \vec{r}) \times d\vec{l}'}{|\vec{s}' - \vec{r}|^3} \quad (\text{A.7})$$

The result gives the superfluid velocity field in all space, \vec{r} , from the Biot-Savart law for isolated vortices in He II.

A.2 Green's Function Solution to Poisson's Equation

Poisson's Equation is given by:

$$\nabla^2 y(\vec{r}) = -f(\vec{r}) \quad (\text{A.8})$$

We can compare Poisson's equation to the general form for the Green's function solution. Given some differential equation, with linear operator, $\mathcal{L} = \mathcal{L}(\vec{r})$:

$$\begin{aligned} \mathcal{L}y(\vec{r}) &= f(\vec{r}) \\ y(\vec{r}) &= \int G(\vec{r} - \vec{r}') f(\vec{r}') d^3 r' \end{aligned} \quad (\text{A.9})$$

$$\mathcal{L}(\vec{r})G(\vec{r} - \vec{r}') = \delta(\vec{r} - \vec{r}'). \quad (\text{A.10})$$

Equation A.9 is the general solution to a Green's function equation, which requires finding the form of $G(\vec{r} - \vec{r}')$. Equation A.10 is the key to finding $G(\vec{r} - \vec{r}')$ for particular forms of $\mathcal{L}(\vec{r})$. For the Poisson Equation: $\mathcal{L}(\vec{r}) = -\nabla^2$, and $f(\vec{r}')$ in Equation A.9 is the same $f(\vec{r})$ from Equation A.8 (written in terms of the integration variable \vec{r}'). We need to solve for $y(\vec{r})$. According to Equation A.9, we need to find $G(\vec{r} - \vec{r}')$, for the Poisson differential operator. We have already come across it in

Electricity and Magnetism:

$$\begin{aligned}
 -\nabla^2 \left(\frac{1}{4\pi|\vec{r} - \vec{r}'|} \right) &= \delta(\vec{r} - \vec{r}') \\
 \mathcal{L}G(\vec{r} - \vec{r}') &= \delta(\vec{r} - \vec{r}') \\
 G(\vec{r} - \vec{r}') &= \frac{1}{4\pi|\vec{r} - \vec{r}'|}.
 \end{aligned} \tag{A.11}$$

Now, we simply insert Equation A.11 into Equation A.9 to get the Green's Function solution to Poisson's Equation:

$$y(\vec{r}) = \frac{1}{4\pi} \int \frac{f(\vec{r}') d^3 r'}{|\vec{r} - \vec{r}'|}. \tag{A.12}$$

Appendix B

Kelvin's Theorem and Vortex Motion

B.1 Kelvin's Theorem

Kelvin's theorem states that the circulation in an ideal fluid is conserved (Guyon et al., 1991):

$$\frac{d\Gamma}{dt} = \frac{d}{dt} \oint_C \vec{v}_s \cdot d\vec{l} = 0. \quad (\text{B.1})$$

To show that this is true, it is important to state our assumptions up front. So we will start with a rather general equation of motion for fluid particles, the Navier-Stokes Equation:

$$\rho \frac{d\vec{v}}{dt} = \vec{f} - \nabla p + \eta \nabla^2 \vec{v}. \quad (\text{B.2})$$

Here, ρ is the fluid density, and \vec{f} represents the net body force per unit volume acting on our fluid particle (as opposed to contact forces from neighboring fluid particles). Gravity would be included in this term. p is the pressure, η is the viscosity, and

the last term represents the friction or shear forces acting on the fluid particle. This equation already includes several assumptions, such as that the fluid is isotropic, that there is the particular relation for the shear forces above, and that the fluid is incompressible, so ρ is constant.

To reduce this to an ideal fluid, we need only make the added assumptions that there is no viscosity, $\eta = 0$, and that any body forces are conservative, so $\vec{f} = -\nabla\phi$. Our equation of motion, a slight modification of Euler's Equation, is now given by:

$$\frac{d\vec{v}}{dt} = -\frac{1}{\rho}\nabla(p + \phi) \quad (\text{B.3})$$

Now, to demonstrate that Kelvin's Theorem applies under these conditions, we apply the time derivative to the integral, and show that this does, in fact, equal zero. For clarity I will write our infinitesimal integration vector as $\vec{\delta l}$.

$$\frac{d\Gamma}{dt} = \oint_{\mathcal{C}} \frac{d\vec{v}}{dt} \cdot \vec{\delta l} + \oint_{\mathcal{C}} \vec{v} \cdot \frac{d(\vec{\delta l})}{dt} \quad (\text{B.4})$$

The first term is easy; we will eventually plug in Equation B.3. But the second term will take some analysis. Consider the arbitrary contour, \mathcal{C} , that we are integrating around, in Figure B.1. We need to allow this contour to move in time.

Relating the two pairs of vectors we have:

$$\frac{d(\vec{\delta l})}{dt} = \vec{v}(\vec{r} + \vec{\delta l}, t) - \vec{v}(\vec{r}, t) \approx (\vec{\delta l} \cdot \nabla)\vec{v},$$

which in the limit that $\vec{\delta l}$ goes to zero, is exact. We now insert everything into

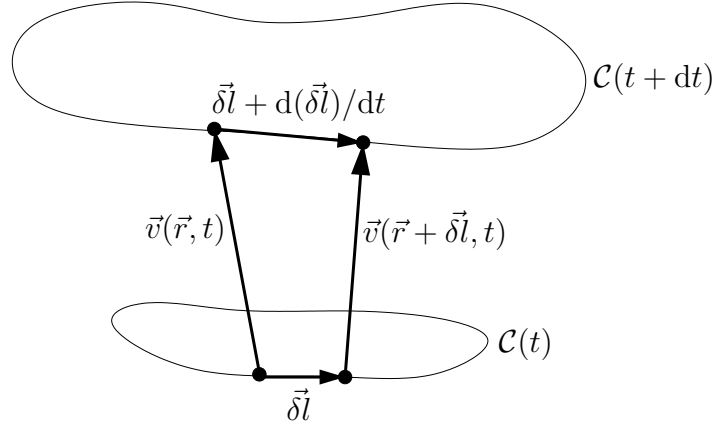


Figure B.1: Arbitrary contour of integration

Equation B.4, and recognize that: $(\nabla \vec{v}) \cdot \vec{v} = \nabla v^2 / 2$.

$$\frac{d\Gamma}{dt} = -\frac{1}{\rho} \left[\oint_C \nabla(p + \phi) \cdot \vec{\delta l} - \oint_C \nabla \frac{\rho v^2}{2} \cdot \vec{\delta l} \right] = 0 \quad (\text{B.5})$$

The integral of these continuous gradient fields around a closed contour must be zero. Kelvin's Theorem is proved.

B.2 Vortices Move with Ideal Fluid Velocity

To show that Equation B.1 means vortices in an ideal fluid move with the local superfluid velocity, let us imagine an arbitrary superfluid vortex drawn in Figure B.2 with a surrounding surface of fluid particles as an imaginary boundary. Insert a contour \mathcal{C} , which we will fix to the fluid particles themselves, such that it moves with the local superfluid velocity. Initially, no part of the vortex is perpendicular to the area bounded by \mathcal{C} . In fact, our vorticity is confined within our bounding surface

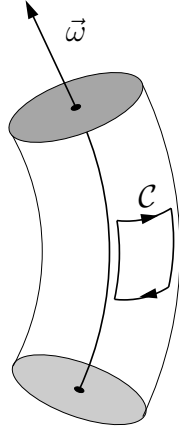


Figure B.2: Superfluid vortex filament

such that $\vec{\omega}$ is zero at the surface.

If we rewrite Kelvin's Theorem:

$$\frac{d\Gamma}{dt} = \frac{d}{dt} \int_{\mathcal{S}} \vec{\omega} \cdot d\vec{S} = 0. \quad (\text{B.6})$$

Notice that, in its initial configuration, the integral itself is zero because $\vec{\omega}$ within \mathcal{S} is zero. Now apply an arbitrary \vec{v}_s . We defined the contour such that it moves with this local superfluid velocity. But since the applied velocity is arbitrary, unless the vortex also moves with the local superfluid velocity, our integral could become nonzero, which would violate Kelvin's theorem. Therefore, in an ideal fluid, a vortex filament must move with the local \vec{v}_s .

Appendix C

Parametric Curves

If \vec{s} gives the position vector of points along a curve, we can parametrize this curve by some generic dimensionless parameter, λ . The length between two points along the curve comes from summing the lengths of the sides of a polygon inscribed along a curve. Then we take the limit as the number of sides of the polygon goes to infinity. The arc length, ξ , makes a convenient parameter for use in numerical derivatives ([Stewart, 2001](#)):

$$\xi(\lambda) = \int_a^\lambda |\vec{s}'(\lambda_*)| d\lambda_*, \quad (\text{C.1})$$

where the prime is the derivative with respect to the parameter, and we are considering our curve at a fixed time. The Fundamental Theorem of Calculus gives us:

$$\frac{d\xi}{d\lambda} = |\vec{s}'(\lambda)|. \quad (\text{C.2})$$

If we wish to reparametrize the position vector in terms of arclength, invert the function $\xi(\lambda) \rightarrow \lambda(\xi)$, yielding $\vec{s} = \vec{s}(\lambda(\xi))$.

C.1 Tangent Vector

We want to find a unit tangent vector to use to track our vortex configuration. For now, we will call this $\hat{T}(\lambda)$.

$$\hat{T}(\lambda) := \frac{\vec{s}'(\lambda)}{|\vec{s}'(\lambda)|}. \quad (\text{C.3})$$

But when we parametrize with arclength, we find that the derivative of $\vec{s}(\xi)$ has unit length:

$$\begin{aligned} \frac{d\xi}{d\lambda} &= |\vec{s}'(\lambda)| \\ \Rightarrow \hat{T}(\lambda) &= \frac{\vec{s}'(\lambda)}{|\vec{s}'(\lambda)|} \\ &= \frac{d\vec{s}/d\lambda}{d\xi/d\lambda} = \frac{d\vec{s}}{d\xi} \\ \rightarrow \left| \frac{d\vec{s}(\lambda(\xi))}{d\xi} \right| &= 1. \end{aligned}$$

So, parametrizing with the arclength means our unit tangent vector is just the first derivative of our position: $\hat{T} = \hat{s}'(\xi)$.

C.2 Curvature Vector

Another necessary quantity to define is the curvature vector.

$$\vec{k} := \frac{d\vec{T}}{d\xi} \quad (\text{C.4})$$

\vec{k} points toward the center of the osculating circle tangent to each point on the vortex. The circle's radius is given by the inverse of the magnitude of the curvature vector: $R = |\vec{k}|^{-1}$. Since \vec{k} points along the radius of the circle tangent to \hat{T} , the two vectors must be orthogonal.

Proof:

$$\vec{k} = \frac{d\hat{T}(\lambda(\xi))}{d\xi} = \frac{d\hat{T}(\lambda)/d\lambda}{d\xi/d\lambda} = \frac{\vec{T}'(\lambda)}{|\vec{s}'(\lambda)|}$$

$$|\hat{T}(\lambda)| = 1 \rightarrow \hat{T}(\lambda) \cdot \hat{T}(\lambda) = 1$$

(Taking the derivative)

$$\hat{T}(\lambda) \cdot \vec{T}'(\lambda) = 0$$

$$\hat{T}(\lambda) \cdot \vec{k} = 0 \quad \square$$

If we continue to use a generic parameter for our vortex, we get a complicated relation between the curvature vector and other spatial derivatives:

$$\vec{k} := \frac{d\hat{T}(\lambda(\xi))}{d\xi} = \frac{d^2\vec{s}}{d\lambda^2} \left| \frac{d\vec{s}}{d\lambda} \right|^{-2} - \frac{d\vec{s}}{d\lambda} \left(\frac{d\vec{s}}{d\lambda} \cdot \frac{d^2\vec{s}}{d\lambda^2} \right) \left| \frac{d\vec{s}}{d\lambda} \right|^{-4} \quad (\text{C.5})$$

Proof:

$$\begin{aligned}
\vec{k} &:= \frac{d\hat{T}(\lambda)}{d\xi} \\
&= \frac{d\lambda}{d\xi} \cdot \frac{d\hat{T}(\lambda)}{d\lambda} \\
&= |\vec{s}'(\lambda)|^{-1} \frac{d}{d\lambda} \left[\frac{\vec{s}'(\lambda)}{|\vec{s}'(\lambda)|} \right] \\
&= |\vec{s}'(\lambda)|^{-1} \left[\frac{d^2\vec{s}}{d\lambda^2} \left| \frac{d\vec{s}}{d\lambda} \right|^{-1} - \frac{1}{2} \frac{d\vec{s}}{d\lambda} \left(\frac{d^2\vec{s}}{d\lambda^2} \cdot \frac{d\vec{s}}{d\lambda} + \frac{d\vec{s}}{d\lambda} \cdot \frac{d^2\vec{s}}{d\lambda^2} \right) \left| \frac{d\vec{s}}{d\lambda} \right|^{-3} \right] \\
&= \frac{d^2\vec{s}}{d\lambda^2} \left| \frac{d\vec{s}}{d\lambda} \right|^{-2} - \frac{d\vec{s}}{d\lambda} \left(\frac{d\vec{s}}{d\lambda} \cdot \frac{d^2\vec{s}}{d\lambda^2} \right) \left| \frac{d\vec{s}}{d\lambda} \right|^{-4}
\end{aligned}$$

However, parametrizing with the arclength ($\lambda = \xi$) greatly simplifies this relation.

$$\begin{aligned}
\left| \frac{d\vec{s}}{d\xi} \right| = 1 &\Rightarrow \frac{d\vec{s}}{d\xi} \cdot \frac{d^2\vec{s}}{d\xi^2} = 0 \\
\Rightarrow \vec{k} &= \frac{d^2\vec{s}}{d\xi^2}
\end{aligned} \tag{C.6}$$

However, it is much simpler to show this if we use the arclength from the beginning:

$$\begin{aligned}
\hat{T} &= \hat{s}'(\xi) \\
\vec{k} &:= \frac{d\hat{T}}{d\xi} = \vec{s}''(\xi)
\end{aligned}$$

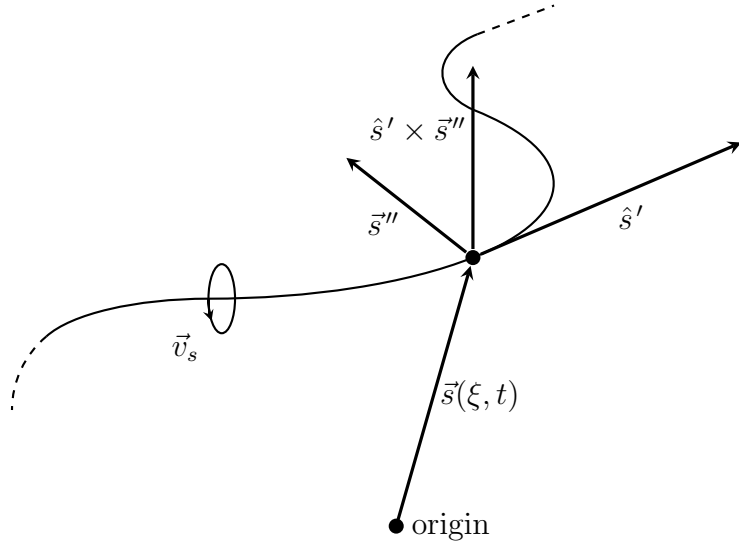


Figure C.1: Schematic of the relevant vectors involved in tracking vortex motion.

C.3 Binormal Vector

Lastly, the binormal vector is defined as such.

$$\hat{B}(\lambda) = \hat{T}(\lambda) \times \hat{k}(\lambda) \quad (\text{C.7})$$

Here, the unit vector, \hat{k} , is referred to as the normal vector. The local velocity, however, uses the unnormalized curvature vector in the relation $\vec{v}_{local} \propto \hat{s}' \times \vec{s}''$. For our simulations, we use $\hat{T} = \hat{s}'$, and $\vec{k} = \vec{s}''$ both parametrized by the arclength. Figure C.1 shows a picture of the relevant vectors.

Appendix D

Scaling in Homogeneous Superfluid Turbulence

Schwarz presented a dimensional analysis argument in his paper Schwarz (1982), which gave us several approximate equations for how quantities in a system of homogeneous superfluid turbulence scale with applied fluid velocity, v_{ns} . Following this, the argument in Schwarz (1982) was refined by Swanson and Donnelly (1985), and then reaffirmed in Schwarz (1988). I will focus, however, on the approximate argument applied to the average line length density, $\langle L \rangle$.

If we assume that $\langle L \rangle$, within some volume of our system, depends only on α , β , and the magnitude of our applied fluid velocity, v_{ns} , the dimensions of these quantities can determine their relation with $\langle L \rangle$. $\langle L \rangle$ has units of cm^{-2} , α is a unitless parameter which varies with temperature in the system, β has units of cm^2/s , and

of course, v_{ns} has cm/s .

$$\begin{aligned}\langle L \rangle &= f(\alpha) \beta^x v_{ns}^y \\ \left[\frac{1}{cm^2} \right] &= \left[\frac{cm^2}{s} \right]^x \left[\frac{cm}{s} \right]^y \\ \Rightarrow y &= -x = 2 \\ \langle L \rangle &= f(\alpha) \left(\frac{v_{ns}}{\beta} \right)^2 \\ \langle L \rangle &= \gamma^2 v_{ns}^2\end{aligned}$$

The final proportionality, is what Schwarz and others found through slightly different arguments. Note, that we assumed, not only that these quantities were all that $\langle L \rangle$ depended on, but we also assumed the form of their dependence. We might expect $\langle L \rangle$ to depend on the size of the system, D . Ignoring this is equivalent to considering the turbulence is homogeneous. We also assume $\langle L \rangle$ depends only on the magnitude of v_{ns} , not on the direction. This is true if our vortex tangle is isotropic. Schwarz, himself, points out this assumption [Schwarz \(1988, p. 2403\)](#), by giving an example of a system which may be homogeneous but is not isotropic: if straight vortices in a periodic cube lie within random planes perpendicular to \hat{v}_{ns} , and if those planes are separated greater than the reconnection distance, then line length will never increase regardless of the driving velocity. $\langle L \rangle$ would be independent of v_{ns} : proportional to $(v_{ns})^0$. This is also similar to an extreme version of the periodic boundaries problem. If open orbit vortices form, the equation of motion would tend

to shrink and, therefore, straighten them. Similarly, one could imagine if vortices line up tangent to the velocity field, $\langle L \rangle$ would also be independent of velocity. This is important for polarized turbulence.

Appendix E

Vortex Visualization on S^3

Any space that is greater than three dimensions is hard to visualize, and even our three dimensional surface, S^3 , is difficult due to its global structure. There are several mappings that have proven useful for visualizing the vortex tangle:

1. the stereographic projection,
2. hyperspherical coordinates, and
3. the Hopf projection (Hopf fibration).

However, we first begin with an exercise to help visualize the 3-sphere, itself.

E.1 Visualizing S^3

First, let us start with one dimension lower. We can imagine puncturing a 2-sphere at some point and flattening it out to form a circle. Figure E.1 shows a schematic of these two geometries. I will refer to it as a 2-ball, meaning the dimension of the area, or a 1-sphere meaning the dimension of the circumference. The antipode of the

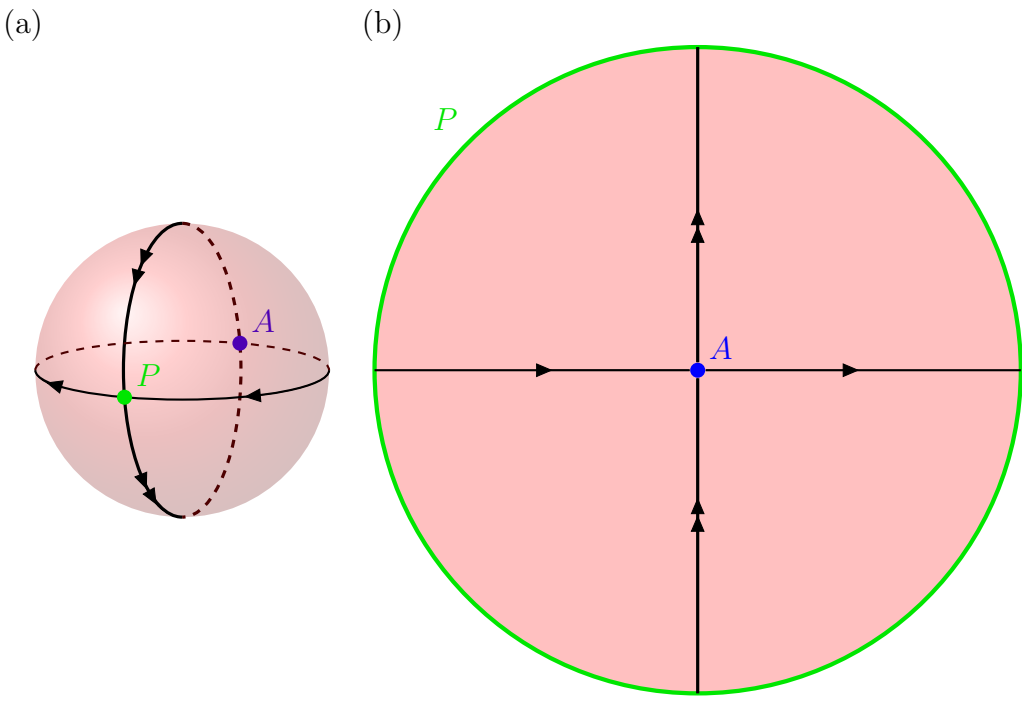


Figure E.1: Association between (a) a 2-sphere and (b) a 2-ball is shown. Point *P* in (a) is the puncture point and *A* is the antipode of *P*. The 2-sphere is considered infinitely stretchable so that *P* is stretched over the entire circumference of the circle in (b). The marked lines in each are paths traveling from *A* to *P* and back to *A*.

puncture point is now in the center of the circle, and the puncture point is spread out over the entire circumference. Distances on the 2-sphere are now distorted but this is purely an exercise in visualizing the space. Traveling along a great circle on the original, unpunctured 2-sphere is now the same as traveling along the radius of the 2-ball. When some object hits the circumference it reemerges at the point directly opposite and continues radially inward toward the center.

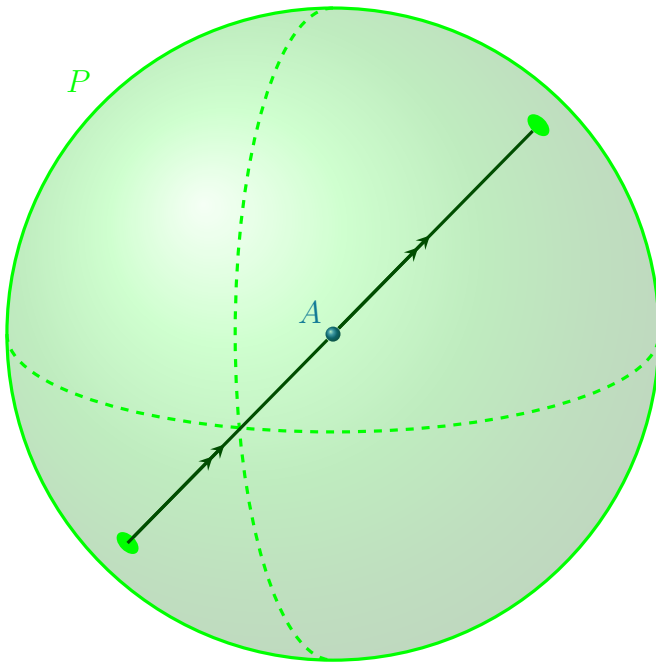


Figure E.2: 3-ball associated with a 3-sphere punctured at point P , which has its antipode point at A . The entire 2-sphere surface is associated with the puncture point P on the 3-sphere. The radial path marked with the double arrows, follows a great circle through points A and P on the associated 3-sphere.

We can imagine the same process in one dimension higher. Puncture a 3-sphere and stretch this point over the surface of a 3-ball. The center of this 3-ball will be the antipode of that point. Now, we can travel in any radial direction from the center of the 3-ball hit the 2-sphere boundary and reemerge radially opposite. Then we would travel radially inward back to our starting point at the center. We cannot draw the associated 3-sphere, however the 3-ball is shown in Figure E.2.

It is more common to see this exercise applied to the periodic cube, that is,

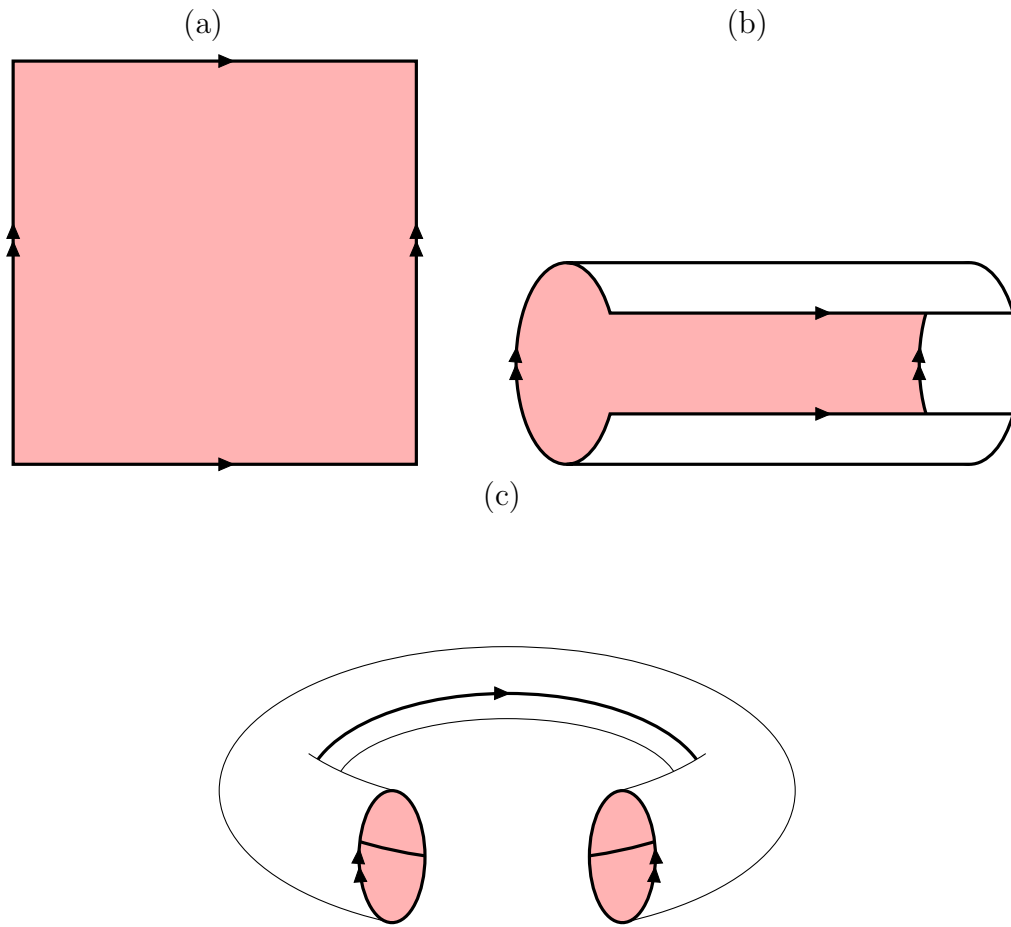


Figure E.3: The association between a periodic box and a 2-torus is shown.

the 3-torus. To show this analogous situation, let us look at a periodic square and identify two opposite sides. Like a piece of paper, we can curl this flat square so that two identified sides connect. Then curl in the perpendicular direction so the other two walls do, too. This is the association between the periodic square and the 2-torus, shown in Figure E.3. And just like before, we could do a similar process with the periodic cube.

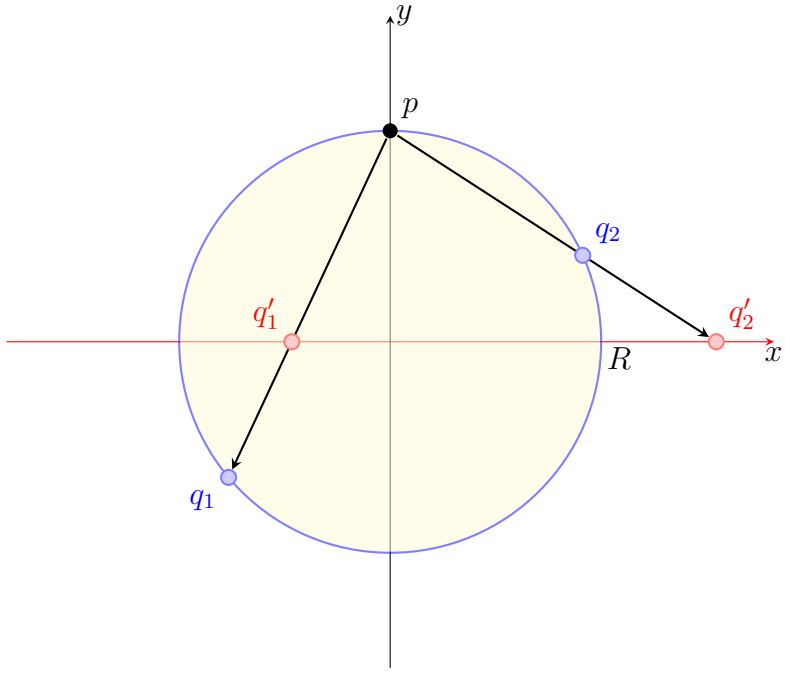


Figure E.4: Stereographic projection: mapping a 1-sphere (circle) of radius R to the x -axis. The projection point is p and two example points in the mapping are shown: $f : q_1 \mapsto q'_1$, and $f : q_2 \mapsto q'_2$.

E.2 Stereographic Projection

The stereographic projection takes points on an n -sphere and maps them onto \mathbb{R}^n . It is easiest to visualize the ($n < 3$)-sphere when embedded in \mathbb{R}^{n+1} . We shall start with $n = 1$, a circle.

Figure E.4 shows the stereographic projection of a circle of radius R , for two example points in the mapping. A line is extended from the projection point, p , through every point on the circle and the intersection between the line and the

x -axis gives the image point. Note that mapping of the projection point itself is undefined. Otherwise, it would be mapped to $\pm\infty$. And as you can see, as the point on the circle nears the projection point, its image on the line approaches infinity, so this mapping cannot preserve line length on the circle. For all points on the circle other than the projection point, the map is bijective (one-to-one). It is not hard to show that the equation for this stereographic projection is given by:

$$x' = \frac{x}{1 - y/R}, \quad (\text{E.1})$$

where x' denotes the image coordinate located on the x -axis.

For a 2-sphere in an embedding space of 3 dimensions, the stereographic projection is illustrated in Figure E.5.

Similar to the 1-sphere, the 2-sphere stereographic projection, with projection point, p , located at $z = R$ and mapping to the xy -plane, has the equation:

$$(x', y') = \left(\frac{x}{1 - z/R}, \frac{y}{1 - z/R} \right), \quad (\text{E.2})$$

where, again, the prime indicates the image coordinates in the xy -plane.

We can take this one step further to our 3-sphere system, with the projection point, p , found at $w = R$ and mapping to the 3-plane $w = 0$. The equation extends naturally:

$$(x', y', z') = \left(\frac{x}{1 - w/R}, \frac{y}{1 - w/R}, \frac{z}{1 - w/R} \right). \quad (\text{E.3})$$

The stereographic projection seems like exactly what we want. We have a 3-sphere

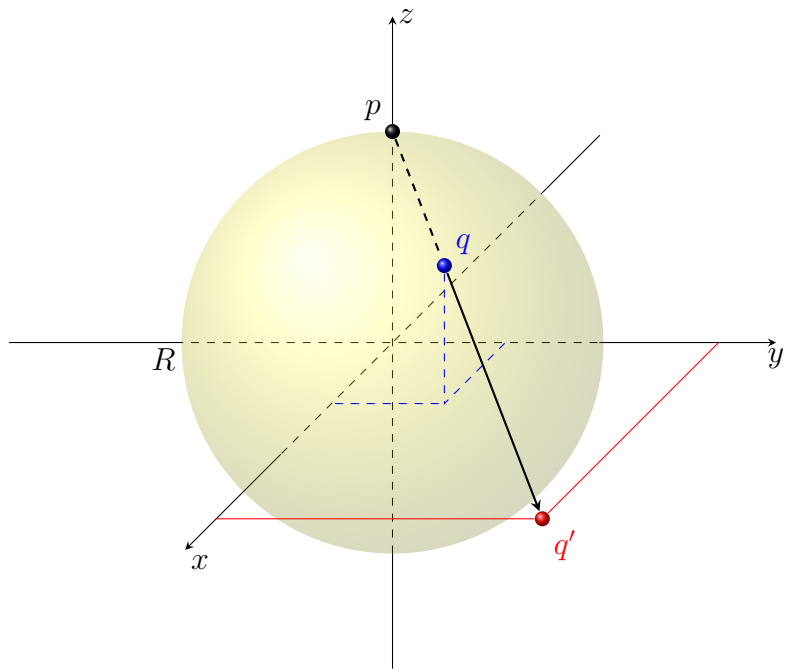


Figure E.5: Stereographic projection: mapping a 2-sphere of radius R to the xy -plane. The projection point is p and the example mapping shown is: $f : q \mapsto q'$.

and we want it to be flat for visualizing. This does exactly that. Although we do not prove it here, stereographic projections also have the benefit that circles on the initial n -sphere still appear as circles when projected (some with infinite radius) (Lyons, 2003). But some of the properties of this map are less than desirable. I already mentioned that length is not preserved under this map. By looking at Figures E.4 and E.5, the far (from p) half of the 2-sphere is projected inside the radius R equator of the 2-plane, and the near half is projected outside of it. Vortices on the side of the 3-sphere nearest the projection point, will be enlarged. Our next visualization method does not suffer from this problem.

E.3 Hyperspherical Coordinates

Hyperspherical coordinates may be the first, most natural idea for visualizing our 3-sphere. By analogy, simply take the (θ, ϕ) of a 2-sphere and add an extra angle: (θ, ϕ, ψ) . The ordering of our coordinate system does not matter, just that we are consistent. We are used to seeing the mapping from spherical coordinates to cartesian coordinates but what we need is the inverse of this:

$$\theta = \text{acot} \left(\frac{x}{\sqrt{w^2 + z^2 + y^2}} \right), \quad (\text{E.4})$$

$$\phi = \text{acot} \left(\frac{y}{\sqrt{w^2 + z^2}} \right), \quad (\text{E.5})$$

$$\psi = 2 \text{acot} \left(\frac{\sqrt{w^2 + z^2} + z}{w} \right). \quad (\text{E.6})$$

Here, the θ , and ϕ coordinates have a range of π , and ψ has a range of 2π . $\psi = \text{acot}(z/w)$ is too small by an additive constant π when $w < 0$, which is why this inverse function is used. There are several stipulations for dealing with when the various coordinates equal zero. Note that different programming languages have different definitions for their inverse trigonometric functions. Unlike the codomain of the stereographic projection, hyperspherical coordinates have a finite range. But our last mapping proves to be even more useful, by taking advantage of properties of our choice of driving velocity.

E.4 Hopf Fibration

The Hopf fibration is a mapping, which takes parallel great circles on S^3 to distinct points on S^2 . These great circles lie tangent to the Hopf velocity field, $v = (-y, x, -w, z)$, which we use as our driving velocity, which makes it specially suited for demonstrating the behavior of our vortex tangle. The term Hopf fibration is used to refer to this mapping as a whole and the term Hopf fibers refers to the great circles on S^3 which are the preimages of points on S^2 under this mapping.

The Hopf fibration is constructed by viewing the embedding space for our 3-sphere, \mathbb{R}^4 , as the direct product of two complex subspaces, \mathbb{C}^2 . Explicitly, if our \mathbb{R}^4 coordinates are (x, y, z, w) , set $q_1 = x + iy$, and $q_2 = z + iw$. Then the Hopf fibration is given by:

$$h(q_1, q_2) = (2q_1q_2^*, |q_1|^2 - |q_2|^2), \quad (\text{E.7})$$

where z^* is the complex conjugate and $|...|^2$ denotes the conjugate square. Note that

the first component of the projected system, $2q_1q_2^*$, is complex. So from this, we get the three coordinates of the embedding space of the 2-sphere that this projection maps to. Namely:

$$h_1 = \operatorname{Re}(2q_1q_2^*) = 2(xz + yw), \quad (\text{E.8})$$

$$h_2 = \operatorname{Im}(2q_1q_2^*) = 2(yz - xw), \quad (\text{E.9})$$

$$\begin{aligned} h_3 &= |q_1|^2 - |q_2|^2 = (x^2 + y^2) - (z^2 + w^2) \\ &= (x + z)(x - z) + (y + w)(y - w). \end{aligned} \quad (\text{E.10})$$

The final coordinate, h_3 , is more numerically stable if it is written in the factored form, given above. It is quite easy to demonstrate that, if our original \mathbb{R}^4 coordinates lie on a 3-sphere of radius r_0 , our image points lie on a 2-sphere of radius r_0^2 . This is all that is needed to show that the Hopf fibration maps $S^3 \rightarrow S^2$.

$$\begin{aligned} h_1^2 + h_2^2 + h_3^2 &= (2q_1q_2^*)(2q_1q_2^*)^* + (|q_1|^2 - |q_2|^2)^2 \\ &= 4|q_1|^2|q_2|^2 + (|q_1|^4 + |q_2|^4 - 2|q_1|^2|q_2|^2) \\ &= (|q_1|^2 + |q_2|^2)^2 \\ &= (x^2 + y^2 + z^2 + w^2)^2 = r_0^4 \end{aligned} \quad (\text{E.11})$$

Hopf demonstrated that this mapping takes great circles on S^3 to points, (h_1, h_2, h_3) , on S^2 (Gluck and Warner, 1983). To see this, we can define another quantity on S^2 as the stereographic projection from the point h_3 onto the plane through the equator.

$$q = \frac{h_1 + ih_2}{1 - h_3} \quad (\text{E.12})$$

This is equivalent to Equation E.2 for a unit 2-sphere, if our projected coordinates are complex. Substituting the definitions of q_1 and q_2 :

$$\begin{aligned} q &= \frac{2q_1 q_2^*}{1 - (|q_1|^2 - |q_2|^2)} \\ &= \frac{2q_1 q_2^*}{2|q_2|^2} \\ &= \frac{q_1}{q_2} \\ &= \frac{x + iy}{z + iw}. \end{aligned} \quad (\text{E.13})$$

Now we set q in Equations E.12 and E.13 equal to each other. The real and imaginary parts give us a system of two simultaneous equations:

$$(1 - h_3)x - h_1z + h_2w = 0, \quad (\text{E.14})$$

$$(1 - h_3)y - h_2z - h_1w = 0. \quad (\text{E.15})$$

If we select h_1 , h_2 , and h_3 as fixed parameters, and x , y , z , and w as variables, these equations represent the intersection of 3-planes through the origin in \mathbb{R}^4 . Explicitly, the first and second equations give the normal vectors to these 3-planes as $(1 - h_3, 0, -h_1, h_2)$ and $(0, 1 - h_3, -h_2, -h_1)$, respectively. Since they are distinct and intersect, they form a 2-plane. We are interested in the locus of points $x^2 + y^2 + z^2 + w^2 = 1$ that also lie on this 2-plane that passes through the origin. The intersection

of these form a great circle. In summary, for a specific image point $(h_1, h_2, h_3) \in S^2$, the Hopf fibration defines the equations of the 3-planes that intersect each other to make a 2-plane, which intersects the origin and the 3-sphere to make a great circle. Thus, the preimage of a point $(h_1, h_2, h_3) \in S^2$ is a great circle in S^3 (a Hopf fiber).

We have talked so far about the Hopf fibers of the 3-sphere but these are intimately connected with the vector field tangent to them, which we use as the driving velocity for our turbulence. If each Hopf fiber is parametrized, we can take the derivative with respect to this parameter to get the tangent vector along that flow line.

We previously associated two complex numbers with points in \mathbb{R}^4 : $q_1 = x + iy$, $q_2 = z + iw$, such that $\mathbb{R}^4 = \mathbb{C}^2$. The great circles on $S^3 \subset \mathbb{R}^4$ can be parametrized like we normally would a complex plane: with polar coordinates. We also need to scale the contributions from q_1 and q_2 as these great circles vary their orientations over the 3-sphere.

$$q_1 = x + iy = r_0 \cos \eta (\cos \theta + i \sin \theta),$$

$$q_2 = z + iw = r_0 \sin \eta (\cos \theta + i \sin \theta).$$

These relations are equivalent to the Hopf coordinates (used in Appendix F) with $\zeta_1 = \zeta_2 = \theta$. Our velocity field is simply the derivative with respect to θ , which if we write this back in our ordered set in \mathbb{R}^4 , becomes:

$$\vec{v} = (-y, x, -w, z). \quad (\text{E.16})$$

This is the velocity field we apply to our system. I will demonstrate some of its properties, in Appendix F.

But first, as a demonstration, Figure E.6 (a) shows 100 randomly generated initial points on a unit-radius S^3 that were then iterated in the direction of the Hopf velocity field and then mapped using the Hopf fibration, Equations E.8, E.9, and E.10. Each iteration along a Hopf fiber (flow line) is marked by a point and connected by a line. The fact that these points appear isolated and distinct, and the fact that you cannot see the lines connecting those on a single flow line, shows visually what we have been demonstrating throughout this appendix: the Hopf vector field lies tangent to great circles, which get mapped to single, distinct points on S^2 . A similar plot of the trajectories along great circles is shown in Figure E.6 (b) for comparison. It shows 15 randomly generated initial points on S^3 and the trajectories of each when iterated along the Hopf vector field, but this time they are stereographically projected.

Because of our choice of the Hopf vector field as our driving velocity, the Hopf fibration turns out to be a useful projection for visualizing the superfluid turbulent system. This mapping emphasizes the symmetry of our driving velocity. It allows us to see deviations of superfluid vortices from these great circle flow lines, which fill the S^3 volume.

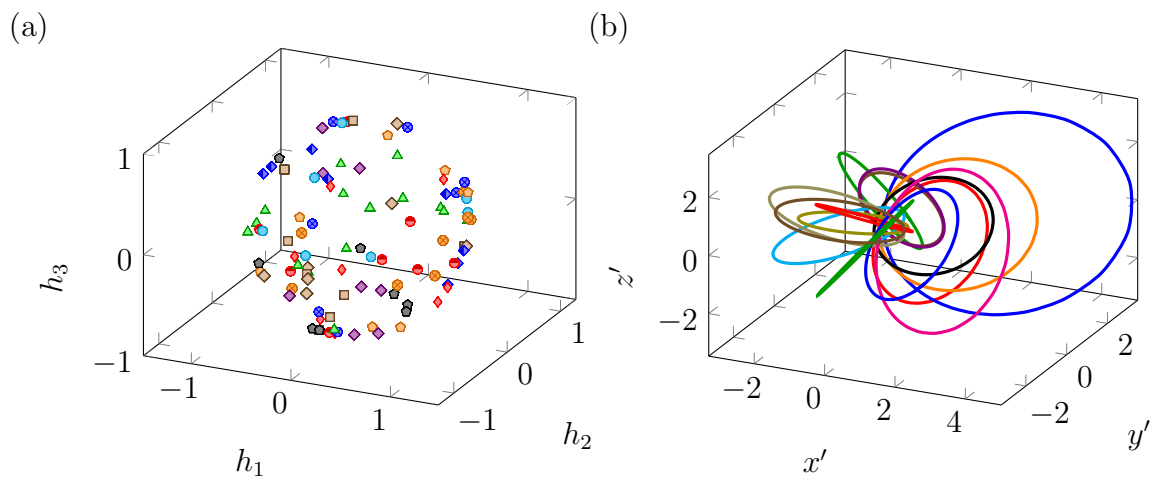


Figure E.6: The flow lines of the Hopf velocity field, $v = (-y, x, -w, z)$, starting from randomly-generated points on a unit-radius S^3 , and projected using (a) the Hopf fibration, and (b) the stereographic projection.

Appendix F

Hopf Velocity Field

From Appendix E.4, our choice of driving velocity is the Hopf vector field, given by Equation E.16:

$$\vec{v} = (-y, x, -w, z).$$

For any driving velocity for the system, we want several characteristics to be fulfilled. Some are more important than others. The driving velocity:

- must be tangent to our system, in this case, the surface S^3 . If not, we would be driving our vortices away out of our surface volume.
- should be uniform magnitude, so that our turbulence can be homogeneous.
- should be divergence-free, otherwise we would not be able to use the Biot-Savart law (see Appendix A).
- should be irrotational, if we wish to apply an average superfluid flow as our driving velocity. Since the applied superfluid velocity is an average fluid flow, and is separate from any velocity due to the vortex filaments, its curl should

be irrotational. If not, we need to use the normal fluid velocity to drive the system.

F.1 Hopf Velocity Properties

The first two criteria are easy to demonstrate. Since the generic vector in \mathbb{R}^4 is always perpendicular to the S^3 surface, when centered at the origin, we can take the \mathbb{R}^4 dot product with (x, y, z, w) to see if the Hopf vector field is indeed tangent to S^3 .

$$(-y, x, -w, z) \cdot (x, y, z, w) = -yx + xy - wz + zw = 0. \quad (\text{F.1})$$

Indeed, it is. Our most important criterion is met. The velocity field is also uniform magnitude: $y^2 + x^2 + w^2 + z^2 = r_0^2$. Check. But we still want to use the Biot-Savart law or else we have no means of comparing to turbulence in \mathbb{R}^3 .

In \mathbb{R}^4 , we can certainly take the divergence of our vector field.

$$\nabla \cdot \vec{v} = -\frac{\partial y}{\partial x} + \frac{\partial x}{\partial y} - \frac{\partial w}{\partial z} + \frac{\partial z}{\partial w} = 0. \quad (\text{F.2})$$

Again, at least in \mathbb{R}^4 , our vector field is divergenceless. Restricting ourselves to the curved, S^3 surface adds a degree of difficulty. To give the answer, [DeTurck and Gluck \(2004, p. 10-11\)](#) state that left-invariant and right-invariant vector fields on S^3 are tangent to parallel great circles on S^3 and are, thus, divergence-free. We know that the Hopf vector field is tangent to great circles but we have not shown that those great circles are parallel. To do this we can show that our Hopf vector

field is right-invariant, which according to DeTurck and Gluck (2004) shows it is divergence-free.

Left and right-invariance refers to quaternion multiplication. For convenience, quaternion multiplication is just a matter of distributing over its components and keeping the following rules in mind:

$$ijk = -1, \quad (\text{F.3})$$

$$i^2 = j^2 = k^2 = -1. \quad (\text{F.4})$$

From these, one can derive the following multiplication table:

q	1	i	j	k
1	1	i	j	k
i	i	-1	k	-j
j	j	-k	-1	i
k	k	j	-i	-1

If we associate \mathbb{R}^4 with the quaternion structure, a generic point $\vec{r} = (x, y, z, w)$ becomes $r = x + yi + zj + wk$ and our vector field becomes $v = -y + xi - wj + zk$. A right-invariant vector field obeys the property, $v(rq) = v(r)q$, while a left-invariant vector field obeys the similar property, $v(qr) = qv(r)$, for the generic quaternion $q = a + bi + cj + dk$.

To show that the Hopf field is right-invariant, rq is given by:

$$rq = (xa - yb - zc - wd) + (ya + xb - wc + zd)i + \\ (za + wb + xc - yd)j + (wa - zb + yc + xd)k.$$

The function $v(r)$ is a map from $(x + yi + zj + wk)$ to $(-y + xi - wj + zk)$. So, we find for $v(rq)$:

$$v(rq) = -(ya + xb - wc + zd) + (xa - yb - zc - wd)i \\ - (wa - zb + yc + xd)j + (za + wb + xc - yd)k. \quad (\text{F.5})$$

Now, we just need to compare this to $v(r)q = (-y + xi - wj + zk)q$:

$$v(r)q = (-ya - xb + wc - zd) + (xa - yb - zc - wd)i + \\ (-wa + zb - yc - xd)j + (za + wb + xc - yd)k. \quad (\text{F.6})$$

The two Equations F.5 and F.6 are identical. The Hopf vector field from Equation E.16 is a right-invariant vector field. We have, then, that the Hopf field is divergenceless. So it has met the first three of four criteria for use as our driving velocity.

DeTurck and Gluck (2004, p. 11) also provide the answer to, “What is the curl of our velocity?” A left-invariant field on S^3 is a curl eigenfield with eigenvalue -2

(a right-invariant field has eigenvalue +2):

$$\nabla \times \vec{v} = \pm 2\vec{v}. \quad (\text{F.7})$$

This is true for a unit 3-sphere, but a 3-sphere of radius r_0 gives an eigenvalue: $\pm 2/r_0$. This makes the Hopf velocity a Beltrami field, one where its curl is tangent to itself. Alas, the Hopf velocity is not irrotational. Unless there is another field that satisfies this criterion in addition to the first three, we should only use the normal fluid velocity as our driving velocity.

It turns out that there is no other field on S^3 that meets all the previous criteria, but is also curl-free. This comes from a corollary of de Rham's theorem ([Frankel, 1997](#), p. 357). For a compact manifold, the p^{th} Betti number is the maximal number of closed p -forms which are not exact. A closed p -form is one which satisfies $d\omega^p = 0$, where d is the exterior derivative (see Section [F.2](#)), while an exact p -form satisfies $\omega^p = d\alpha^{p-1}$. Since $d^2\omega$ for any p -form, all exact p -forms are closed, but not all closed p -forms are exact. We are interested in 1-forms, the covariant version of a contravariant vector field. In three dimensions at least, being closed equates with being curl-free. Since the 1^{st} Betti number is zero for S^3 , there are no curl-free vector fields on S^3 . Actually, this tells us no *non-exact*, closed, covariant vector fields exist on S^3 . However, [Adams \(1962\)](#) showed that there are only three smooth

linearly-independent vector fields on S^3 , with curl or not. The Hopf vector fields,

$$\vec{v}_1 = (-y, x, -w, z),$$

$$\vec{v}_2 = (z, -w, -x, y),$$

$$\vec{v}_3 = (-w, -z, y, x),$$

are exactly those vector fields. So, the Hopf velocity field we use as our driving velocity is the best we can do.

There is one more relevant property of the Hopf vector field: for any divergence-free field on S^3 , the Biot-Savart law is the inverse of the curl ([DeTurck and Gluck, 2004](#)). Again, for a unit 3-sphere:

$$BS(\vec{v}) = \pm \frac{1}{2} \vec{v}, \quad (\text{F.8})$$

where the \pm is the same as for the curl, depending on whether the field is right-invariant (like ours) or left-invariant. I explore the implications of this in the discussion of Chapter [5.2](#).

F.2 Divergence and Curl of Hopf Velocity

Here, I wish to compute both the divergence and curl of the Hopf velocity on S^3 . This section depends heavily on the tools and notation of differential geometry. But an introduction to it all is well beyond the scope of this work, but could be found in [Frankel \(1997\)](#).

I will start by getting the requisite definitions out of the way. For vector field $v = v^\mu \partial_\mu$, in a three-dimensional Riemannian manifold:

$$\text{div}(v) = \star d \star v^\flat, \quad (\text{F.9})$$

$$\text{curl}(v) = [\star(dv^\flat)]^\sharp, \quad (\text{F.10})$$

with d the exterior derivative, \star the hodge dual, and \flat, \sharp lowering and raising operators (musical isomorphisms). Note that there are other ways to identify these vector operations in the language of differential geometry. However, I do show the use of these in Euclidean space. This discussion uses Einstein summation notation, where we sum over the components for repeated upper and lower indices.

If ω is a p -form, written as:

$$\omega = f_I dx^I = f_{i_1 i_2 \dots i_p} dx^{i_1} \wedge dx^{i_2} \wedge \dots \wedge dx^{i_p}, \quad (\text{F.11})$$

the exterior derivative takes this p -form to a $(p+1)$ -form in the following manner:

$$d\omega = \frac{\partial f_I}{\partial x^j} dx^j \wedge dx^I. \quad (\text{F.12})$$

Here, \wedge is the wedge product defined by:

$$dx^1 \wedge dx^2 = dx^1 \otimes dx^2 - dx^2 \otimes dx^1. \quad (\text{F.13})$$

The hodge dual turns a p -form in n -dimensional space into an pseudo $(n-p)$ -form

with components:

$$(\star\alpha)_{j_1 j_2 \dots j_{n-p}} = \frac{\sqrt{|\det(g)|}}{p!} \alpha^{k_1 \dots k_p} \epsilon_{k_1 \dots k_p j_1 \dots j_{n-p}}$$

$$\alpha^{k_1 \dots k_p} = g^{k_1 s_1} \dots g^{k_p s_p} \alpha_{s_1 \dots s_p}. \quad (\text{F.14})$$

Here, $g^{\mu\nu}$ is the metric, and ϵ is the Levi-Civita symbol. Finally, our last definitions are the lowering and raising operators (respectively):

$$v^\flat = g_{ij} v^i dx^j, \quad (\text{F.15})$$

$$\omega^\sharp = g^{ij} \omega_i \partial_j, \quad (\text{F.16})$$

The notation stands for $\partial_j = \partial/\partial x^j$. These are the tools we will need to compute the divergence and the curl of our vector field. We shall start with the divergence.

F.2.1 Divergence of Hopf Velocity

First, let us check that this equation gives us the correct result for a simple vector field in \mathbb{R}^3 : (x, y, z) . The metric would be given by: $ds^2 = dx^2 + dy^2 + dz^2$. So, $g_{\mu\nu} = \delta_{\mu\nu}$, the Kronecker delta.

Working through Equation F.9, from the inside, out:

$$v^\flat = v_\mu dx^\mu = x dx + y dy + z dz.$$

This is a 1-form in 3-dimensional space, so the hodge dual would result in a pseudo

2-form.

$$\begin{aligned}
(\star v^\flat)_{\mu\nu} &= \frac{\sqrt{|det(g)|}}{1!} (v^\flat)^\sigma \epsilon_{\sigma\mu\nu} \\
(\star v^\flat)_{xy} &= -(\star v^\flat)_{yx} = v^\sigma \epsilon_{\sigma xy} = z \epsilon_{zxy} = z \\
(\star v^\flat)_{xz} &= -(\star v^\flat)_{zx} = y \epsilon_{yxz} = -y \\
(\star v^\flat)_{yz} &= -(\star v^\flat)_{zy} = x \epsilon_{xyz} = x
\end{aligned}$$

And all other components would be zero. So:

$$\star v^\flat = z dx \wedge dy - y dx \wedge dz + x dy \wedge dz.$$

Now, continuing on, Equation F.12 tells us:

$$\begin{aligned}
d(\star v^\flat) &= \frac{\partial z}{\partial z} dz \wedge dx \wedge dy - \frac{\partial y}{\partial y} dy \wedge dx \wedge dz + \frac{\partial x}{\partial x} dx \wedge dy \wedge dz \\
&= 3 dx \wedge dy \wedge dz.
\end{aligned}$$

Lastly, the final hodge dual takes our 3-form in \mathbb{R}^3 to a 0-form:

$$div(v) = \star d \star v^\flat = \frac{\sqrt{|det(g)|}}{3!} (d \star v^\flat)^{\sigma\mu\nu} \epsilon_{\sigma\mu\nu} = 3.$$

The six permutations of $(d \star v^\flat)^{\sigma\mu\nu}$ along with the permutations of the Levi-Civita symbol add to cancel out the $3!$ in the denominator. It works.

To calculate the divergence of the Hopf vector field, we first need to pick a coordinate system. The divergence is a property of the vector field, not the coordinates.

So the natural choice, which simplifies the math significantly, is the Hopf coordinate system, (η, ζ_1, ζ_2) , where $(0 \leq \eta \leq \pi/2)$, and $(0 \leq \zeta_1, \zeta_2 < 2\pi)$:

$$ds^2 = r_0^2(d\eta^2 + \sin^2 \eta d\zeta_1^2 + \cos^2 \eta d\zeta_2^2)$$

$$x = r_0 \cos \zeta_1 \sin \eta, \quad y = r_0 \sin \zeta_1 \sin \eta$$

$$z = r_0 \cos \zeta_2 \cos \eta, \quad w = r_0 \sin \zeta_2 \cos \eta$$

Finally, we need the inverse relations to convert v into Hopf coordinates. This particular form needs to give the full range for the Hopf coordinates.

$$\begin{aligned}\eta &= \operatorname{arccot} \left(\sqrt{\frac{z^2 + w^2}{x^2 + y^2}} \right) \\ \zeta_1 &= 2\operatorname{arccot} \left(\frac{\sqrt{x^2 + y^2} + x}{y} \right) \\ \zeta_2 &= 2\operatorname{arccot} \left(\frac{\sqrt{z^2 + w^2} + z}{w} \right)\end{aligned}$$

To transform the Hopf velocity, we need the following relation:

$$v^{\mu'} = \frac{\partial x^{\mu'}}{\partial x^\mu} v^\mu \tag{F.17}$$

Using $d[\operatorname{arccot}(u(x))] / dx = (-du/dx)/(1 + u^2)$ and the following values, we can

transform coordinate systems:

$$\begin{aligned}\frac{\partial \eta}{\partial x} &= \frac{x}{r_0^2} \sqrt{\frac{z^2 + w^2}{x^2 + y^2}}, \quad \frac{\partial \eta}{\partial y} = \frac{y}{r_0^2} \sqrt{\frac{z^2 + w^2}{x^2 + y^2}}, \quad \frac{\partial \eta}{\partial z} = \frac{-z}{r_0^2} \sqrt{\frac{x^2 + y^2}{z^2 + w^2}}, \quad \frac{\partial \eta}{\partial w} = \frac{-w}{r_0^2} \sqrt{\frac{x^2 + y^2}{z^2 + w^2}} \\ \frac{\partial \zeta_1}{\partial x} &= \frac{-y}{x^2 + y^2}, \quad \frac{\partial \zeta_1}{\partial y} = \frac{x}{x^2 + y^2}, \quad \frac{\partial \zeta_1}{\partial z} = \frac{\partial \zeta_1}{\partial w} = 0 \\ \frac{\partial \zeta_2}{\partial x} &= \frac{\partial \zeta_2}{\partial y} = 0, \quad \frac{\partial \zeta_2}{\partial z} = \frac{-w}{z^2 + w^2}, \quad \frac{\partial \zeta_2}{\partial w} = \frac{z}{z^2 + w^2}\end{aligned}$$

So the Hopf velocity $(-y, x, -w, z)$ in Hopf coordinates becomes, very simply:

$$v = \partial_{\zeta_1} + \partial_{\zeta_2} = (0, 1, 1). \quad (\text{F.18})$$

Noting that: $g_{\eta\eta} = r_0^2$, $g_{\zeta_1\zeta_1} = r_0^2 \sin^2 \eta$, and $g_{\zeta_2\zeta_2} = r_0^2 \cos^2 \eta$, where all others are zero. Again, working our way through Equation F.9 from inside, out:

$$\begin{aligned}v^\flat &= r_0^2(\sin^2 \eta d\zeta_1 + \cos^2 \eta d\zeta_2) \\ \star v^\flat &= r_0^3 \sin \eta \cos \eta (d\eta \wedge d\zeta_1 - d\eta \wedge d\zeta_2)\end{aligned} \quad (\text{F.19})$$

Since the coefficient of $\star v^\flat$ is only a function η , only this derivative will survive taking the exterior derivative. We are left with:

$$d \star v^\flat = \frac{\partial}{\partial \eta} [r_0^3 \sin \eta \cos \eta] d\eta \wedge (d\eta \wedge d\zeta_1 - d\eta \wedge d\zeta_2).$$

But $dx^j \wedge dx^j = 0$ from Equation F.13. So we have our result, the Hopf velocity is divergence-free:

$$\operatorname{div}(v) = \star d \star v^\flat = 0. \quad (\text{F.20})$$

F.2.2 Curl of Hopf Velocity

Before pressing on with Equation F.10, let us show that this form of the curl reproduces the results we want for a simple vector field in \mathbb{R}^3 : $ds^2 = dx^2 + dy^2 + dz^2$. The vector field we will look at is: $v = (-y, x, 0)$.

Briefly: $v^\flat = -ydx + xdy$, $dv^\flat = -dy \wedge dx + dx \wedge dy = 2dx \wedge dy$.

$$(\star dv^\flat)_\mu = \frac{1}{2} (2\epsilon_{xy\mu} - 2\epsilon_{yx\mu})$$

$$\text{curl}(u) = [\star(dv^\flat)]^\sharp = 2\partial_z = (0, 0, 2)$$

Which is correct.

Now we shall compute the curl of $v = (-y, x, -w, z)$, in Hopf coordinates: $(0, 1, 1)$. We have already computed v^\flat , Equation F.19. So moving on:

$$dv^\flat = r_0^2 \sin \eta \cos \eta (d\eta \wedge d\zeta_1 - d\eta \wedge d\zeta_2)$$

The hodge dual takes the form:

$$(\star dv^\flat)_\mu = \frac{\sqrt{|\det(g)|}}{2} (dv^\flat)^{\nu\sigma} \epsilon_{\nu\sigma\mu}$$

And its various terms are given by:

$$\begin{aligned}
\sqrt{|det(g)|} &= r_0^3 \sin \eta \cos \eta \\
(dv^\flat)^{\eta\zeta_1} &= -(dv^\flat)^{\zeta_1\eta} = 2 \cot \eta / r_0^2 \\
(dv^\flat)^{\eta\zeta_2} &= -(dv^\flat)^{\zeta_2\eta} = -2 \tan \eta / r_0^2 \\
(\star dv^\flat)_\eta &= 0 \\
(\star dv^\flat)_{\zeta_1} &= \frac{r_0^3 \sin \eta \cos \eta}{2} \left[\frac{-2 \tan \eta}{r_0^2} \epsilon_{\eta\zeta_2\zeta_1} + \frac{2 \tan \eta}{r_0^2} \epsilon_{\zeta_2\eta\zeta_1} \right] \\
&= 2r_0 \sin^2 \eta \\
(\star dv^\flat)_{\zeta_2} &= \frac{r_0^3 \sin \eta \cos \eta}{2} \left[\frac{2 \cot \eta}{r_0^2} \epsilon_{\eta\zeta_1\zeta_2} - \frac{2 \cot \eta}{r_0^2} \epsilon_{\zeta_1\eta\zeta_2} \right] \\
&= 2r_0 \cos^2 \eta
\end{aligned}$$

This gives us:

$$\star dv^\flat = 2r_0 (\sin^2 \eta d\zeta_1 + \cos^2 \eta d\zeta_2).$$

Finally to apply the raising operator, note: $g^m = 1/r_0^2$, $g^{\zeta_1\zeta_1} = 1/(r_0^2 \sin^2 \eta)$, and $g^{\zeta_2\zeta_2} = 1/(r_0^2 \cos^2 \eta)$:

$$\begin{aligned}
curl(v) &= [\star dv^\flat]^\sharp = \frac{2}{r_0} (\partial_{\zeta_1} + \partial_{\zeta_2}) \\
curl(v) &= \frac{2}{r_0} v.
\end{aligned} \tag{F.21}$$

We have confirmed what [DeTurck and Gluck \(2004\)](#) informed us: the Hopf vector field is an eigenfield of the curl operator, with eigenvalue $2/r_0$.

Appendix G

Appendix References

G.1 References

- Adams, J. F. *Annals of Mathematics*, **75**, 603 (1962).
- DeTurck, D. and Gluck, H. *arXiv:math/0406276* (2004).
- Frankel, T. *The Geometry of Physics: An Introduction*. Cambridge University Press, 2nd edition (1997).
- Gluck, H. and Warner, F. W. *Duke Mathematical Journal*, **50**, 107 (1983).
- Guyon, E., Hulin, J.-P., Petit, L., and Mitescu, C. D. *Physical Hydrodynamics*. Oxford University Press (1991).
- Lyons, D. W. *Mathematics Magazine*, **76**, 87 (2003).
- Schwarz, K. W. *Physical Review Letters*, **49**, 283 (1982).
- Schwarz, K. W. *Physical Review B*, **38**, 2398 (1988).

Stewart, J. *Calculus: Concepts and Contexts*. Brooks/Cole, second edition (2001).

Swanson, C. E. and Donnelly, R. J. *Journal of Low Temperature Physics*, **61**, 363 (1985).